Classical and Quantum Nonlinear Optical Information Processing

Thesis by

Mankei Tsang

In Partial Fulfillment of the Requirements

for the Degree of

Doctor of Philosophy

California Institute of Technology

Pasadena, California

2006

(Defended May 2, 2006)

Acknowledgements

First and foremost I would like to thank my mentor, Professor Demetri Psaltis, for giving me the opportunity to come to Caltech and for his insightful advice about optics, research, and all aspects of life in academia. It has truly been a pleasure working with him in my four years at Caltech.

I would also like to acknowledge my past and present group mates, who are all intelligent and capable, and from whom I have learned a great deal. I am especially grateful to Dr. Ye Pu and Dr. Martin Centurion, for their guidance when I worked briefly in the lab and for sharing with me their exciting experiment results; Jim Adleman and Dr. David Erickson, for all the driving in a long but enjoyable road trip to the DARPA workship in Sonoma; Lucinda Acosta, for her help in administrative tasks; and Yayun Liu, for her words of encouragement when I first started at Caltech. Furthermore, I would like to acknowledge Dr. Zhiwen Liu, Dr. Hung-Te Hsieh, Zhenyu Li, Hua Long, Troy Rockwood, Eric Ostby, Xin Heng, Baiyang Li, Dr. Allen Pu, Jae-Woo Choi, and Ted Dikaliotis, with whom I have enjoyed countless inspiring discussions.

I am indebted to Dr. Fiorenzo Omenetto, who provided his experimental results for my first paper, and generously lent us his experimental equipment several times; Professor Michael Cross, for his advice on the metaphoric optical computing project; and my candidacy and thesis examining committee members, including Professor Amnon Yariv, Professor Changhuei Yang, Professor Oskar Painter, Professor Kerry Vahala, and Dr. John Hong, for their valuable time, as well as their insightful feedback on my research.

I will forever be indebted to my mother, whose love, care, and support make me the person I am now, despite all the adversities she has had to face. I am also grateful to my elder sister, and all my relatives and friends in Hong Kong and the United States, who are extremely supportive of my family and myself.

Last but not the least, I thank my girlfriend, Helen. Without her I would not have survived a single day at Caltech.

List of Publications

[1] M. Tsang and D. Psaltis, "Dispersion and nonlinearity compensation by spectral phase conjugation," Opt. Lett. **28**, 1558 (2003).

[2] M. Tsang, D. Psaltis, and F. G. Omenetto, "Reverse propagation of femtosecond pulses in optical fibers," Opt. Lett. **28**, 1873 (2003).

[3] M. Tsang and D. Psaltis, "Spectral phase conjugation with cross-phase modulation compensation," Opt. Express **12**, 2207 (2004).

[4] M. Tsang and D. Psaltis, "Spectral phase conjugation by quasi-phase-matched three-wave mixing," Opt. Commun. **242**, 659 (2004).

[5] M. Tsang and D. Psaltis, "Spontaneous spectral phase conjugation for coincident frequency entanglement," Phys. Rev. A **71**, 043806 (2005).

[6] M. Centurion, Y. Pu, M. Tsang, and D. Psaltis, "Dynamics of filament formation in a Kerr medium," Phys. Rev. A **71**, 063811 (2005).

[7] M. Tsang, "Spectral phase conjugation via extended phase matching," J. Opt. Soc. Am. B **23**, 861 (2006).

[8] M. Tsang and D. Psaltis, "Propagation of temporal entanglement," Phys. Rev. A **73**, 013822 (2006).

[9] M. Tsang, "Quantum temporal correlations and entanglement via adiabatic control of vector solitons," e-print quant-ph/0603088 [submitted to Phys. Rev. Lett.].

[10] M. Tsang and D. Psaltis, "Reflectionless evanescent wave amplification via two dielectric planar waveguides," e-print physics/0603079 [submitted to Opt. Lett.].

[11] M. Tsang, "Beating the spatial standard quantum limits via adiabatic soliton expansion and negative refraction," under preparation.

[12] M. Tsang and D. Psaltis, "Metaphoric optical computing of fluid dynamics," under preparation.

Abstract

This thesis is a theoretical investigation of the classical and quantum information processing enabled by the advent of modern ultrafast nonlinear optics.

Chapter 2 and 3 study the propagation of ultrashort optical pulses in optical fibers, and propose two methods of compensating the linear and nonlinear distortions experienced by the pulses, namely, reverse propagation and spectral phase conjugation. Chapter 4 and 5 suggest different schemes that implement spectral phase conjugation.

Chapter 6 and 7 establish the connection between classical spectral phase conjugation and quantum coincident frequency entanglement. Chapter 6 shows how a spectral phase conjugator can create coincident frequency entangled photon pairs, and Chapter 7 in turn demonstrates how a coincident frequency entanglement generator can perform spectral phase conjugation.

The next three chapters, 8, 9, and 10, focus on quantum spatiotemporal information processing. Chapter 8 studies the temporal properties of entangled photon pair propagation and proposes the concept of quantum temporal imaging. Chapter 9 investigates how optical solitons can be used to perform quantum timing jitter reduction and temporal entanglement, while Chapter 10 applies the same idea to the spatial domain for quantum spatial information processing tasks, such as spatial beam displacement uncertainty reduction and quantum lithography.

The final two chapters return to a couple of miscellaneous problems in classical optics. Chapter 11 shows how a pair of dielectric slabs can amplify the near field of an optical image. Chapter 12 explores the similarities between nonlinear optics and fluid dynamics, and speculates on the possibility of using nonlinear optics experiments to simulate fluid dynamics problems.

Contents

List of Figures

List of Tables

Chapter 1

Summary

This thesis investigates various classical and quantum optics techniques for applications in optical communications, quantum information processing, imaging, and computing.

Chapter 2 presents a numerical technique for reversing femtosecond pulse propagation in an optical fiber, such that given any output pulse it is possible to obtain the input pulse shape by numerically undoing all dispersion and nonlinear effects. The technique is tested against experimental results, and it is shown that it can be used for fiber output pulse optimization in both the anomalous and normal dispersion regimes [1].

Chapter 3 proposes the use of spectral phase conjugation to compensate for dispersion of all orders, self-phase modulation, and self-steepening of an optical pulse in a fiber. Although this method cannot compensate for loss and intrapulse Raman scattering, it is superior to the previously suggested midway temporal phase conjugation method if high-order dispersion is a main source of distortion. The reshaping performance of our proposed scheme and a combined temporal and spectral phase conjugation scheme in the presence of uncompensated effects is studied numerically [2].

Chapter 4 analyzes spectral phase conjugation with short pump pulses in a third-order nonlinear material in depth. It is shown that if signal amplification is considered, the conversion efficiency can be significantly higher than previously considered, while the spectral phase conjugation operation remains accurate. A novel method of compensating for cross-phase modulation, the main parasitic effect, is also proposed. The validity of our theory and the performance of the spectral phase conjugation scheme are studied numerically [3].

Chapter 5 proposes a novel spectral phase conjugation scheme by three-wave mixing. It is shown that a phase-conjugated and time-reversed replica of the incoming signal can be generated, if appropriate quasi-phase matching is achieved and the three-wave mixing process is transversely pumped by a short second-harmonic pulse [4].

Chapter 6 studies spontaneous parametric processes pumped transversely with short pulses under a unified framework, which proves that such processes can efficiently generate entangled photon pairs with time anticorrelation and frequency correlation. Improvements upon previously proposed schemes can be made by the use of quasi-phase matching, four-wave mixing, and cross-phase modulation compensation. The use of frequency-correlated photons in the Hung-Ou-Mandel interferometer is also studied [5].

Chapter 7 demonstrates that the copropagating three-wave-mixing parametric process, with appropriate type-II extended phase matching and pumped with a short second-harmonic pulse, can perform spectral phase conjugation and parametric amplification, which shows a threshold behavior analogous to backward wave oscillation. The process is also analyzed in the Heisenberg picture, which predicts a spontaneous parametric down conversion rate in agreement with experimental results reported elsewhere [6].

Chapter 8 derives the equations that govern the temporal evolution of two photons in the Schrödinger picture, taking into account the effects of loss, group-velocity dispersion, temporal phase modulation, linear coupling among different optical modes, and four-wave mixing. Inspired by the formalism, the concept of quantum temporal imaging is proposed, which uses dispersive elements and temporal phase modulators to manipulate the temporal correlation of two entangled photons. The exact solution of a two-photon vector soliton is also presented, in order to demonstrate the ease of use and intuitiveness of the proposed formulation [7].

Chapter 9 shows that optical pulses with a mean position accuracy beyond the standard quantum limit can be produced by adiabatically expanding an optical vector soliton followed by classical dispersion management. The proposed scheme is also capable of entangling positions of optical pulses and can potentially be used for general continuous-variable quantum information processing [8].

Chapter 10 studies spatial quantum enhancement effects under a unified framework. An approach of generating arbitrary quantum lithographic patterns by the use of multiphoton coincident momentum states is proposed. It is shown that the multiphoton absorption rate of photons with a quantum-enhanced lithographic resolution is reduced, not enhanced, contrary to popular belief. Finally, the use of adiabatic soliton expansion followed by negative refraction is proposed to beat both the standard quantum limit on the optical beam displacement accuracy, as well as that on the minimum spot size of quantum lithography [9].

In Chapter 11, utilizing the underlying physics of evanescent wave amplification by a negative-refractive-index slab, it is shown that evanescent waves with specific spatial frequencies can also be amplified without any reflection simply by two dielectric planar waveguides. The simple configuration allows one to take advantage of the high resolution limit of a high-refractive-index material without contact with the object [10].

Chapter 12 presents theoretical and numerical evidence to show that self-defocusing nonlinear optical propagation can be used to compute Euler fluid dynamics and possibly Navier-Stokes fluid dynamics. In particular, the formation of twin vortices and the Kármán vortex street behind an obstacle, two well-known viscous fluid phenomena, is numerically demonstrated using the nonlinear Schrödinger equation [11].

Bibliography

[1] M. Tsang, D. Psaltis, and F. G. Omenetto, Opt. Lett. **28**, 1873 (2003).

[2] M. Tsang and D. Psaltis, Opt. Lett. **28**, 1558 (2003).

[3] M. Tsang and D. Psaltis, Opt. Express **12**, 2207 (2004).

[4] M. Tsang and D. Psaltis, Opt. Commun. **242**, 659 (2004).

[5] M. Tsang and D. Psaltis, Phys. Rev. A **71**, 043806 (2005).

[6] M. Tsang, J. Opt. Soc. Am. B **23**, 861 (2006).

[7] M. Tsang and D. Psaltis, Phys. Rev. A **73**, 013822 (2006).

[8] M. Tsang, e-print quant-ph/0603088 [submitted to Phys. Rev. Lett.].

[9] M. Tsang, under preparation.

[10] M. Tsang and D. Psaltis, e-print physics/0603079 [submitted to Opt. Lett.].

[11] M. Tsang and D. Psaltis, under preparation.

Chapter 2

Reverse propagation of femtosecond pulses in optical fibers

2.1 Introduction

Dispersion and nonlinear effects have been the bottleneck of ultrafast pulse propagation in an optical fiber. Various schemes, for example, optical solitons [1] and optical phase conjugation (OPC) [2, 3] have been proposed to compensate for these effects, yet the high-order distortions including third-order dispersion (TOD), self-steepening, and Raman scattering remain undefeated. Femtosecond power delivery in a normally dispersive fiber, which is useful for biomedical applications, is especially difficult to achieve because normal dispersion and nonlinear effects always tend to broaden and distort a pulse. Another scheme is to embrace all the effects and adopt an adaptive optimization method, typically in the form of genetic algorithm, hoping that modulating the input pulse shape can produce an output with desirable properties [4, 5, 6]. Although an adaptive method can compensate for pulse propagation distortions and unknown experimental variables, it does not make full use of our theoretical knowledge of optical fiber ultrafast pulse propagation and may therefore be time consuming and suboptimal.

In this chapter we show that by reversing the nonlinear pulse propagation equation it is possible to theoretically predict the exact input pulse shape that gives a desired output of a fiber. All dispersion and nonlinear effects can be incorporated into the simulation, and hence one can produce any kind of pulse shape at the output end by shaping the input pulse appropriately according to the calculated result. In conjunction with currently available femtosecond pulse-shaping techniques such as $4f$ pulse shaping [7] this approach is especially suited to provide custom-shaped high-power ultrafast pulse delivery both in normally and anomalously dispersive fibers.

2.2 Theory

The nonlinear pulse propagation equation in a fiber is given by the general form [1]

$$\frac{\partial A(z,T)}{\partial z} = \{\hat{D} + \hat{N}[A(z,T)]\}A(z,T), \tag{2.1}$$

where $A(z,T)$ is the pulse envelope, $\hat{D}$ is the linear operator that includes absorption and all dispersion effects, and $\hat{N}$ is the nonlinear operator that includes all nonlinear effects and is a function of $A(z,T)$. Mathematically, the output is obtained by application of the propagation operator to the input:

$$A(L,T) = \exp\left\{L\hat{D} + \int_0^L \hat{N}[A(z,T)]dz\right\}A(0,T), \tag{2.2}$$

where L is the length of the fiber. The input can also be expressed in terms of the output by application of the reverse propagation operator:

$$A(0,T) = \exp\left\{-L\hat{D} - \int_0^L \hat{N}[A(z,T)]dz\right\}A(L,T). \tag{2.3}$$

To solve this equation and derive the input pulse shape given the output, we use the standard Fourier split-step method:

$$A(z,T) \approx \exp(-h\hat{D})\exp\{-h\hat{N}[A(z+h,T)]\}A(z+h,T), \tag{2.4}$$

in each step of which the linear and nonlinear effects on a pulse shape are evaluated separately for a small propagation distance h.

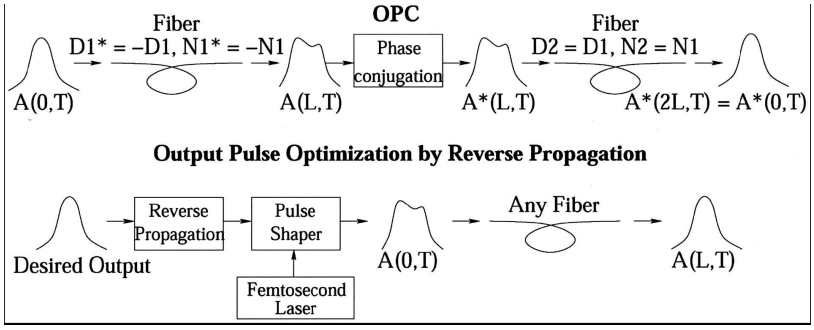

Figure 2.1: Comparison of OPC and reverse propagation.

As a comparison, let us consider the OPC technique in the operator notation. Figure 2.1 depicts schematically the OPC method and the reverse propagation method. By conjugating Eq. (2.2) and comparing the result with Eq. (2.3), one can see that OPC can reconstruct an input pulse if $\hat{D}$ and $\hat{N}$ contain operators with the property $\hat{M} = -\hat{M}^*$. This restriction precludes many important phenomena, such as loss, TOD, and

self-steepening, that may severely hamper the accuracy of pulse reconstruction by OPC, especially in the femtosecond regime. In a numerical simulation of reverse propagation, however, there is no such limitation, and all effects can be included to yield the optimal input pulse shape.

To model femtosecond pulse propagation, we choose the linear operator $\hat{D}$ to be

$$\hat{D} = -\frac{\alpha}{2} - j\frac{\beta_2}{2}\frac{\partial^2}{\partial T^2} + \frac{\beta_3}{6}\frac{\partial^3}{\partial T^3}. \tag{2.5}$$

The first term corresponds to loss, the second term corresponds to group-velocity dispersion (GVD), and the third term corresponds to TOD. The higher-order dispersion terms are neglected because of the relatively short length considered here but can be easily included if the need arises.

The nonlinear operator $\hat{N}$ is

$$\hat{N} = j\gamma\Big[|A|^2 + \frac{j}{\omega_0}\frac{1}{A}\frac{\partial}{\partial T}(|A|^2 A) - T_R\frac{\partial |A|^2}{\partial T}\Big]. \tag{2.6}$$

The first term corresponds to optical Kerr effect, the second term corresponds to self-steepening, and the third term corresponds to intrapulse Raman scattering.

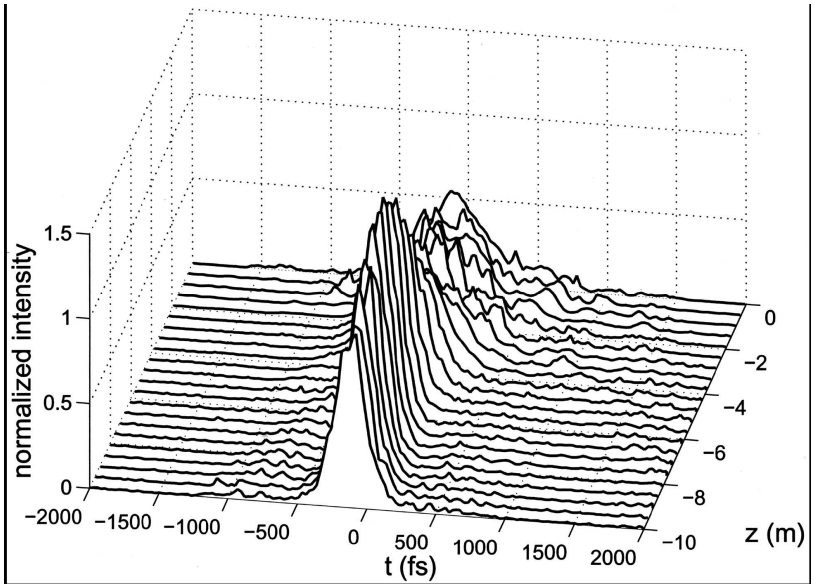

Figure 2.2: Reverse propagation of an experimental output pulse. The experimental output pulse shape is plotted at $z = 0$ m and numerically propagates in reverse from $z = 0$ m to $z = -10$ m.

2.3 Comparison with experiments

To test the validity of reverse propagation, in an experiment we launch a 150 fs positively chirped hyperbolic secant pulse with a peak power of 1 kW in a 10 m long Corning SMF-28 fiber [6]. From frequency-resolved

optical gating measurements we obtain the amplitude and phase of both input and output pulses. The output pulse is then reverse propagated in a computer simulation as in Fig. 2.2. The output pulse shape is plotted at $z = 0$ m at the top of the graph, and propagation effects are reversed numerically as the pulse goes from $z = 0$ m to $z = -10$ m. The simulated input from reverse propagation is compared with the experimental input in Fig. 2.3. Both pulses are remarkably similar, with nearly identical amplitudes and positive chirp, showing that the reverse propagation theory is consistent with experimental results.

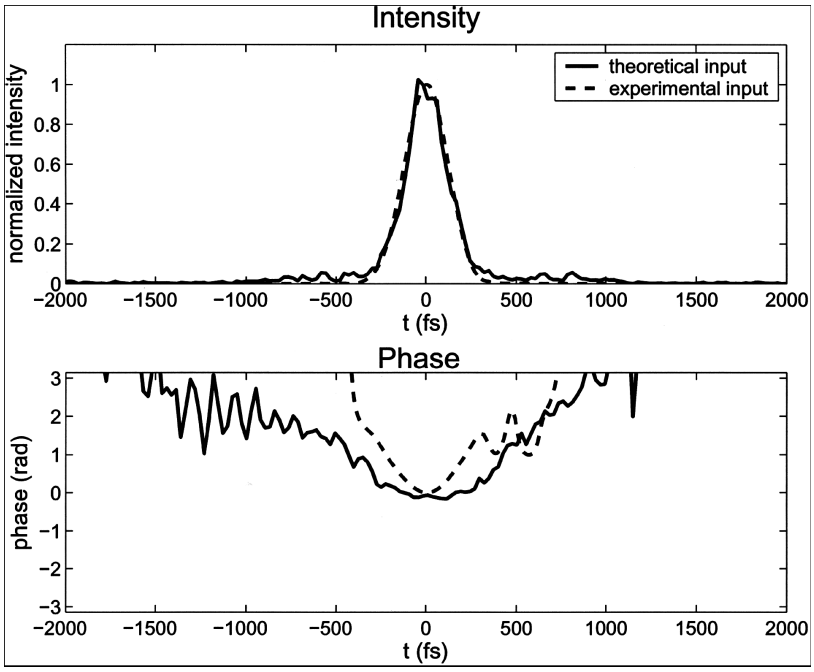

Figure 2.3: Comparison of the input obtained from reverse propagation and the actual experimental input.

2.4 Numerical analysis

Reverse propagation can be used to calculate the proper input pulse shape that provides a narrow pulse at the output. As a numerical example, let us consider a 100-m-long conventional dispersion-shifted fiber with parameters $\beta_2 = -1$ ps^2/km, $\beta_3 = 0.1$ ps^3/km, $\gamma = 1.5$ W^{-1}km^{-1}, and $T_R = 3$ fs at $\lambda_0 = 1550$ nm. A fundamental soliton with a pulse width T_0 of 100 fs can propagate in this fiber with a peak power of 67 W but will experience distortions as a result of TOD, self-steepening, and soliton self-frequency shift. To obtain better output, we reverse the propagation of a desirable pulse shape, say a chirped sech pulse with a pulse profile $A(0,T) = P_0^{1/2}\mathrm{sech}(T/T_0)\exp[-iC(T/T_0)^2/2]$, peak power $P_0 = 67$ W, and chirp $C = 1$. Figure 2.4 shows the reverse propagation of the desired output along the fiber. The peak intensity of the optimized input pulse during propagation is lower than that of a fundamental soliton, thereby avoiding the high-order nonlinear distortions. To obtain an even shorter pulse, we would need to include higher-order linear and nonlinear terms in Eqs. (2.5) and (2.6).

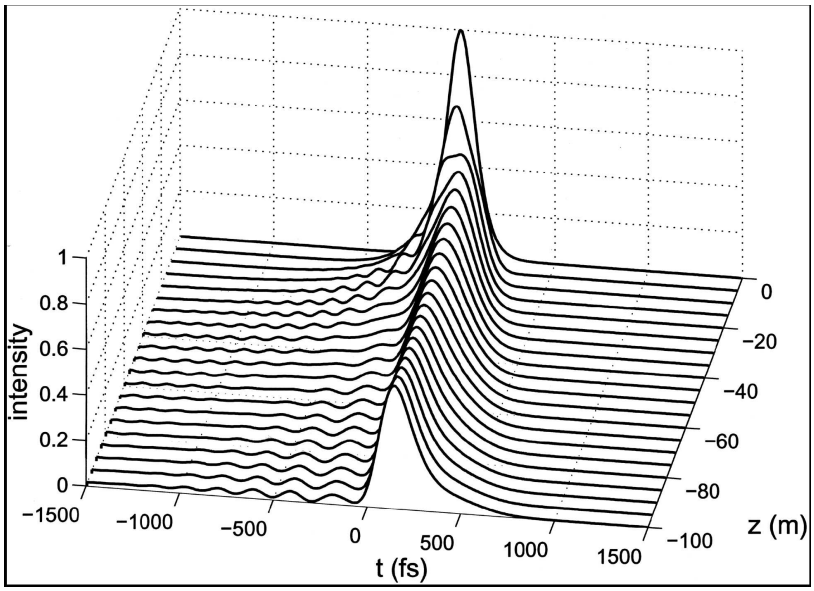

Figure 2.4: Reverse propagation of a chirped sech pulse at $\lambda_0 = 1550$ nm.

It must be stressed that the reverse propagation method is not limited to near-soliton conditions but can be applied to any fiber in both dispersion regimes. For our second numerical example consider a 1-m-long normally dispersive single-mode fiber at $\lambda_0 = 800$ nm, with parameters $\beta_2 = 40$ ps^2/km, $\beta_3 = 0.03$ ps^2/km, and $\gamma = 9$ W^{-1} km^{-1} [8]. A 100-fs unchirped hyperbolic secant pulse, centered at 800 nm, with peak power $P_0 = 20$ kW and total energy $E = 4$ nJ is given as our desired output. Figure 2.5 shows the optimal input pulse amplitude and phase. Qualitatively speaking, the pulse shape is asymmetric to compensate for TOD, self-steepening, and Raman scattering, and the negative chirp ($C = -0.1$ by polynomial fitting) focuses the pulse by GVD. In an experiment the large chirp can be imposed by a grating pair before $4f$ pulse shaping.

We also investigate numerically the OPC technique, as depicted in Fig. (2.1), using the same criteria as those above as a comparison. Figure 2.6 shows the resultant output pulse by OPC compared with the ideal output pulse shape that can be produced by reverse propagation and pulse shaping. The OPC output pulse is distorted by high-order effects, whereas reverse propagation and pulse shaping, taking all the high-order effects into account, produce a better output.

2.5 Conclusion

In conclusion, we have shown in this chapter that reverse propagation is a feasible method of predicting the optimal input pulse shape that will yield any desired output in a well-characterized fiber, defeating all high-order dispersive and nonlinear effects that may be detrimental to other output optimization schemes. The theory is successfully tested against experimental results, and its application to femtosecond pulse delivery through fibers in both dispersion regimes is presented numerically. The interface of reverse propagation

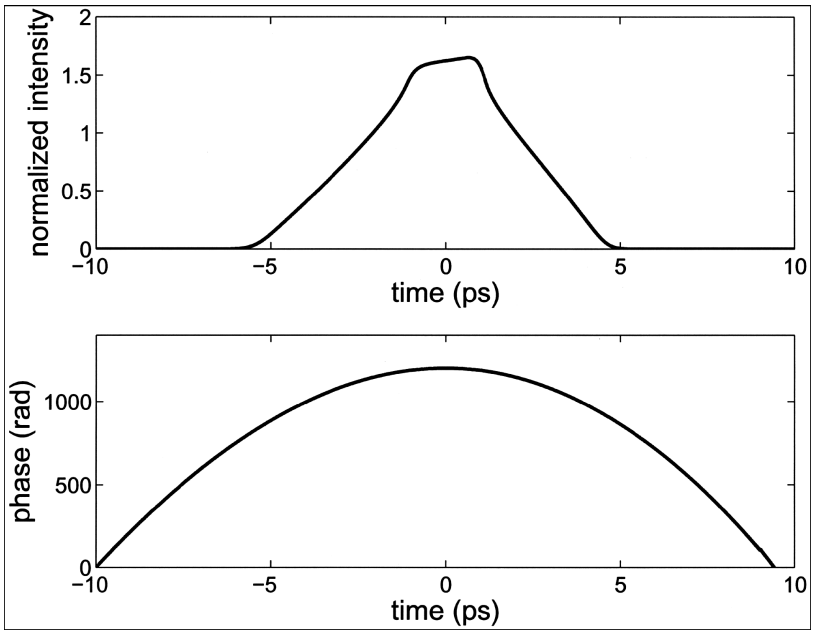

Figure 2.5: Amplitude and phase of the optimal input that produces the desired sech output pulse shape at $\lambda_0 = 800$ nm.

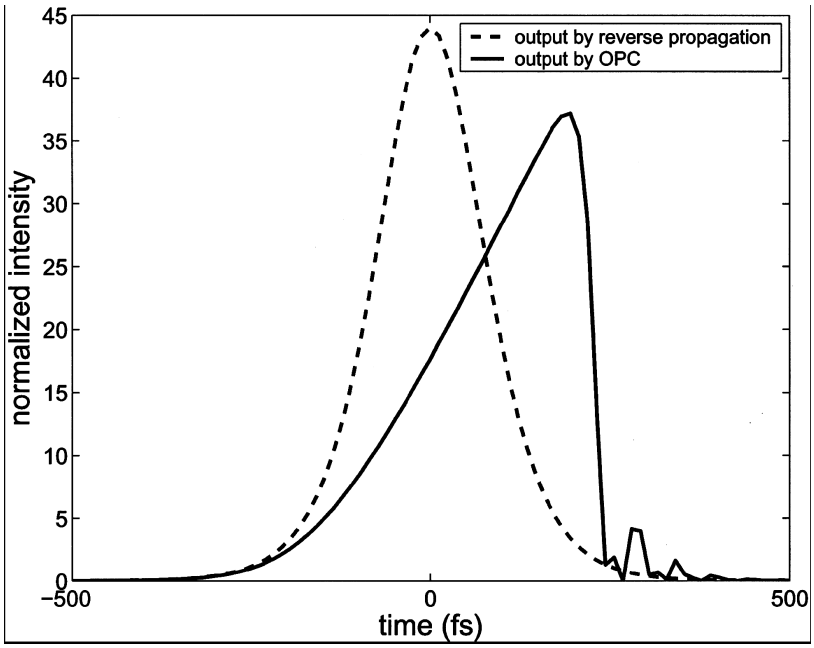

Figure 2.6: Compared with the ideal output pulse shape produced by reverse propagation and pulse shaping, the OPC output is significantly distorted by high-order effects.

code to a pulse shaper can be envisaged for short propagation lengths, so that the proper modulation is applied to the input pulse by the programmable optical modulator of choice. For longer distances, practical realizations become more complex as linear distortions become too large to be overcome by the available modulators alone. In this case linear compensators can be combined with programmable modulators and reverse propagation predictions to compensate for all distortions.

Bibliography

[1] G. P. Agrawal, *Nonlinear Fiber Optics* (Academic, San Diego, Calif., 2001).

[2] A. Yariv, D. Fekete, and D. M. Pepper, Opt. Lett. **4**, 52 (1979).

[3] R. A. Fisher, B. R. Suydam, and D. Yevick, Opt. Lett. **8**, 611 (1983).

[4] R. S. Judson and H. Rabitz, Phys. Rev. Lett. **68**, 1500 (1992).

[5] F. G. Omenetto, B. P. Luce, and A. J. Taylor, J. Opt. Soc. Am. B **16**, 2005 (1999).

[6] F. G. Omenetto, A. J. Taylor, M. D. Moores, and D. H. Reitze, Opt. Lett. **26**, 938 (2001).

[7] A. M. Weiner, J. P. Heritage, and E. M. Kirschner, J. Opt. Soc. Am. B **5**, 1563 (1988).

[8] S. W. Clark, F. O. Ilday, and F. W. Wise, Opt. Lett. **26**, 1320 (2001).

Chapter 3

Dispersion and nonlinearity compensation via spectral phase conjugation

3.1 Introduction

Temporal phase conjugation (TPC) was proposed to compensate for group-velocity dispersion [1], self-phase modulation [2], and intrapulse Raman scattering [3] of an optical pulse in a fiber. However, when the pulse width is sufficiently short or the center wavelength is near the zero-dispersion point, third-order dispersion and self-steepening effects become more prominent and limit the reshaping performance of TPC. To compensate for the high-order effects, alternative methods [4, 5, 6, 7] have been suggested, but many of them are either too complicated or are only able to compensate for a limited number of propagation effects. An interesting scheme, which compensates for all effects by both TPC and a suitably chosen dispersion map, is also proposed by Pina *et al.* [8].

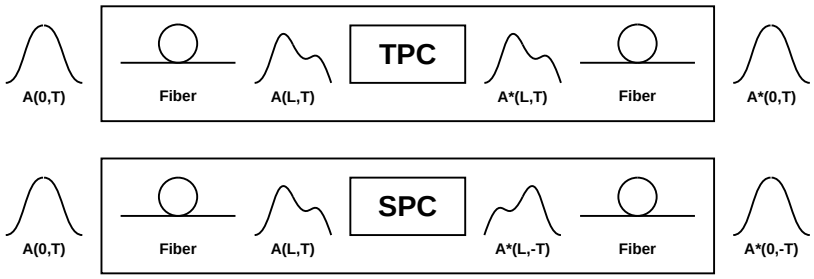

Figure 3.1: Schematics of TPC and SPC.

Instead of just conjugating the time envelope of an optical pulse midway through a fiber as in the TPC scheme, we propose to perform midway phase conjugation as well as time reversal of the pulse envelope (Fig. 3.1). In this way, dispersion of all orders, self-phase modulation, and self-steepening in a fiber are automatically compensated. Conjugation and time reversal of an envelope are equivalent to just conjugation

of the optical pulse in the frequency domain, hence the name spectral phase conjugation (SPC).

3.2 Theory

Consider a pulse $E(t) = A(t)\exp(-j\omega_0 t)$ with envelope $A(t)$ and center frequency ω_0. If we take the conjugate of the Fourier transform of $E(t)$, it becomes

$$\tilde{E}^*(\omega) = \Big[\int_{-\infty}^{\infty} A(t)\exp(-j\omega_0 t)\exp(j\omega t)\mathrm{d}t\Big]^* \tag{3.1}$$

$$= \int_{-\infty}^{\infty} A^*(-t)\exp(-j\omega_0 t)\exp(j\omega t)\mathrm{d}t \tag{3.2}$$

where the substitution $t \rightarrow -t$ is made. Hence, conjugation of individual spectral components of a pulse is equivalent to phase conjugation and time reversal of the temporal envelope. TPC, on the other hand, corresponds to conjugation and inversion in the frequency domain.

Midway SPC is unique in the sense that it can compensate for all dispersion and most nonlinearities simultaneously. Consider the general pulse propagation equation in a fiber,

$$\frac{\partial A(z,T)}{\partial z} = \Big[\hat{D}_T + \hat{N}_T\big(A(z,T)\big)\Big]A(z,T), \tag{3.3}$$

where z is the propagation distance, T is the retarded time with respect to the group velocity $1/\beta_1$ of the pulse ($T = t - \beta_1 z$), and $A(z,T)$ is the pulse envelope. $\hat{D}_T$ is the linear operator,

$$\hat{D}_T = -\frac{\alpha}{2} + \sum_{n=2}^{\infty} j\frac{\beta_n}{n!}(j\frac{\partial}{\partial T})^n, \tag{3.4}$$

where the first term on the right-hand side is the loss term, and the remaining terms are nth-order dispersion terms. $\hat{N}_T$ is the nonlinear operator, which can be expressed as the following for a femtosecond pulse,

$$\hat{N}_T(A) = j\gamma\Big[|A|^2 + \frac{j}{\omega_0}\frac{1}{A}\frac{\partial}{\partial T}(|A|^2 A) - T_R\frac{\partial |A|^2}{\partial T}\Big], \tag{3.5}$$

where the first term on the right-hand side is the self-phase modulation term, the second term is self-steepening, and the third term is intrapulse Raman scattering [9]. The subscript T of $\hat{D}_T$ and $\hat{N}_T$ denotes the derivatives with respect to T in the operators.

We rewrite Eq. (3.3) to express the output pulse in terms of the propagation operator applied to the input pulse [9],

$$A(L,T) = \exp\Big[L\hat{D}_T + \int_0^L \hat{N}_T\big(A(z,T)\big)\mathrm{d}z\Big]A(0,T), \tag{3.6}$$

where L is the fiber length. The input can also be expressed in terms of the output by applying the reverse

propagation operator [7],

$$A(0,T) = \exp\Big[-L\hat{D}_T - \int_0^L \hat{N}_T\big(A(z,T)\big)\mathrm{d}z\Big]A(L,T). \tag{3.7}$$

Now let us take the complex conjugate of Eq. (3.7) and make the substitution $T \to -T$. Eq. (3.7) becomes

$$\begin{aligned} A^*(0,-T) &= \exp\Big[-L\hat{D}^*_{-T} - \int_0^L \hat{N}^*_{-T}\big(A(z,-T)\big)\mathrm{d}z\Big] \\ &\quad A^*(L,-T). \end{aligned} \tag{3.8}$$

The conjugated and time reversed linear operator, ignoring loss, is

$$\hat{D}^*_{-T} = \sum_{n=2}^{\infty} -j\frac{\beta_n}{n!}[(-j)(-\frac{\partial}{\partial T})]^n \tag{3.9}$$

$$= \sum_{n=2}^{\infty} -j\frac{\beta_n}{n!}(j\frac{\partial}{\partial T})^n = -\hat{D}_T. \tag{3.10}$$

Similarly, the nonlinear operator, ignoring intrapulse Raman scattering, is

$$\hat{N}^*_{-T}(A(z,-T)) = -\hat{N}_T(A^*(z,-T)). \tag{3.11}$$

In general, we only keep terms that acquire a minus sign when conjugation and time reversal are both applied. All operator terms, except loss and intrapulse Raman scattering, satisfy our criteria due to their odd combinations of j's and time derivatives. With the substitution $z \to L - z'$, Eq. (3.8) becomes

$$\begin{aligned} A^*(0,-T) &= \exp\Big[L\hat{D}_T + \int_0^L \hat{N}_T\big(A^*(L-z',-T)\big)\mathrm{d}z'\Big] \\ &\quad A^*(L,-T). \end{aligned} \tag{3.12}$$

Eq. (3.12) has the exact same form as Eq. (3.6), but with $A^*(L-z',-T)$ as the solution. In other words, if we launch $A^*(L,-T)$ in another identical fiber, the final output $A^*(0,-T)$ is a conjugated and time reversed version of the first input. This result can only be applied to cases where loss and intrapulse Raman scattering can be neglected. Table 3.1 summarizes the propagation effects that can be compensated by TPC and SPC, respectively.

	loss	EOD	OOD	SPM	SS	IRS
TPC	×	√	×	√	×	√
SPC	×	√	√	√	√	×

Table 3.1: Comparison of TPC and SPC in terms of propagation effects that can be compensated by each scheme. EOD stands for even-order dispersion, OOD stands for odd-order dispersion, SPM stands for self-phase modulation, SS stands for self-steepening, and IRS stands for intrapulse Raman scattering.

To identify important propagation effects for a given optical pulse transmission system, it is useful to define a characteristic length for each propagation effect [9],

$$L_{loss} = \text{loss length} = 1/\alpha, \tag{3.13}$$

$$L_D = \text{dispersion length} = T_0^2/|\beta_2|, \tag{3.14}$$

$$L'_D = \text{third-order dispersion length} = T_0^3/|\beta_3|, \tag{3.15}$$

$$L_{NL} = \text{nonlinear length} = 1/(\gamma P_0), \tag{3.16}$$

$$L_{SS} = \text{self-steepening length} = \omega_0 T_0/(\gamma P_0), \tag{3.17}$$

$$L_R = \text{Raman length} = T_0/(T_R \gamma P_0), \tag{3.18}$$

where T_0 is the pulse width. The significance of a propagation effect can be roughly estimated by the ratio of the total propagation distance L_{total} to the characteristic length. Hence a phase conjugation system should be designed such that the characteristic lengths of uncompensated propagation effects are much longer than L_{total}. This is demonstrated next in the numerical simulations.

3.3 Numerical analysis

As a numerical example, consider $\lambda_0 = 1550$ nm, two dispersion-shifted fibers, each with length $L_{total}/2 = 1$ km, parameters $\beta_2 = -1$ ps^2/km, $\beta_3 = 0.1$ ps^3/km, $\gamma = 1.5$ W^{-1}km^{-1}, $\alpha = 0.2$ dB/km, $T_R = 3$ fs, a temporal or spectral phase conjugator in the middle, an amplifier at each fiber end to compensate for loss, and a super-Gaussian input pulse,

$$A(t) = \sqrt{P_0}\exp[-\frac{1}{2}(\frac{T}{T_0})^6], \tag{3.19}$$

with $T_0 = 200$ fs, and peak power $P_0 = 1.7$ W. The peak power is chosen to be one-tenth of that of a fundamental soliton, such that L_{loss} = 2 km, $L_D = 0.04$ km, $L'_D = 0.08$ km, and $L_{NL} = 0.4$ km. Other characteristic lengths are too long to be significant. Since L_{NL} is comparable to L_{total} while much longer than the dispersion lengths, we expect nonlinear effects to be observable but less significant than dispersion effects. The output pulses with and without compensation schemes are plotted in Fig. 3.2. SPC reconstructs the input pulse at the output almost perfectly, while the TPC output pulse is significantly distorted by third-order dispersion. At this power level, SPC has the advantage over TPC for the former's ability to compensate for all important linear and nonlinear effects together with an amplifier.

In practice, SPC can be performed by spectral holography [4], short-pump four-wave mixing [10] or spectral four-wave mixing [11]. If SPC is to be used in a communication system, one must perform time reversal only on each time slot or a group of slots, within the time window of the SPC device. A synchronous clock, in the form of pump pulses, will therefore be required, unfortunately. The pulses also need to be periodically conjugated before they breach adjacent time windows. In this case solitons are preferred because their broad-

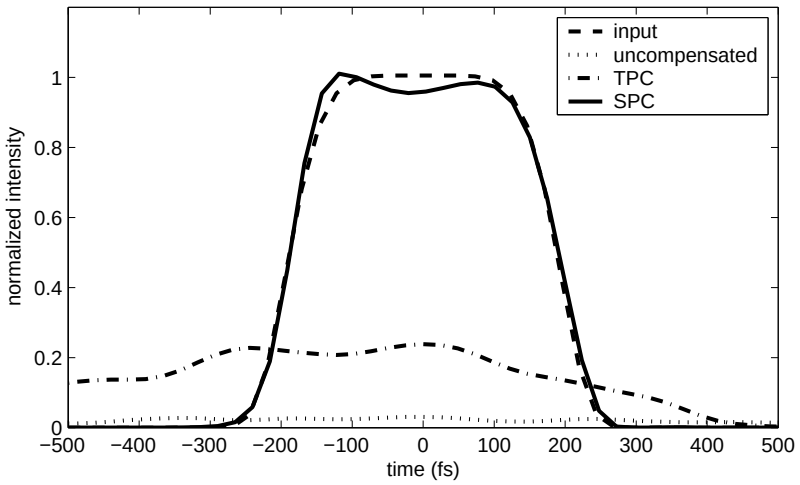

Figure 3.2: Input and output pulses with and without compensation schemes, when a 1.7 W 200 fs super-Gaussian pulse propagates for a total distance of 2 km.

ening is much slower than conventional pulses and the frequency of conjugation can be minimized. We note that periodic conjugation is also required in other schemes for different reasons, such as that suggested by Pina *et. al.*, to satisfy the path-averaging assumption.

Since SPC can compensate for distortions not compensated by TPC, and vice versa, we propose that a hybrid scheme combining SPC and TPC can offer superior performance. An example would be to sandwich a temporal phase conjugator with two midway SPC systems, such that the Raman effect uncompensated in a SPC system can be compensated by the TPC system, at least to first order. More rigorous analysis is required to fully estimate the performance of a hybrid scheme.

Our second numerical example tests the compensation capabilities of SPC and the hybrid scheme for multiple solitons. It has been suggested that TPC can compensate for soliton interactions [12]. Fig. 3.3 plots the output pulses obtained from various compensation schemes for the same parameters as the first example, but with a total length of 1 km and a 17 W alternatively π phase-shifted sech soliton train representing the bit sequence 10110111. SPC undoes soliton interactions and pulse distortions better than TPC in this case, while the hybrid scheme performs slightly better than SPC. This can be attributed to the fact that the hybrid scheme has more phase conjugation stages for the same total length. The hybrid scheme, however, can also compensate for the Raman-induced frequency shift, which cannot be compensated by SPC alone. The mean frequency shift of the TPC output is calculated to be +0.032 THz, that of the SPC output is -0.16 THz, while that of the hybrid scheme is only -0.027 THz.

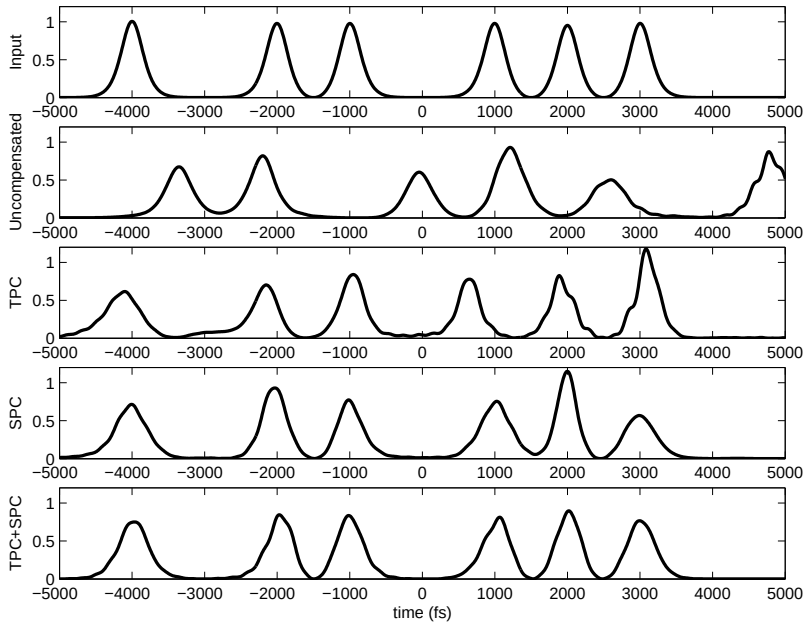

Figure 3.3: Input and output pulses with and without compensation schemes, when multiple 17 W 200 fs solitons propagates for a total distance of 1 km.

3.4 Conclusion

In conclusion, we have proven that SPC can compensate for all the considered linear and nonlinear distortions to optical pulses if loss and intrapulse Raman scattering can be neglected. Moreover, SPC and a hybrid scheme combining TPC and SPC are both shown numerically to offer better compensation of pulse distortions and soliton interactions than TPC for femtosecond pulses.

Bibliography

[1] A. Yariv, D. Fekete, and D. M. Pepper, Opt. Lett. **4**, 52 (1979).

[2] R. A. Fisher, B. R. Suydam, and D. Yevick, Opt. Lett. **8**, 611 (1983).

[3] S. Chi and S. F. Wen, Opt. Lett. **19**, 1705 (1994).

[4] A. M. Weiner, D. E. Leaird, D. H. Reitze, and E. G. Paek, IEEE J. Quantum Electron. **28**, 2251 (1992).

[5] C. Chang, H. P. Sardesai, and A. M. Weiner, Opt. Lett. **23**, 283 (1998).

[6] F. G. Omenetto, A. J. Taylor, M. D. Moores, and D. H. Reitze, Opt. Lett. **26**, 938 (2001).

[7] M. Tsang, D. Psaltis, and F. G. Omenetto, Opt. Lett. **28**, 1873 (2003).

[8] J. Pina, B. Abueva, and G. Goedde, Opt. Commun. **176**, 397 (2000).

[9] G. P. Agrawal, *Nonlinear Fiber Optics* (Academic Press, San Diego, 2001).

[10] D. A. B. Miller, Opt. Lett. **5**, 300 (1980).

[11] D. Marom, D. Panasenko, R. Rokitski, P. Sun, and Y. Fainman, Opt. Lett. **25**, 132 (2000).

[12] W. Forysiak and N. J. Doran, Electron. Lett. **30**, 154 (1994).

Chapter 4

Spectral phase conjugation with cross-phase modulation compensation

4.1 Introduction

Spectral phase conjugation (SPC) [1] is the phase conjugation of individual spectral components of an optical waveform, which is equivalent to phase conjugation and time reversal of the pulse envelope. Joubert *et al.* prove that midway SPC can compensate for all chromatic dispersion [2]. In the previous chapter we prove that midway SPC can simultaneously compensate for self-phase modulation (SPM), self-steepening and dispersion [3]. The physical implementation of SPC is first suggested by Miller using short-pump four-wave mixing (FWM) [1], and later demonstrated using photon echo [4, 5], spectral hole burning [6, 7], temporal holography [2], spectral holography [8], and spectral three-wave mixing (TWM) [9]. The FWM scheme is especially appealing to real-world applications such as communications and ultrashort pulse delivery due to its simple setup. However, low conversion efficiency and parasitic Kerr effects make a practical implementation difficult.

In this chapter we derive an accurate expression for the output idler when the conversion efficiency, defined as the output idler energy divided by the input signal energy, is high. We prove that if signal amplification is considered, the SPC process remains intact and the conversion efficiency can grow exponentially with respect to the cross-fluence of the two pump pulses, compared with a quadratic growth predicted in Ref. [1].

As the theoretical conversion efficiency approaches 100%, which is required for the purpose of nonlinearity compensation, parasitic effects begin to hamper the efficiency and accuracy of SPC. The main parasitic effect is cross-phase modulation (XPM) due to the strong pump, a problem that similarly plagues conventional temporal phase conjugation schemes [10]. We suggest a novel method to compensate for XPM by adjusting the phases of the pump pulses appropriately. We show that in theory, this method can fully compensate for the XPM effect.

Finally, numerical analysis is performed to confirm our predictions about the conversion efficiency and

XPM compensation. Pump depletion is also addressed by full three-dimensional simulations.

4.2 Spectral phase conjugation by four-wave mixing

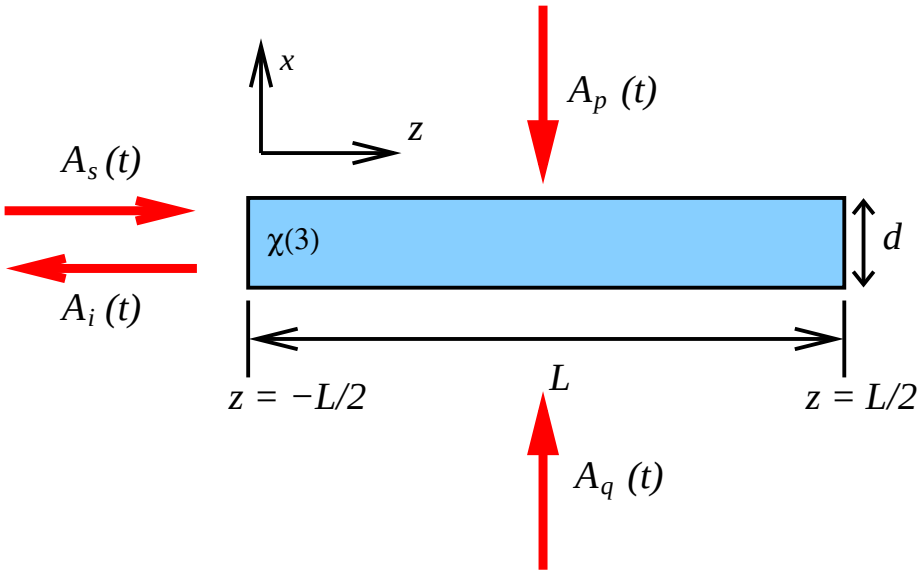

Figure 4.1: Setup of SPC by four-wave mixing. $A_s(t)$ is the signal pulse, $A_p(t)$ and $A_q(t)$ are the pump pulses, and $A_i(t)$ is the backward-propagating idler pulse. (After Ref. [1])

The configuration of spectral phase conjugation by four-wave mixing introduced in Ref. [1] is drawn in Fig. 4.1. A_p and A_q are the envelopes of the pump pulses propagating downward and upward, respectively. A_s is the forward-propagating signal envelope; and A_i is the backward-propagating idler envelope. The coupled-mode equations that govern A_p, A_q, A_s and A_i can be derived from the wave equation and are given by

$$-\frac{\partial A_p}{\partial x}+\frac{1}{v_x}\frac{\partial A_p}{\partial t} = j\gamma[2A_sA_iA_q^*+(|A_p|^2+2|A_q|^2+2|A_s|^2+2|A_i|^2)A_p], \tag{4.1}$$

$$\frac{\partial A_q}{\partial x}+\frac{1}{v_x}\frac{\partial A_q}{\partial t} = j\gamma[2A_sA_iA_p^*+(2|A_p|^2+|A_q|^2+2|A_s|^2+2|A_i|^2)A_q], \tag{4.2}$$

$$\frac{\partial A_s}{\partial z}+\frac{1}{v}\frac{\partial A_s}{\partial t} = j\gamma[2A_pA_qA_i^*+(2|A_p|^2+2|A_q|^2+|A_s|^2+2|A_i|^2)A_s], \tag{4.3}$$

$$-\frac{\partial A_i}{\partial z}+\frac{1}{v}\frac{\partial A_i}{\partial t} = j\gamma[2A_pA_qA_s^*+(2|A_p|^2+2|A_q|^2+2|A_s|^2+|A_i|^2)A_i], \tag{4.4}$$

$$\gamma = \frac{3\omega_0\chi^{(3)}}{8cn_0}, \tag{4.5}$$

where v_x and v are group velocities in the x direction and the z direction, respectively, and n_0 is the refractive index. Diffraction and group-velocity dispersion are neglected. The spatial dependence of A_p on z can also be suppressed if the illumination is uniform in z and undepleted. If we further assume that the thickness of the medium d is much smaller than the pump pulse width, then the dependence on the x dimension can also

be neglected.

The zeroth-order solution is the linear propagation of the incoming waves. Let the zeroth-order solution be

$$A_p^{(0)}(x,t) = A_p(t), \tag{4.6}$$

$$A_q^{(0)}(x,t) = A_q(t), \tag{4.7}$$

$$A_s^{(0)}(z,t) = F(t-\frac{z}{v}), \tag{4.8}$$

$$A_i^{(0)}(z,t) = 0. \tag{4.9}$$

The first-order solution can then be obtained by substituting the zeroth-order solution into the right-hand side of Eqs. (4.3) and (4.4). Each of Eqs. (4.1)−(4.4) has a single wave mixing term (first term on the right-hand side) and four phase modulation terms, which generally distort the pulses. With the subsitutions only Eq. (4.4) has a nonzero wave mixing term, and the output idler $A_i(-\frac{L}{2},t)$ in the first order is shown to be the SPC of the input signal [1],

$$A_i^{(1)}(-\frac{L}{2},t) = jF^*(-t+\frac{L}{2v})\int_{-\infty}^{\infty} 2\gamma v A_p(t')A_q(t')dt', \tag{4.10}$$

and the conversion efficiency is

$$\eta^{(1)} \equiv \frac{\int_{-\infty}^{\infty}|A_i^{(1)}(-\frac{L}{2},t')|^2dt'}{\int_{-\infty}^{\infty}|A_s^{(1)}(-\frac{L}{2},t')|^2dt'} = [\int_{-\infty}^{\infty}|2\gamma v A_p(t')A_q(t')|dt']^2, \tag{4.11}$$

assuming that either of the pump pulses A_p and A_q is much shorter than the input signal F and the medium is long enough to contain the signal. Conceptually, the short pump pulses take a "snapshot" of the signal spatial profile, which is reproduced as the idler. Since the idler has the same spatial profile as the signal but propagates backwards, the time profile is reversed.

To summarize, in order to perform accurate SPC, the following conditions should be satisfied:

$$\frac{L}{v} >> T_s >> (T_p \text{ or } T_q) >> \frac{d}{v_x}, \tag{4.12}$$

where T_s is the signal pulse width, and T_p and T_q are the pulse widths of the two pumps.

4.3 High conversion efficiency with signal amplification

When the conversion efficiency is high, mixing of the pump and the generated idler can also amplify the signal, as in the case of parametric amplification. In this section we derive accurate expressions for the output idler and the conversion efficiency in such a case. Assuming that the pump pulses are short, unchirped,

and undepleted, and phase modulation terms are neglected, we can derive a closed-form solution for the conversion efficiency. Eqs. (4.3) and (4.4) then become

$$\begin{aligned} v\frac{\partial A_s(z,t)}{\partial z}+\frac{\partial A_s(z,t)}{\partial t} &= jg(t)A_i^*(z,t), && (4.13)\\ -v\frac{\partial A_i(z,t)}{\partial z}+\frac{\partial A_i(z,t)}{\partial t} &= jg(t)A_s^*(z,t), && (4.14)\\ \text{where } g(t) &= 2\gamma v A_p(t)A_q(t). && (4.15) \end{aligned}$$

We first take the complex conjugate of Eq. (4.14),

$$-v\frac{\partial A_i^*(z,t)}{\partial z}+\frac{\partial A_i^*(z,t)}{\partial t}=-jg^*(t)A_s(z,t), \quad (4.16)$$

and let $\tilde{A}_s$ and $\tilde{A}_i$ be the Fourier transforms of A_s and A_i^* with respect to z, respectively,

$$\begin{aligned} \tilde{A}_s(\kappa,t) &= \int_{-\infty}^{\infty} A_s(z,t)\exp(-j\kappa z)dz, && (4.17)\\ \tilde{A}_i(\kappa,t) &= \int_{-\infty}^{\infty} A_i^*(z,t)\exp(-j\kappa z)dz. && (4.18) \end{aligned}$$

Note that $\tilde{A}_i$ is the Fourier transform of the complex conjugate of A_i. Eqs. (4.13) and (4.16) become

$$\begin{aligned} j\kappa v\tilde{A}_s+\frac{\partial \tilde{A}_s}{\partial t} &= jg(t)\tilde{A}_i, && (4.19)\\ -j\kappa v\tilde{A}_i+\frac{\partial \tilde{A}_i}{\partial t} &= -jg^*(t)\tilde{A}_s. && (4.20) \end{aligned}$$

We multiply both sides of Eq. (4.19) by $\exp(j\kappa vt)$ and both sides of Eq. (4.20) by $\exp(-j\kappa vt)$,

$$\begin{aligned} \exp(j\kappa vt)(j\kappa v\tilde{A}_s+\frac{\partial \tilde{A}_s}{\partial t}) &= jg(t)\exp(j\kappa vt)\tilde{A}_i, && (4.21)\\ \exp(-j\kappa vt)(-j\kappa v\tilde{A}_i+\frac{\partial \tilde{A}_i}{\partial t}) &= -jg^*(t)\exp(-j\kappa vt)\tilde{A}_s, && (4.22) \end{aligned}$$

or equivalently,

$$\begin{aligned} \frac{\partial}{\partial t}[\exp(j\kappa vt)\tilde{A}_s] &= jg(t)\exp(j\kappa vt)\tilde{A}_i, && (4.23)\\ \frac{\partial}{\partial t}[\exp(-j\kappa vt)\tilde{A}_i] &= -jg^*(t)\exp(-j\kappa vt)\tilde{A}_s. && (4.24) \end{aligned}$$

Then we make another set of substitutions,

$$\begin{aligned} A(\kappa,t) &= \exp(j\kappa vt)\tilde{A}_s=\exp(j\kappa vt)\int_{-\infty}^{\infty} A_s(z,t)\exp(-j\kappa z)dz, && (4.25)\\ B(\kappa,t) &= \exp(-j\kappa vt)\tilde{A}_i=\exp(-j\kappa vt)\int_{-\infty}^{\infty} A_i^*(z,t)\exp(-j\kappa z)dz, && (4.26) \end{aligned}$$

Eqs. (4.23) and (4.24) become

$$\frac{\partial A}{\partial t} = jg(t)\exp(2j\kappa\nu t)B, \tag{4.27}$$

$$\frac{\partial B}{\partial t} = -jg^*(t)\exp(-2j\kappa\nu t)A. \tag{4.28}$$

The exponential terms on the right-hand side have a frequency $2\kappa\nu$. To estimate the magnitude of this frequency, it is best to first consider the linear propagation of the signal and idler envelopes, before wave mixing occurs,

$$\nu\frac{\partial A_s}{\partial z} + \frac{\partial A_s}{\partial t} = 0, \tag{4.29}$$

$$-\nu\frac{\partial A_i}{\partial z} + \frac{\partial A_i}{\partial t} = 0. \tag{4.30}$$

Fourier transforms in z as well as t give the dispersion relation for the envelopes,

$$|\kappa\nu| = |\Omega|, \tag{4.31}$$

which is consistent with the definition of group velocity, $\nu = \frac{d\omega}{dk}$. Ω is the frequency variable in taking the temporal Fourier transform of the signal and idler envelopes, and has a maximum magnitude $\sim 1/T_s$. From Eqs. (4.27) and (4.28) it can be observed that wave mixing does not alter the spatial bandwidth of the envelopes, therefore κ has the same order of magnitude throughout, and $\kappa\nu \sim 1/T_s << (1/T_p \text{ or } 1/T_q)$. $g(t)$ has a duration shorter than both T_p and T_q, so $\exp(2j\kappa\nu t)$ oscillates relatively slowly compared to $g(t)$. Say $g(t)$ is centered at $t = 0$, we can then make the assumption

$$g(t)\exp(2j\kappa\nu t) \approx g(t). \tag{4.32}$$

The coupled-mode equations (4.27) and (4.28) become

$$\frac{\partial A}{\partial t} = jg(t)B, \tag{4.33}$$

$$\frac{\partial B}{\partial t} = -jg^*(t)A. \tag{4.34}$$

The initial condition is

$$A_s(z, -\frac{L}{2\nu}) = F(-\frac{L}{2\nu} - \frac{z}{\nu}), \tag{4.35}$$

$$A_i(z, -\frac{L}{2\nu}) = 0. \tag{4.36}$$

The initial condition for A and B can then be obtained from the substitutions, Eqs. (4.25) and (4.26). Define $g(t) = |g(t)| \exp j\theta(t)$, and assume that $\theta(t)$ is a constant. Eqs. (4.33) and (4.34) can now be solved to give

$$A(\kappa, t) = A(\kappa, -\frac{L}{2v}) \cosh[\int_{-\frac{L}{2v}}^{t} |g(t')| dt'], \tag{4.37}$$

$$B(\kappa, t) = -jA(\kappa, -\frac{L}{2v}) \exp(-j\theta) \sinh[\int_{-\frac{L}{2v}}^{t} |g(t')| dt']. \tag{4.38}$$

The final solution for A_s and A_i is

$$A_s(z, t) = F(t - \frac{z}{v}) \cosh[\int_{-\frac{L}{2v}}^{t} |g(t')| dt'], \tag{4.39}$$

$$A_i(z, t) = jF^*(-t - \frac{z}{v}) \exp(j\theta) \sinh[\int_{-\frac{L}{2v}}^{t} |g(t')| dt']. \tag{4.40}$$

As the idler exits the medium at $z = -\frac{L}{2}$ and $t = \frac{L}{2v}$, the pump pulses have long gone, hence the upper integral limit can be effectively replaced by ∞. The lower limit can also be replaced by $-\infty$, since the pump pulses have not arrived when the signal enters the medium at $t = -\frac{L}{2v}$. Hence

$$A_i(-\frac{L}{2}, t) = jF^*(-t + \frac{L}{2v}) \exp(j\theta) \sinh[\int_{-\infty}^{\infty} |g(t')| dt']. \tag{4.41}$$

This solution is consistent with Eq. (4.10), the first-order approximation in the limit of small gain. The conversion efficiency is

$$\eta \equiv \frac{\int_{-\infty}^{\infty} |A_i(-\frac{L}{2}, t')|^2 dt'}{\int_{-\infty}^{\infty} |A_s(-\frac{L}{2}, t')|^2 dt'} = \sinh^2[\int_{-\infty}^{\infty} |2\gamma v A_p(t') A_q(t')| dt']. \tag{4.42}$$

This result shows the exponential dependence of the conversion efficiency on the cross fluence of the two pump pulses.

4.4 Cross-phase modulation compensation

With the undepleted pump approximation, the main nonlinear effect besides wave mixing is the cross-phase modulation on the signal and the idler imposed by the strong pump. Mathematically this can be observed from Eq. (4.3) and Eq. (4.4), where the XPM terms are the largest apart from the wave mixing terms. These effects are previously neglected in deriving Eq. (4.42).

With XPM terms included, the coupled-mode equations become

$$v\frac{\partial A_s(z,t)}{\partial z}+\frac{\partial A_s(z,t)}{\partial t} = jg(t)A_i^*(z,t)+jc(t)A_s(z,t), \tag{4.43}$$

$$-v\frac{\partial A_i(z,t)}{\partial z}+\frac{\partial A_i(z,t)}{\partial t} = jg(t)A_s^*(z,t)+jc(t)A_i(z,t), \tag{4.44}$$

$$\text{where } g(t) = 2\gamma v A_p(t)A_q(t), \tag{4.45}$$

$$c(t) = 2\gamma v\left[|A_p(t)|^2+|A_q(t)|^2\right]. \tag{4.46}$$

XPM effects are detrimental to the SPC efficiency and accuracy if a high conversion efficiency is desired, as it introduces a time-dependent detuning factor to the wave mixing process.

To solve Eqs. (4.43) and (4.44), we follow similar procedures as in the previous section by performing a Fourier transform with respect to z and making the following substitutions:

$$A(\kappa,t) = \exp[j\kappa v t - j\int_{-\infty}^{t}c(t')dt']\int_{-\infty}^{\infty}A_s(z,t)\exp(-j\kappa z)dz, \tag{4.47}$$

$$B(\kappa,t) = \exp[-j\kappa v t + j\int_{-\infty}^{t}c(t')dt']\int_{-\infty}^{\infty}A_i^*(z,t)\exp(-j\kappa z)dz. \tag{4.48}$$

We obtain the following:

$$\frac{\partial A}{\partial t} = jg(t)\exp[-2j\int_{-\infty}^{t}c(t')dt']B, \tag{4.49}$$

$$\frac{\partial B}{\partial t} = -jg^*(t)\exp[2j\int_{-\infty}^{t}c(t')dt']A. \tag{4.50}$$

Eqs. (4.49) and (4.50) are difficult to solve analytically, but a special case exists when the phase of $g(t)$ exactly cancels the XPM term,

$$\theta(t) = \theta_0+2\int_{-\infty}^{t}c(t')dt'. \tag{4.51}$$

Eqs. (4.49) and (4.50) are then reduced to

$$\frac{\partial A}{\partial t} = j|g(t)|\exp(j\theta_0)B, \tag{4.52}$$

$$\frac{\partial B}{\partial t} = -j|g(t)|\exp(-j\theta_0)A. \tag{4.53}$$

The general solution is

$$A_s(z,t) = F(t-\frac{z}{v})\exp[j\int_{-\infty}^{t}c(t')dt']\cosh[\int_{-\infty}^{t}|g(t')|dt'], \tag{4.54}$$

$$A_i(z,t) = jF^*(-t-\frac{z}{v})\exp[j\theta_0+j\int_{-\infty}^{t}c(t')dt']\sinh[\int_{-\infty}^{t}|g(t')|dt'], \tag{4.55}$$

and the output idler is

$$A_i(-\frac{L}{2},t) = jF^*(-t+\frac{L}{2v})\exp[j\theta_0 + j\int_{-\infty}^{\infty} c(t')dt']\sinh[\int_{-\infty}^{\infty}|g(t')|dt']. \tag{4.56}$$

This solution is the same as Eq. (4.41), the output idler without considering XPM, apart from a constant phase term $\exp[\int_{-\infty}^{\infty} c(t')dt']$, which does not affect the pulse waveform. If we let $A_p(t) = |A_p(t)|\exp[j\theta_p(t)]$ and $A_q(t) = |A_q(t)|\exp[j\theta_q(t)]$, then from Eq. (4.51) the actual phase adjustments to the pump pulses are given by

$$\theta_p(t) + \theta_q(t) = \theta_0 + 4\gamma v\int_{-\infty}^{t} |A_p(t')|^2 + |A_q(t')|^2 dt'. \tag{4.57}$$

Qualitatively, by adjusting the phases of the pump pulses according to Eq. (4.57), we can utilize the wave mixing process to introduce phase variations to the signal and the idler, so that the cross-phase modulation can be exactly canceled. In practice, the phase variation of the pump pulses can be introduced by various pulse shaping methods, for example, using a 4f pulse shaper [12]. The phase correction can be introduced to either or both of the pump pulses as long as the condition in Eq. (4.57) is satisfied.

4.5 Numerical analysis

To verify our derivations, we obtain numerical solutions of Eqs. (4.43) and (4.44) by a multiscale approach. In this approach successively higher-order solutions are obtained by substituting lower-order solutions into the right-hand side of the equations, until convergence is reached. For the following simulations, the pump and the input signal are assumed to be

$$A_p(t) = A_q(t) = \exp\big(-\frac{t^2}{2T_p^2}\big), \tag{4.58}$$

$$F(\tau) = A_{s0}\Big\{\exp\big[-\frac{1+j}{2}(\frac{\tau+2T_s}{T_s})^2\big] + \frac{1}{2}\exp\big[-\frac{1}{2}(\frac{\tau-2T_s}{T_s})^2\big]\Big\}. \tag{4.59}$$

To confirm that the SPC process is still accurate when the conversion efficiency is high, we first consider the case in which XPM is neglected. Figure 4.2 shows a plot of the amplitude and the phase of the output idler pulse envelope $A_i(-\frac{L}{2},t)$ compared with the input signal $A_s(-\frac{L}{2},t)$, using parameters similar to Ref. [9] and polydiacetylene, a material with the highest off-resonant third-order nonlinearity reported [11], as the wave mixing medium. The conversion efficiency is 100% with a total pump energy of only 12.8 nJ from the numerical analysis. From Fig. 4.2 it is clear that the output idler is an exact, time-reversed and phase-conjugated replica of the input signal.

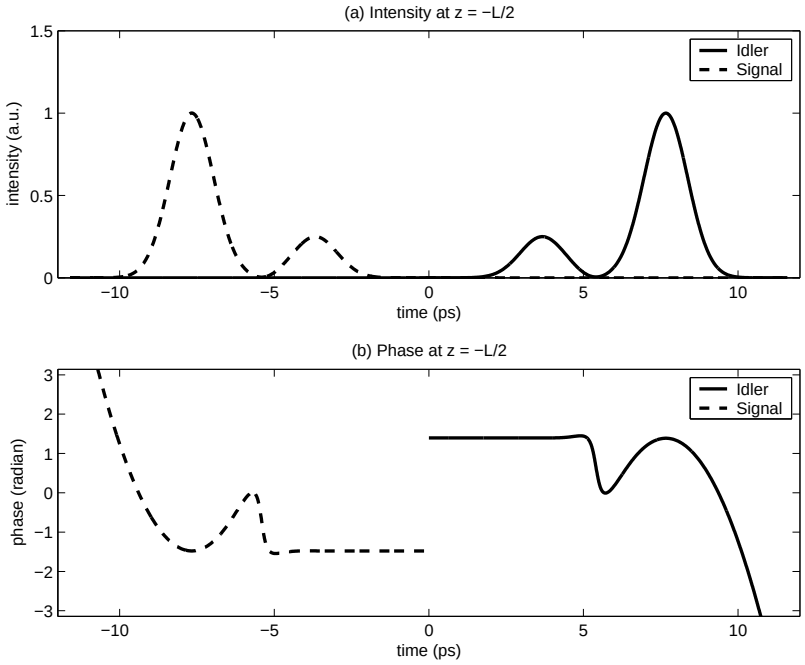

Figure 4.2: (a) Amplitude and (b) phase of output idler (solid lines) $A_i(-\frac{L}{2},t)$ compared with input signal (dash lines) $A_s(-\frac{L}{2},t)$. XPM is neglected in this example. As predicted, the output idler is time-reversed and phase-conjugated with respect to the input signal. Parameters used are $n_2 = 1\times10^{-11}$ cm^2/W, $n_0 = 1.7$, $\lambda_0 = 800$ nm, $L = 2$ mm, $d = 5$ μm, T_s = 1 ps, T_p = 100 fs, E_p = 12.8 nJ, pump fluence = $\frac{E_p}{Ld}$. Conversion efficiency is 100%.

4.5.1 Conversion efficiency

Figure 4.3 is a plot of conversion efficiencies against total pump energy obtained from theory and simulations, using the same parameters as for the previous numerical example. The dotted curve is a plot of Eq. (4.11), the result from Ref. [1]. The solid curve is a plot of Eq. (4.42), the conversion efficiency obtained by including signal amplification but neglecting XPM. The crosses are results from a numerical simulation of Eqs. (4.13) and (4.14), validating the closed-form solution we derive. The triangles are results from a numerical simulation of Eqs. (4.3) and (4.4), which also include phase modulation terms. It clearly shows that XPM becomes detrimental to the conversion efficiency as the pump energy increases. Finally, the circles are a numerical simulation that includes all nonlinear terms and XPM compensation according to Eq. (4.57). The numerical results confirm the accuracy of our conversion efficiency derivation, demonstrates the detrimental XPM effect on conversion efficiency, and proves that our compensation method can indeed undo the XPM effect.

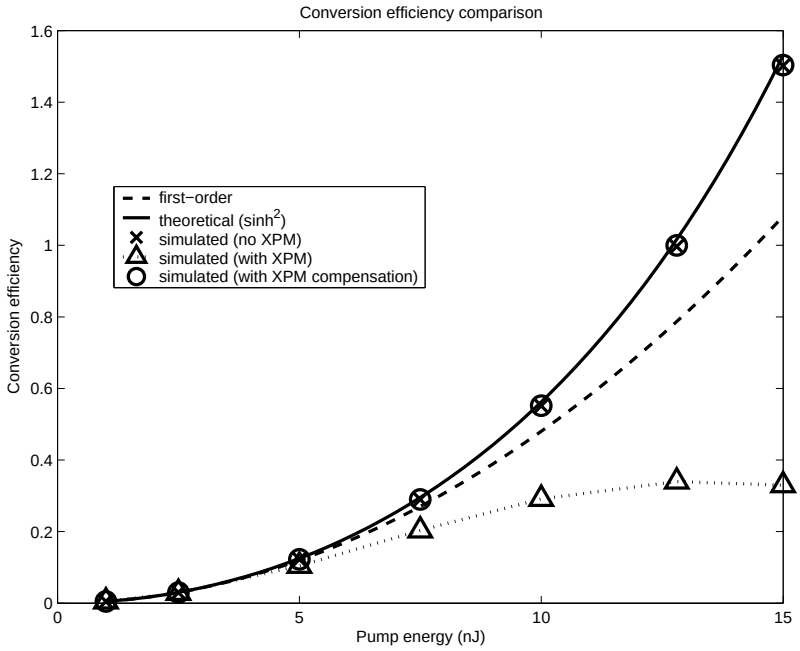

Figure 4.3: Conversion efficiencies from simulations compared with predictions from first-order analysis and coupled-mode theory. Simulation results agree well with coupled-mode theory. See caption of Fig. 4.2 for parameters used.

4.5.2 Demonstration of cross-phase modulation compensation

Figure 4.4(a) and (b) plot the output idler $A_i(-\frac{L}{2},t)$ compared with the SPC of the input signal $A_s^*(-\frac{L}{2},-t)$, with XPM included, using the same parameters as before. The efficiency is reduced from 100% to 34% and the accuracy of the SPC operation suffers due to the XPM effect. Figure 4.4(c) and (d) plots the same data, but with the phase of the pump pulses adjusted according to Eq. (4.57) and plotted in Fig. 4.5. The accuracy of the SPC operation is restored by the XPM compensation, and the efficiency is back to 100%.

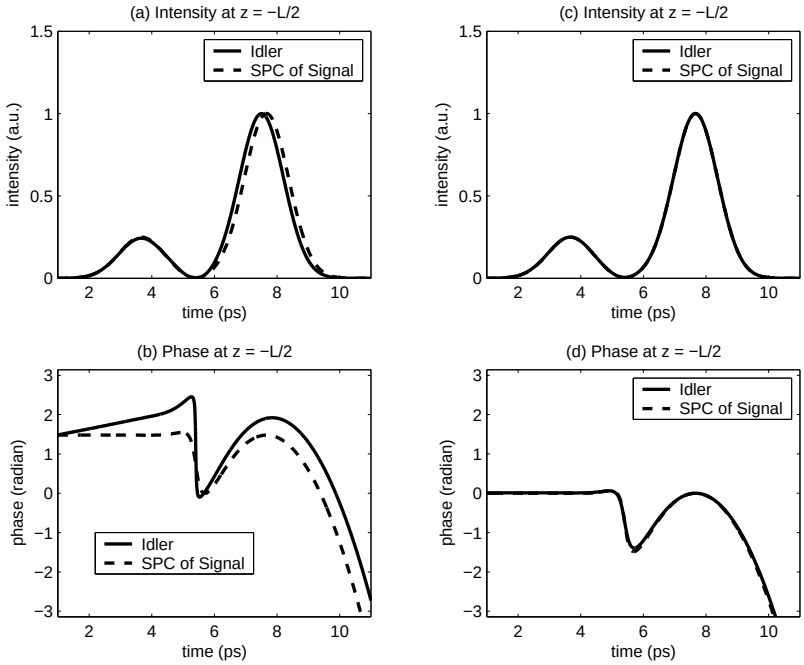

Figure 4.4: (a) and (b) plot the *normalized* amplitude and phase of the output idler $A_i(-\frac{L}{2},t)$ compared to the SPC of the input signal $A_s^*(-\frac{L}{2},-t)$, respectively, when XPM is present. The amplitude plots are normalized with respect to their peaks. The output idler is distorted and the conversion efficiency is only 34%, much lower than the theoretical efficiency 100%. (c) and (d) plot the same data, but with XPM compensation. The efficiency is back to 100% and the accuracy is restored.

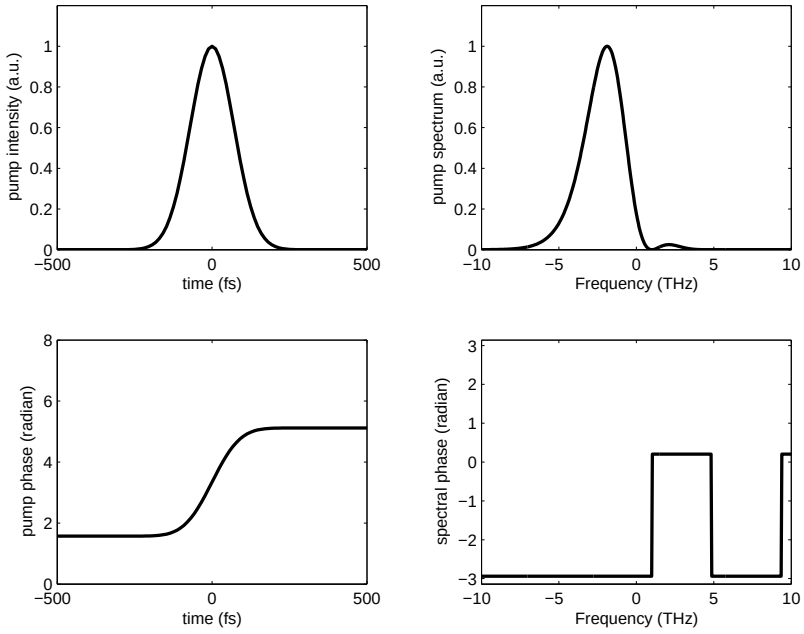

Figure 4.5: Plots of amplitude and phase of one pump pulse with ideal phase adjustment according to Eq. (4.57) in the time and frequency domain. Top-left: temporal envelope; bottom-left: temporal phase; top-right: envelope spectrum; bottom-right: spectral phase. The simple pulse shape should be easily produced by many pulse shaping methods.

4.6 Beyond the basic assumptions

4.6.1 Pump depletion

All of our derivations so far assume that the pump is undepleted. If the signal becomes comparable to the pump, then the pump can no longer sustain a fixed gain, which begins to depend on the signal field across z. Mathematically this means that the right-hand sides of Eqs. (4.1) and (4.2) become comparable to the left-hand sides. In this case the pump would be depleted, and we can no longer expect the SPC operation to be accurate. To avoid pump depletion we therefore require the right-hand sides of Eqs. (4.1) and (4.2) to be much smaller than the left-hand sides, or roughly speaking,

$$|A_p| \quad >> \quad 2\gamma|A_s||A_i||A_q|d, \tag{4.60}$$

$$E_s \quad << \quad \frac{n_0 d T_s}{\eta_0 \gamma \sqrt{\eta}}. \tag{4.61}$$

where E_s is the signal energy and η_0 is the free-space impedance. The signal energies should be much smaller than the rough signal energy upper limits established by Eq. (4.61) in order to avoid pump depletion. A low signal energy also avoids distortion due to SPM.

To investigate the effect of pump depletion, we perform three-dimensional simulations in x, z, t by numerically solving Eqs. (4.1), (4.2), (4.3), and (4.4) simultaneously.

The first example assumes the same parameters as before, with a signal energy of 1 pJ, much below the pump depletion limit, calculated to be 1 nJ from Eq. (4.61). XPM is included along with XPM compensation. The conversion efficiency from the simulation drops slightly to 92% due to a finite medium thickness. However, the SPC process still remains accurate with the inclusion of the x dimension.

On the other hand, with a signal energy of 5 nJ, much above the pump depletion limit 1 nJ, Fig. 4.6 plots the output idler from the same simulation. As can be seen from the movie, the pump pulses are highly depleted, and from Fig. 4.6 it can be seen that the top of the idler is flattened due to gain saturation. The conversion efficiency is reduced to 32%.

4.6.2 Other nonideal conditions

Besides pump depletion, other nonideal conditions also affect the accuracy of the SPC process. If the pump pulses are not short enough, then from the first-order solution in Ref. [1] it can be seen that the output pulse becomes the convolution of the pump and the signal. The medium also needs to be long enough to contain the whole signal pulse, otherwise the output idler will be truncated.

If the medium is thick, the x dimension can no longer be ignored. $A_p(t)$ and $A_q(t)$ should be replaced by $A_p(t + x/v_x)$ and $A_q(t - x/v_x)$, respectively, which do not directly affect the generated idler temporal pulse shape. However, the idler beam will acquire additional transverse patterns in x, which will distort the pulse shape if diffraction or waveguiding is also taken into account. Another problem with a thick medium is that

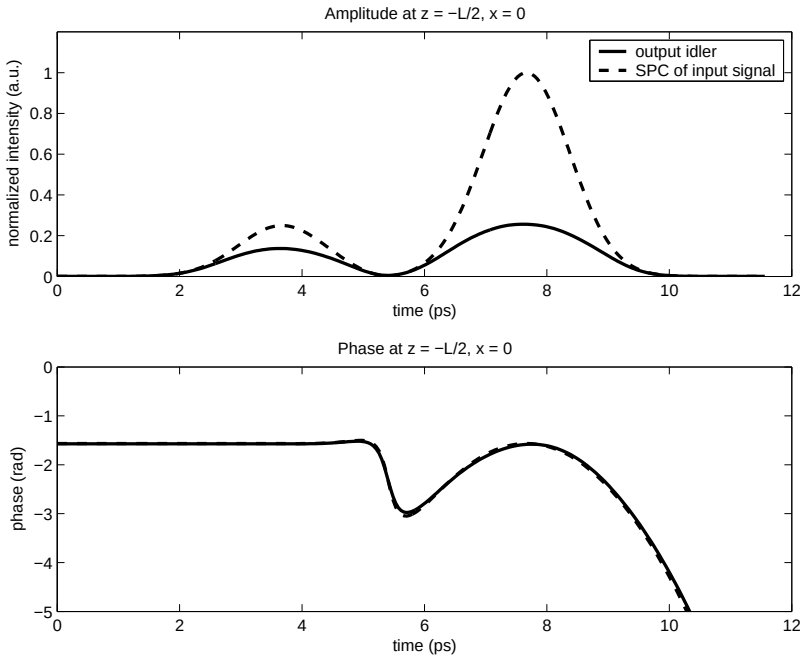

Figure 4.6: Amplitude and phase of output idler and input signal for the wave mixing process, with a signal energy of 5 nJ, much above the pump depletion limit, to demonstrate the effect of pump depletion.

SPM will chirp the pump pulses and reduce the SPC efficiency and accuracy. That said, since SPM is not directly involved with the wave mixing process, it can be precompensated by pulse shaping if it becomes a problem.

4.7 Conclusion

In conclusion, we have derived new solutions for the spectral phase conjugation process by four-wave mixing. When signal amplification is significant, the SPC process has been shown to remain accurate and achieve higher efficiency. We have also proposed a method to compensate for XPM, which severely reduces the efficiency and accuracy of SPC, by adjusting the phases of the pump pulses accordingly. With a higher predicted conversion efficiency and an effective method to compensate for XPM without sacrificing accuracy, we are hopeful that SPC by four-wave mixing can finally be experimentally implemented and utilized for real-world applications.

Bibliography

[1] D. A. B. Miller, Opt. Lett. **5**, 300 (1980).

[2] C. Joubert, M. L. Roblin, R. Grousson, Appl. Opt. **28**, 4604 (1989).

[3] M. Tsang, D. Psaltis, Opt. Lett. **28**, 1558 (2003).

[4] N. W. Carlson, L. J. Rothberg, A. G. Yodh, W. R. Babbitt, T. W. Mossberg, Opt. Lett. **8**, 483 (1983).

[5] V. L. da Silva, Y. Silberberg, J. P. Heritage, E. W. Chase, M. A. Saifi, M. J. Andrejco, Opt. Lett. **16**, 1340 (1991).

[6] A. Rebane, J. Aaviksoo, J. Kuhl, Appl. Phys. Lett. **54**, 93 (1989).

[7] S. Fraigne, J. P. Galaup, J. L. Le Gouet, B. Bousquet, L. Canioni, M. Joffre, J. P. Likforman, J. Opt. Soc. Am. B **20**, 1555 (2003).

[8] A. M. Weiner, D. E. Leaird, D. H. Reitze, Eung Gi Paek, IEEE J. Quantum Electron. **28**, 2251 (1992).

[9] D. Marom, D. Panasenko, R. Rokitski, P. Sun, Y. Fainman, Opt. Lett. **25**, 132 (2000).

[10] S. Wen, S. Chi, T. Chang, Opt. Lett. **19**, 939 (1994).

[11] R. Quintero-Torres, M. Thakur, J. Appl. Phys. **85**, 401 (1999).

[12] A. M. Weiner, Rev. Sci. Instrum. **71**, 1929 (2000).

Chapter 5

Spectral phase conjugation by quasi-phase-matched three-wave mixing

5.1 Introduction

Conventional phase conjugation schemes perform the so-called phase conjugation with spectral inversion [1]. The output of such schemes has a spectrum that is phase conjugated and spectrally inverted with respect to the input. In the time domain, this is equivalent to phase conjugation of the pulse envelope, so the scheme is also called temporal phase conjugation (TPC) [2]. A distinct kind of phase conjugation, which performs phase conjugation *without* spectral inversion, is first suggested by Miller [3]. The output spectrum of such a phase conjugation scheme is the phase conjugation of the input spectrum, and the scheme is therefore called spectral phase conjugation (SPC). In the time domain, the output pulse envelope is the phase conjugation and time reversal of the input pulse envelope.

While TPC can compensate for even-order dispersion [1], self-phase modulation [4], and intrapulse Raman scattering [5], SPC can simultaneously compensate for *all* chromatic dispersion [6], self-phase modulation, and self-steepening [2], thus making it attractive for ultrafast applications such as optical communications. The time reversal operation associated with SPC is also useful for signal processing [7].

The physical implementation of SPC is first suggested by Miller using short-pump four-wave mixing (FWM) [3], and later demonstrated, for example, using photon echo [8, 9], spectral hole burning [10, 11], temporal holography [6], spectral holography [12], and spectral three-wave mixing (TWM) [13]. The FWM scheme is especially appealing to real-world applications due to its simple setup, and its efficiency is recently shown to be significantly higher than previously considered [14]. However, the FWM scheme requires accurate synchronization of two short pump pulses, which may undermine its robustness. A setup that combines the elegant geometry of Miller's scheme and the robustness of TWM can therefore be advantageous. It is also of fundamental interest to investigate if the use of second-order nonlinearity can provide a higher efficiency than the FWM configuration.

5.2 Configuration

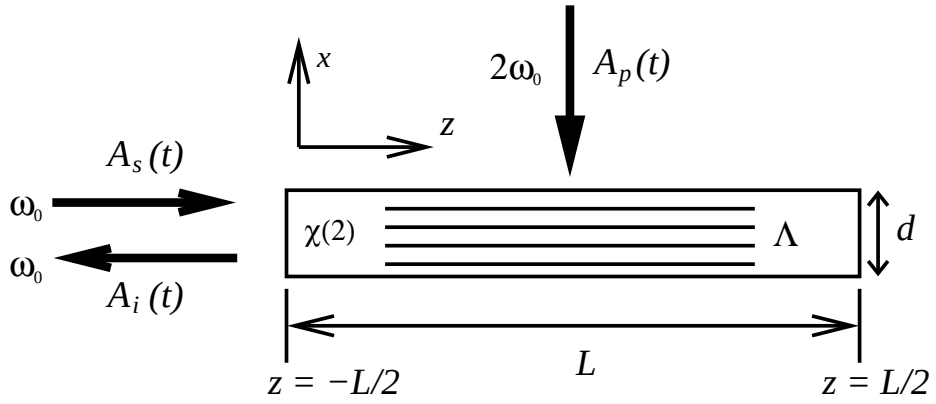

Figure 5.1: Geometry of SPC by quasi-phase-matched three-wave mixing. $A_s(t)$ is the incoming signal pulse with a carrier frequency ω_0, and $A_p(t)$ is the second-harmonic pump pulse. $A_i(t)$ is the generated idler pulse. Quasi-phase matching is achieved by a $\chi^{(2)}$ grating with period Λ along x.

The proposed configuration is shown in Fig. 5.1. It is similar to surface-emitting second-harmonic generation [15, 16], transverse-pumping parametric amplification [17], and transverse-pumping phase conjugation [18]. The difference in our proposed system is that the pump pulse $A_p(t)$ is much shorter than the signal pulse $A_s(t)$. Therefore, the pump pulse takes a "snapshot" of the signal pulse, and when phase matching is satisfied, the generated idler pulse $A_i(t)$ is a backward-propagating, phase-conjugated, and time-reversed replica of the input signal pulse. The second-harmonic pump pulse can be generated by conventional second-harmonic generation methods.

5.3 Theory

To achieve phase matching we must have

$$\mathbf{k}_s + \mathbf{k}_i = \mathbf{k}_p + \mathbf{K}, \tag{5.1}$$

where $\mathbf{k}_i$ is the wave vector of the idler, $\mathbf{k}_s$ is the wave vector of the signal, $\mathbf{k}_p$ is the wave vector of the pump, and $\mathbf{K} = \frac{2\pi}{\Lambda}\hat{\mathbf{x}}$ is the $\chi^{(2)}$ grating vector. In our geometry $\mathbf{k}_s = -\mathbf{k}_i$, so $\mathbf{K} = -\mathbf{k}_p$, or

$$\Lambda = \frac{\lambda_0(2\omega_0)}{n(2\omega_0)}, \tag{5.2}$$

where $\lambda_0(2\omega_0)$ is the free-space wavelength at $2\omega_0$ and $n(2\omega_0)$ is the refractive index at $2\omega_0$. In other words, the grating period should be equal to the second-harmonic wavelength in the medium, which is in general submicron. A $\chi^{(2)}$ grating with such a small period can be fabricated, for example, in AlGaAs/GaAs heterostructures [16, 19], asymmetric coupled quantum wells [20], poled-polymer waveguides [21], and KTP

crystals [22].

Notice that in our scheme the $\chi^{(2)}$ grating is only used to cancel the carrier wave vector of the pump pulse, while the additional wave vector due to the broad bandwidth of the pump pulse is accounted for in the coupled-mode formalism below. Provided that such quasi-phase matching is achieved, the coupled-mode equations of pulse envelopes A_p, A_s, and A_i can be derived from the wave equation, and are given by

$$-\frac{\partial A_p}{\partial x}+\frac{1}{v_x}\frac{\partial A_p}{\partial t}=2j\gamma\frac{n_0}{n(2\omega_0)}A_sA_i, \tag{5.3}$$

$$\frac{\partial A_q}{\partial x}+\frac{1}{v_x}\frac{\partial A_q}{\partial t}=2j\gamma\frac{n_0}{n(2\omega_0)}A_sA_i, \tag{5.4}$$

$$\frac{\partial A_s}{\partial z}+\frac{1}{v}\frac{\partial A_s}{\partial t}=j\gamma(A_p+A_q)A_i^*, \tag{5.5}$$

$$-\frac{\partial A_i}{\partial z}+\frac{1}{v}\frac{\partial A_i}{\partial t}=j\gamma(A_p+A_q)A_s^*, \tag{5.6}$$

$$\gamma=\frac{\omega_0\chi^{(2)}}{2cn_0}, \tag{5.7}$$

where A_q is the upward-propagating second-harmonic wave, which can be neglected in general but included here for completeness, v_x is the group velocity at $2\omega_0$ along x, v is the group velocity at ω_0 along z, and n_0 is the refractive index at ω_0. Diffraction and group-velocity dispersion are neglected.

If a waveguide structure is used, then γ should also include an overlapping factor that describes the overlapping extent of the signal and idler waveguide modes,

$$\gamma=\frac{\omega_0\chi^{(2)}}{2cn_0}\int d\mathbf{r}_\perp,\ \psi_s\psi_i \tag{5.8}$$

where ψ_s and ψ_i are the normalized waveguide mode profiles of the signal and the idler, respectively.

If the right-hand sides of Eqs. (5.3) and (5.4) are much smaller than the left-hand sides, then the pump can be assumed to be undepleted. Moreover, we can neglect the x dimension if the pump pulse spatial width v_xT_p is much longer than the thickness of the medium d. The resulting coupled-mode equations of A_s and A_i are

$$v\frac{\partial A_s(z,t)}{\partial z}+\frac{\partial A_s(z,t)}{\partial t}=jg(t)A_i^*(z,t), \tag{5.9}$$

$$-v\frac{\partial A_i(z,t)}{\partial z}+\frac{\partial A_i(z,t)}{\partial t}=jg(t)A_s^*(z,t), \tag{5.10}$$

$$g(t)=\gamma vA_p(t). \tag{5.11}$$

Equations (5.9) and (5.10) are completely identical to the equations that describe the signal and the idler in

the FWM geometry [14]. The boundary conditions are assumed to be

$$A_s(-\frac{L}{2},t) = F(t+\frac{L}{2v}), \tag{5.12}$$

$$A_i(\frac{L}{2},t) = 0. \tag{5.13}$$

Assuming that $g(t) = |g(t)|\exp(j\theta)$, θ is constant, and the pulse width of A_p is much shorter than that of A_s, Eqs. (5.9) and (5.10) can be solved using the same method described in Ref. [14]. The solution is then given by

$$A_s(z,t) = F(t-\frac{z}{v})\cosh[\int_{-\infty}^{t}|g(t')|dt'], \tag{5.14}$$

$$A_i(z,t) = jF^*(-t-\frac{z}{v})\exp(j\theta)\sinh[\int_{-\infty}^{t}|g(t')|dt']. \tag{5.15}$$

The idler exiting at $z = -\frac{L}{2}$ is

$$A_i(-\frac{L}{2},t) = jF^*(-t+\frac{L}{2v})\exp(j\theta)\sinh[\int_{-\infty}^{\infty}|\gamma v A_p(t')|dt']. \tag{5.16}$$

The conversion efficiency, defined as the input signal energy divided by the output idler energy, is

$$\eta \equiv \frac{\int_{-\infty}^{\infty}|A_i(-\frac{L}{2},t')|^2dt'}{\int_{-\infty}^{\infty}|A_s(-\frac{L}{2},t')|^2dt'} = \sinh^2[\int_{-\infty}^{\infty}|\gamma v A_p(t')|dt']. \tag{5.17}$$

Similar to the FWM configuration, the following conditions should be satisfied for accurate SPC operation:

$$\frac{L}{v} >> T_s >> T_p >> \frac{d}{v_x}, \tag{5.18}$$

where T_s is the pulse width of the signal.

5.4 Comparison with the FWM scheme

To compare the efficiency of the TWM scheme with that of the FWM scheme, we first compute the pump energy E_p required to achieve a certain conversion efficiency η by assuming that the pump pulse is a Gaussian,

$$A_p(t) = A_{p0}\exp(-\frac{t^2}{2T_p^2}), \tag{5.19}$$

$v = c/n_0$, and the cross-section area of the pump beam is Ld. E_p is then given by

$$E_p = \frac{n_0 Ld}{2\eta_0} \int |A_p(t')|^2 dt' \tag{5.20}$$

$$= \frac{n_0^5 Ld}{\sqrt{\pi}\eta_0 \omega_0^2 [\chi^{(2)}]^2 T_p} [\sinh^{-1}(\sqrt{\eta})]^2, \tag{5.21}$$

where η_0 is the free-space impedance. Compare this with the total pump energy required for the FWM configuration, assuming that the two pump pulses are identical,

$$E_p' = \frac{4n_0'^3 Ld}{3\eta_0 \omega_0 \chi^{(3)}} \sinh^{-1}(\sqrt{\eta}) \tag{5.22}$$

$$= \frac{n_0' Ld}{\omega_0 n_2} \sinh^{-1}(\sqrt{\eta}), \tag{5.23}$$

where n_0' is the refractive index of the $\chi^{(3)}$ medium. The TWM scheme is thus more efficient when

$$[\frac{\sqrt{\pi}}{\sinh^{-1}(\sqrt{\eta})}](\omega_0 T_p) \frac{\eta_0 [\chi^{(2)}]^2}{n_0^5} > \frac{n_2}{n_0'}. \tag{5.24}$$

For example, for $\lambda_0 = 800$ nm, $T_p = 100$ fs, a GaAs/AlGaAs heterostructure with $\chi^{(2)} \approx 50$ pm/V, $n_0 \approx 3$, $\eta = 100\%$, the left-hand side of Eq. (5.24) is about 10^{-14} cm^2/W, which is close to the n_2 of CS_2, but much lower than that of conjugated polymers ($\sim 10^{-11}$ cm^2/W [23]). That said, $\chi^{(2)}$ of asymmetric coupled GaAs/AlAs quantum wells can theoretically reach 30 nm/V in the far infrared regime [24], potentially giving rise to a much lower pump energy requirement. The TWM scheme also eliminates the need of the second pump pulse and avoids the difficulty in synchronizing two ultrashort pulses in a thin medium.

5.5 Numerical analysis

In order to confirm the validity of the approximations in our theoretical predictions, we perform numerical simulations of Eqs. (5.9) and (5.10), using GaAs/AlGaAs heterostructure as the nonlinear medium, a Gaussian pump pulse with $T_p = 100$ fs, and pump energy $E_p = 2.1$ μJ. The incoming signal is assumed to be

$$F(t) = A_{s0}\Big\{ -\exp\big[-\frac{1+j}{2}(\frac{t+2T_s}{T_s})^2\big] + \frac{1}{2}\exp\big[-\frac{1}{2}(\frac{t-2T_s}{T_s})^2\big]\Big\}, \tag{5.25}$$

with $T_s = 1$ ps. The calculated conversion efficiency is 100%, consistent with the theoretical efficiency from Eq. (5.17). The signal and idler pulse shapes from the numerical analysis are plotted in Fig. 5.2, which confirms that SPC can indeed be accurately performed by TWM. The required pump energy 2.1 μJ is much higher than that theorized in Ref. [14] for the FWM scheme using polydiacetylene ($\sim$ 10 nJ), but it is still much lower than the pump energy used in Ref. [13] ($\sim$ 1 mJ).

Using the same parameters, Fig. 5.3 plots the theoretical conversion efficiency calculated from Eq. (5.17)

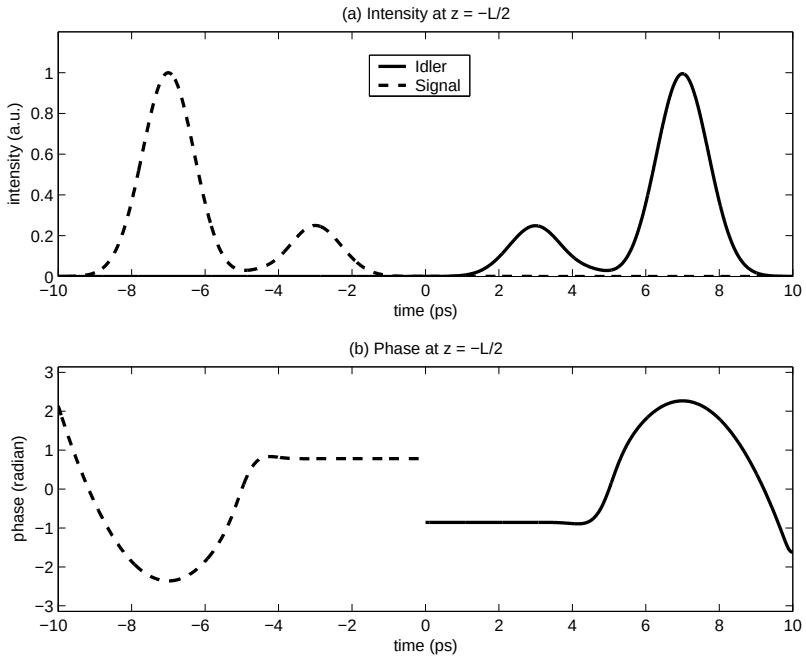

Figure 5.2: Plots of intensity and phase of incoming signal and output idler from numerical analysis. It is clear from the plots that the idler is a phase-conjugated and time-reversed replica of the signal, confirming our theoretical derivations. Parameters used are $\chi^{(2)} = 50$ pm/V, $n_0 = 3$, $L = 1$ mm, $d = 5$ μm, width in $y = d$, $E_p = 2.1$ μJ, pump fluence $= \frac{E_p}{Ld}$. For such dimensions waveguide confinement of the signal and the idler is necessary.

and that obtained from numerical analysis against the pump energy. The numerical results agree quite well with the theoretical prediction, although the former is slightly lower, due to slight deviation from the ideal conditions stated in Eq. (5.18).

5.6 Competing third-order nonlinearity

With a high pump intensity, competing third-order nonlinearity in the form of cross-phase modulation (XPM) can be detrimental to the SPC accuracy and efficiency in the same manner as for the FWM scheme [14]. One way to control XPM is by the same XPM compensation method described in Ref. [14], which uses the wave mixing process to introduce phase variations to the signal and the idler, so that the Kerr phase modulation due to the strong pump can be exactly canceled. The theoretical proof is very similar to the FWM case [14], and the pump phase adjustment is

$$\theta(t) = \theta_0 + \int_{-\infty}^{t} \frac{3\omega_0 v \chi^{(3)}}{2cn_0} |A_p(t')|^2 dt'. \tag{5.26}$$

This phase adjustment is an almost linear function of time, or equivalently a center frequency shift. Therefore, if this compensation method is used, the $\chi^{(2)}$ grating period should also be adjusted to account for the wave

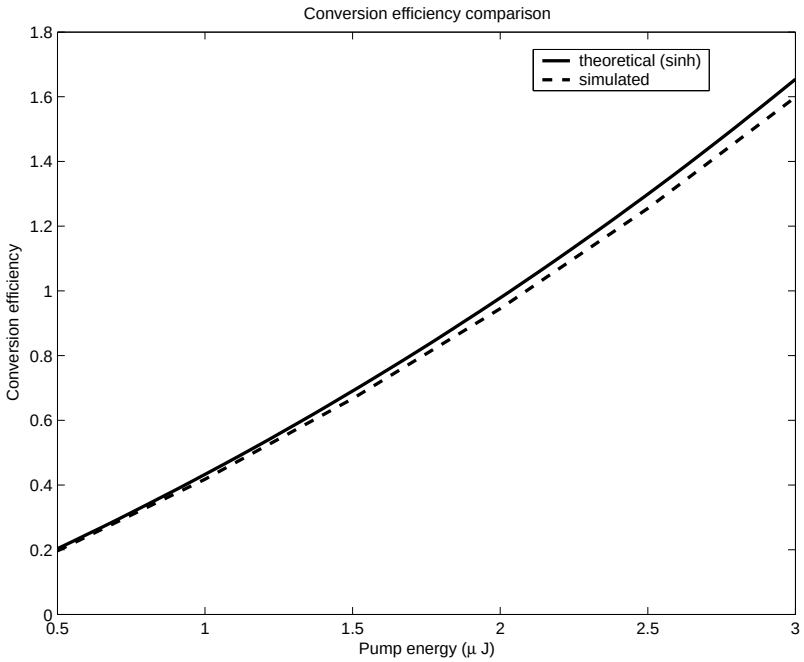

Figure 5.3: Theoretical conversion efficiency derived from Eq. (5.17) and that from numerical analysis plotted against pump energy. See caption of Fig. 5.2 for parameters used.

vector change due to the center frequency shift.

5.7 Conclusion

We have proposed a novel SPC scheme by the use of quasi-phase-matched TWM. The advantages of the TWM scheme over the FWM scheme include the elimination of the second pump pulse, higher conversion efficiency for certain parameters, and possible independent management of second-order and third-order nonlinearities.

Bibliography

[1] A. Yariv, D. Fekete, and D. M. Pepper, Opt. Lett. **4**, 52 (1979).

[2] M. Tsang, D. Psaltis, Opt. Lett. **28**, 1558 (2003).

[3] D. A. B. Miller, Opt. Lett. **5**, 300 (1980).

[4] R. A. Fisher, B. R. Suydam, and D. Yevick, Opt. Lett. **8**, 611 (1983).

[5] S. Chi, S. F. Wen, Opt. Lett. **19**, 1705 (1994).

[6] C. Joubert, M. L. Roblin, and R. Grousson, Appl. Opt. **28**, 4604 (1989).

[7] D. M. Marom, D. Panasenko, P. Sun, Y. T. Mazurenko, and Y. Fainman, IEEE J. Sel. Top. Quantum Electron. **7**, 683 (2001).

[8] N. W. Carlson, L. J. Rothberg, A. G. Yodh, W. R. Babbitt, and T. W. Mossberg, Opt. Lett. **8**, 483 (1983).

[9] V. L. da Silva, Y. Silberberg, J. P. Heritage, E. W. Chase, M. A. Saifi, and M. J. Andrejco, Opt. Lett. **16**, 1340 (1991).

[10] A. Rebane, J. Aaviksoo, and J. Kuhl, Appl. Phys. Lett. **54**, 93 (1989).

[11] S. Fraigne, J. P. Galaup, J. L. Le Gouet, B. Bousquet, L. Canioni, M. Joffre, and J. P. Likforman, J. Opt. Soc. Am. B **20**, 1555 (2003).

[12] A. M. Weiner, D. E. Leaird, D. H. Reitze, and Eung Gi Paek, IEEE J. Quantum Electron. **28**, 2251 (1992).

[13] D. Marom, D. Panasenko, R. Rokitski, P. Sun, and Y. Fainman, Opt. Lett. **25**, 132 (2000).

[14] M. Tsang and D. Psaltis, Opt. Express **12**, 2207 (2004).

[15] R. Normandin and G. I. Stegeman, Opt. Lett. **4**, 58 (1979).

[16] D. Vakhshoori, R. J. Fischer, M. Hong, D. L. Sivco, G. J. Zydzik, G. N. S. Chu, and A. Y. Cho, Appl. Phys. Lett. **59**, 896 (1991).

[17] Y. J. Ding, S. J. Lee, and J. B. Khurgin, Phys. Rev. Lett. **75**, 429 (1995).

[18] Y. J. Ding, J. B. Khurgin, and S. J. Lee, Opt. Quantum Electron. **28**, 1617 (1996).

[19] C. Degen, G. Jennemann, I. Fischer, W. Elsaber, S. Leu, R. Rettig, and W. Stolz, Opt. Quantum Electron. **34**, 707 (2002).

[20] S. Janz, F. Chatenoud, and R. Normandin, Opt. Lett. **19**, 622 (1994).

[21] A. Otomo, G. I. Stegeman, M. C. Flipse, M. B. J. Diemeer, W. H. G. Horsthuis, and G. R. Mohlmann, J. Opt. Soc. Am. B **15**, 759 (1998).

[22] C. Canalias, V. Pasiskevicius, R. Clemens, and F. Laurell, Appl. Phys. Lett. **82**, 4233 (2003).

[23] R. Quintero-Torres and M. Thakur, J. Appl. Phys. **85**, 401 (1999).

[24] S. Li and J. Khurgin, Appl. Phys. Lett. **62**, 1727 (1993).

Chapter 6

Spontaneous spectral phase conjugation for coincident frequency entanglement

6.1 Introduction

It has been proven in the two previous chapters that if the three-wave mixing (TWM) or four-wave mixing (FWM) parametric process is transversely pumped with short pulses in a long and thin nonlinear medium, parametric amplification can be performed, with time reversal and spectral phase conjugation (SPC) [1, 2]. The correspondence between classical parametric amplification and quantum entanglement makes one wonder if spontaneous SPC can perform the opposite of what its continuous-wave-pumped counterpart does, and realize time anticorrelation or frequency correlation. This distinct kind of entanglement is useful for applications such as quantum-enhanced position and clock synchronization [3] and one-way autocompensating quantum cryptography [4]. Various implementations of such entanglement have been suggested [5, 6], and the scheme proposed by Walton *et al.* [6] looks intriguingly similar to the TWM scheme for SPC [1]. On the other hand, while TWM is traditionally the preferred method to generate entangled photons, recent experimental progress on entangled photon sources using third-order nonlinear processes [7, 8] makes FWM a promising candidate for such a task. In this chapter, we prove that spontaneous SPC, either by TWM or FWM, can indeed efficiently generate time-anticorrelated and frequency-correlated photon pairs.

Our proposed schemes have several key improvements over that in Ref. [6], and make coincident frequency entanglement much more realizable. First, it is unclear in Ref. [6] how phase matching should be achieved. We propose the incorporation of quasi-phase matching to satisfy the requirement. Second, we suggest an alternative FWM scheme, which can be more efficient with focused femtosecond pump beams. Third, for good efficiency, cross-phase modulation due to the strong pump becomes a large parasitic effect for both schemes. We introduce the use of pump phase modulation to compensate for cross-phase modulation. We also perform an in-depth Heisenberg analysis of the spontaneous SPC schemes, predicting that a high gain is possible with current technology. The high gain enables the generation of large-photon-number frequency-correlated states, which are interesting for their use in nonlocal dispersion cancellation and noise

reduction experiments [9].

Lastly we investigate the use of frequency-correlated photons generated by our proposed schemes in the Hong-Ou-Mandel (HOM) interferometer [10], subject to temporal delays, dispersion, frequency shifts, and temporal phase modulation. Quantum dispersion cancellation in the HOM interferometer with such photons has been studied [10, 11, 12, 13], but relatively little attention is given to the distinguishability introduced by phase modulation in the time domain, for example, via the optical Kerr effect, which can be useful in quantum nondemolition measurements [14]. Ref. [11] studies the effect of frequency shifts on frequency-correlated photons, but only in a highly idealized case. Using the formalism developed for our schemes, we first review the HOM dip effect introduced by time delays and dispersion for completeness, and then study the nonlocal temporal phase cancellation properties of the entangled photons.

6.2 Configurations

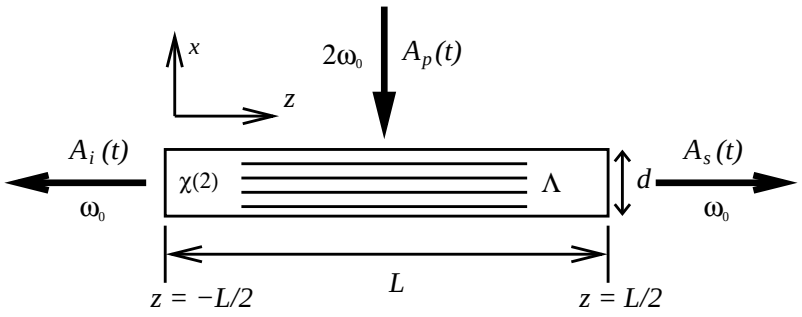

Figure 6.1: Spontaneous SPC by TWM.

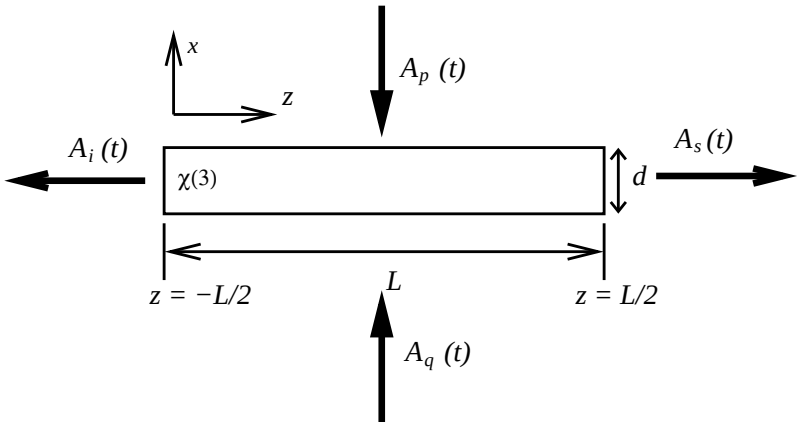

Figure 6.2: Spontaneous SPC by FWM.

The spontaneous SPC scheme by TWM is sketched in Fig. 6.1, and the FWM scheme in Fig. 6.2. For the

TWM scheme, the interaction Hamiltonian is

$$\hat{H} \propto w \int dx \int dz \chi^{(2)} f(z) E_p^{(+)} E_s^{(-)} E_i^{(-)} + H.c., \tag{6.1}$$

where w is the width of the nonlinear medium in the y dimension, $\chi^{(2)}$ is the second-order nonlinear susceptibility, $f(z)$ is the pump beam profile, $E^{(+)}$ and $E^{(-)}$ are the positive-frequency and negative-frequency electric field operators, respectively, and the subscripts p, s, i denote pump, signal and idler, respectively. If the pump is assumed to be classical, the electric field operators can be written in terms of envelopes, $E_p^{(+)} \propto A_p(t+\frac{x}{v_x})\exp(-i2\omega_0 t - ik_x x)$, $E_s^{(-)} \propto \hat{A}_s^\dagger(t-\frac{z}{v})\exp(i\omega_0 t - ik_z z)$ and $E_i^{(-)} \propto \hat{A}_i^\dagger(t+\frac{z}{v})\exp(i\omega_0 t + ik_z z)$, where k_x is the pump carrier wave vector, and v and v_x are the group velocities in z and x, respectively. Unlike the scheme in Ref. [5], spontaneous SPC places no restriction on the material dispersion properties as long as the signal and idler are the same but counterpropagating modes. Otherwise the pump beam(s) can be slightly tilted in the z direction to compensate fo the signal-idler phase mismatch. The interaction Hamiltonian then becomes

$$\hat{H} \propto w \int_{-\frac{d}{2}}^{\frac{d}{2}} dx \int dz \chi^{(2)} f(z) A_p(t+\frac{x}{v_x}) \hat{A}_s^\dagger(t-\frac{z}{v}) \hat{A}_i^\dagger(t+\frac{z}{v}) \exp\Big[-i(k_x - \frac{2\pi}{\Lambda})x\Big] + H.c., \tag{6.2}$$

where Λ is the $\chi^{(2)}$ grating period. Ref. [15] assumes that the transverse dimension d is small enough so that detuning due to k_x can be ignored. However, for a realizable setup, k_x is usually on the order of 1/(1 μm), while d is on the order of microns for a waveguide. Hence in most cases k_x should not be ignored, and quasi-phase matching, not mentioned in Ref. [6], is in fact needed. The submicron $\chi^{(2)}$ grating period required can be fabricated, for example, in a GaAs/AlGaAs heterostructure [16]. To avoid space-time coupling, the spatial pulse width of the pump, on the order of 100 μm for a femtosecond pulse, should be much larger than $d \sim$ 10 μm, so that the x dependence of A_p can be neglected. $\hat{H}$ is then given by

$$\hat{H} \propto wd \int dz \chi^{(2)} f(z) A_p(t) \hat{A}_s^\dagger(t-\frac{z}{v}) \hat{A}_i^\dagger(t+\frac{z}{v}) + H.c. \tag{6.3}$$

The FWM process, on the other hand, is automatically phase-matched due to the counterpropagating pump pulses. The interaction Hamiltonian is

$$\hat{H} \propto w \int dx \int dz \chi^{(3)} f(z) E_p^{(+)} E_q^{(+)} E_s^{(-)} E_i^{(-)} + H.c. \tag{6.4}$$

With similar assumptions as the TWM scheme, the interaction Hamiltonian is given by

$$\hat{H} \propto wd \int dz \chi^{(3)} f(z) A_p(t) A_q(t) \hat{A}_s^\dagger(t-\frac{z}{v}) \hat{A}_i^\dagger(t+\frac{z}{v}) + H.c., \tag{6.5}$$

which is almost identical to that of the TWM scheme. Hence one can analyze both schemes in a unified

framework, with the general Hamiltonian

$$\hat{H} \propto \int dz f(z) g(t) \hat{A}_s^\dagger (t - \frac{z}{v}) \hat{A}_i^\dagger (t + \frac{z}{v}) + H.c., \tag{6.6}$$

where $g(t) \propto \chi^{(2)} A_p(t)$ for the TWM scheme and $g(t) \propto \chi^{(3)} A_p(t) A_q(t)$ for the FWM scheme. To the first order, the wave function is given by [6]

$$|\psi'\rangle \propto \int dt \hat{H} |0\rangle \tag{6.7}$$

$$\propto \int dt \int dz g(t) f(z) \hat{A}_s^\dagger (t - \frac{z}{v}) \hat{A}_i^\dagger (t + \frac{z}{v}) |0\rangle \tag{6.8}$$

$$\propto \int d\omega_s \int d\omega_i \tilde{f}(\frac{\omega_s - \omega_i}{v}) \tilde{g}(\omega_s + \omega_i) \hat{a}_s^\dagger(\omega_s) \hat{a}_i^\dagger(\omega_i) |0\rangle, \tag{6.9}$$

where $\tilde{f}$, $\tilde{g}$, and $\hat{a}_{s,i}^\dagger$ are Fourier transforms of f, g, and $\hat{A}_{s,i}^\dagger$, respectively. In the time domain, if the width of $g(t)$ is much more narrow than the width of $f(z)$ divided by v, $g(t)$ can sample the integrand in Eq. (6.8), say at $t = 0$. Equivalently in the frequency domain $\tilde{f}$ can sample the integrand at $\omega_s = \omega_i$ in Eq. (6.9). The wave function becomes

$$|\psi'\rangle \propto \int dt' g(t') \int dt f(vt) \hat{A}_s^\dagger(-t) \hat{A}_i^\dagger(t) |0\rangle \tag{6.10}$$

$$\propto \int d\omega' \tilde{f}(\frac{\omega'}{v}) \int d\omega \tilde{g}(2\omega) \hat{a}_s^\dagger(\omega) \hat{a}_i^\dagger(\omega) |0\rangle. \tag{6.11}$$

The generated photon pair therefore possesses quantum time anticorrelation and frequency correlation. In summary, for optimal entanglement, the assumption

$$\frac{L}{v} >> \text{width of } g(t) >> \frac{d}{v_x} \tag{6.12}$$

should be satisfied.

6.3 Conversion efficiency

The efficiency of spontaneous SPC is best studied in the Heisenberg picture. The coupled-operator equations, assuming classical undepleted pumps, are given by

$$\Big(v\frac{\partial}{\partial z} + \frac{\partial}{\partial t}\Big)\hat{A}_s = ig(t)\hat{A}_i^\dagger + ic(t)\hat{A}_s, \tag{6.13}$$

$$\Big(-v\frac{\partial}{\partial z} + \frac{\partial}{\partial t}\Big)\hat{A}_i^\dagger = -ig^*(t)\hat{A}_s - ic(t)\hat{A}_i^\dagger, \tag{6.14}$$

where

$$g(t) = \frac{\omega_0 v \chi^{(2)}}{2cn_0} A_p(t) \tag{6.15}$$

for the TWM scheme and

$$g(t) = \frac{3\omega_0 v \chi^{(3)}}{4cn_0} A_p(t) A_q(t) \tag{6.16}$$

for the FWM scheme.

$$c(t) = \frac{3\omega_0 v \chi^{(3)}}{4cn_0} (|A_p|^2 + |A_q|^2) \tag{6.17}$$

is the cross-phase modulation term, which acts as a time-dependent detuning factor. Cross-phase modulation is always present in the FWM scheme, while it exists in the form of competing third-order nonlinearity in the TWM scheme. Eqs. (6.13) and (6.14) can be solved in the same manner as the classical SPC analysis [1, 2]. The temporary detuning due to cross-phase modulation can be compensated if $g(t)$ is also appropriately detuned. Quantitatively, the phase of $g(t)$ should be modulated as [2],

$$\theta(t) = \theta_0 + 2\int_{-\infty}^{t} dt' c(t'). \tag{6.18}$$

$\theta(t)$ can be approximated by a linear temporal phase, or a center frequency shift of $g(t)$ [2]. In other words, for spontaneous SPC under the cross-phase modulation effect, the generation of photon pairs will actually be most efficient at a center frequency different from the center pump frequency in the FWM scheme, or from half the center second-harmonic pump frequency in the TWM scheme. This is analogous to the phenomenon of sideband gain in continous-wave FWM, although now the signal and idler spectra should *coincide* with each other. This feature is actually desirable for the FWM scheme, since it is easier to separate the scattered pump from the weak signal and idler by spectral filtering.

The average number of photons in each mode is

$$n_s = C^2 n_{s0} + S^2 (n_{i0} + 1), \tag{6.19}$$

$$n_i = C^2 n_{i0} + S^2 (n_{s0} + 1), \tag{6.20}$$

where $C \equiv \cosh[\int dt |g(t)|]$, $S \equiv \sinh[\int dt |g(t)|]$, n_{s0} is the initial signal photon number, and n_{i0} is the initial idler photon number. The number of photon pairs spontaneously generated in each wave mixing event is therefore S^2, and the conversion efficiency, defined as the energy of the generated photons divided by the

energy of the pump photons, is

$$\Gamma = \frac{2S^2\hbar\omega_0}{\mathscr{E}_p}, \tag{6.21}$$

where $\mathscr{E}_p$ is the total pump energy. The FWM scheme is more efficient than the TWM scheme when $g(t)$ of the former is larger, or, all else being equal,

$$\frac{\chi^{(3)}}{(n_0^{(3)})^3}\left(\frac{\mathscr{E}_p}{\varepsilon_0 cLwT_p}\right)^{\frac{1}{2}} \gtrsim \frac{\chi^{(2)}}{(n_0^{(2)})^{\frac{5}{2}}}, \tag{6.22}$$

where T_p is the pump pulse width.

For example, polydiacetylene, a conjugate polymer, has a $\chi^{(3)} \sim 10^{-18}$ m^2/V^2 and $n_0^{(3)} \sim 2$, while a GaAs/AlGaAs heterostructure has a $\chi^{(2)} \sim 10^{10}$ m/V and $n_0^{(2)} \sim 4$. For a focused femtosecond pump beam, say $L \sim 2$ mm, $w \sim 5$ μm, $T_p \sim 100$ fs, the FWM scheme is more efficient when $\mathscr{E}_p$ is approximately larger than 1 nJ. Ti:Sapphire laser systems can achieve a pulse energy of 1 mJ or more, so the FWM scheme can be orders of magnitude more efficient. The FWM scheme also has the advantage of automatic phase matching as well as having pump pulses near the fundamental frequency, thus eliminating the need of quasi-phase matching and a second-harmonic source in an experiment. That said, the necessity of synchronizing two short pump pulses in the FWM scheme may undermine its robustness, while the TWM scheme may be more efficient for certain parameters and it is relatively easier to filter out scattered second-harmonic pump from the signal and idler. For the parameters above, the signal and idler gain S^2 can achieve 100% for a pump pulse energy ~ 10 nJ with the FWM scheme and ~ 2 μJ with the TWM scheme. For such a relatively high gain the wave function can have higher-order terms [17], $|\psi\rangle \propto \sum_{n=0}^{\infty} T^n |n\rangle_s |n\rangle_i$, where $T = S/C$, and the weights of large-photon-number states T^{2n} with $n > 1$ become appreciable when S^2 approaches unity. Amplification of coincident frequency entanglement [17] also becomes possible.

6.4 Hong-Ou-Mandel interferometry

In the HOM interferometry, variable delays are introduced to the signal and idler photons, which then pass through a 50-50 beam splitter and finally the coincidence rate of the two output ports is measured [10]. For simplicity we also assume that the distances from the two detectors to the beam splitter are the same. We start with the more general wave function in Eq. (6.8). The electric field operators of the two outputs are given by

$$\hat{A}_{1,2}(t) \propto \hat{A}_{s,i}(\pm L_{s,i}, t) + i\hat{A}_{i,s}(\mp L_{i,s}, t), \tag{6.23}$$

where $L_{s,i}$ are the distances travelled by the signal and the idler from $z=0$ to the detectors, respectively. L_i has a negative sign in front because the idler travels backwards. The coincidence rate is given by [12, 13]

$$P_c \propto \int dt_1 \int dt_2 \langle \psi' | \hat{A}_1^\dagger(t_1) \hat{A}_2^\dagger(t_2) \hat{A}_1(t_1) \hat{A}_2(t_2) | \psi' \rangle \tag{6.24}$$

$$\propto \int dt_+ |g(t_+ - \frac{L_+}{v})|^2 \Big[\int dt_- |f(L_- - vt_-)|^2 - \mathrm{Re} \int dt_- f^*(L_- - vt_-) f(L_- + vt_-) \Big]. \tag{6.25}$$

where $t_+ = (t_1+t_2)/2$, $L_+ = (L_s+L_i)/2$, $t_- = (t_1-t_2)/2$ and $L_- = (L_s-L_i)/2$ is half the signal-idler path difference. The shape of the HOM dip with respect to the path difference $L_s - L_i$ is given by the last term of Eq. (6.25), which has a width on the order of L, the width of the pump beam profile $f(z)$. Ref. [11] predicts that P_c is identically zero for all L_- with perfectly frequency-correlated photons, which is simply a special case when $L \to \infty$.

Steinberg *et al.* predicted [18] and demonstrated [19] even-order dispersion cancellation in the HOM interferometer with frequency-anticorrelated photons. With frequency-correlated photons, intuition then suggests that one can obtain nonlocal cancellation of dispersion of all orders, which is proven in Ref. [12]. To see how this effect manifests itself in our schemes, we shall start with the general wave function in the frequency domain, Eq. (6.9), and apply spectral phase to the operators just as in Ref. [18]. The coincidence rate can be expressed in terms of frequency-domain operators as [18]

$$P_c \propto \int d\omega_1 \int d\omega_2 \langle \psi' | \hat{a}_1^\dagger(\omega_1) \hat{a}_2^\dagger(\omega_2) \hat{a}_1(\omega_1) \hat{a}_2(\omega_2) | \psi' \rangle \tag{6.26}$$

$$\propto \int d\omega_1 \int d\omega_2 |\tilde{g}(\omega_1+\omega_2)|^2 \Big\{ |\tilde{f}(\frac{\omega_1-\omega_2}{v})|^2 - \mathrm{Re}\Big[\tilde{f}(\frac{\omega_1-\omega_2}{v}) \tilde{f}^*(\frac{\omega_2-\omega_1}{v}) \exp\Big(i[k_s(\omega_1)-k_s(\omega_2)]L_s - i[k_i(\omega_1)-k_i(\omega_2)]L_i \Big) \Big] \Big\}. \tag{6.27}$$

where k_s and k_i are the dispersive propagation constants of the signal and idler, respectively. The exponential term in Eq. (6.27) characterizes the nonlocal dispersion cancellation. If the photons have perfect frequency anticorrelation, $\tilde{g}$ is infinitely sharp, $\omega_1 = -\omega_2$, and we recover the even-order dispersion cancellation results in Ref. [18]. If $\tilde{f}$ is infinitely sharp, $\omega_1 = \omega_2$, the exponential term evalulates to 1 and $P_c = 0$ for dispersion of all orders. If $\tilde{f}$ is not infinitely sharp and dispersion is only due to time delay, the result in Eq. (6.25) is recovered.

Frequency shifts can be introduced to the signal and the idler by, for example, moving mirrors or acousto-optic modulators via the Doppler effect. Opposite Doppler shifts can also occur to the counterpropagating photons if the source frame is moving along z relative to the detection frame. We can then rewrite $\hat{A}_1$ and $\hat{A}_2$,

$$\hat{A}_{1,2}(t) \propto \exp(-i\delta\omega_{s,i}t)\hat{A}_{s,i} + i\exp(-i\delta\omega_{i,s}t)\hat{A}_{i,s}, \tag{6.28}$$

where $\delta\omega_s$ is the signal frequency shift and $\delta\omega_i$ is the idler frequency shift. For intuitiveness we assume that

the path delays for both photons are the same, or $L_s = L_i = L_+$. P_c becomes

$$P_c \propto \int dt_+ |g(t_+ - \frac{L_+}{v})|^2 \Big\{ \int dt_- |f(-vt_-)|^2 - \\ \mathrm{Re} \int dt_- f^*(-vt_-) f(vt_-) \exp\left[2i(\delta\omega_s - \delta\omega_i)t_-\right] \Big\}. \tag{6.29}$$

The last term of Eq. (6.29), which is the Fourier transform of $|f(vt)|^2$ if $f(vt)$ is even, characterizes the HOM dip with respect to the frequency difference $\delta\omega_s - \delta\omega_i$. The width of the dip is on the order of v/L, for which the infinitely sharp dip predicted by Ref. [11] is again a special case when $L \to \infty$.

The coincidence rate depends on the time-domain operators in Eq. (6.24) in the same way as the expression in Eq. (6.26) depends on frequency-domain operators,

$$P_c \propto \int dt_1 \int dt_2 \langle \psi' | \hat{A}_1^\dagger(t_1) \hat{A}_2^\dagger(t_2) \hat{A}_1(t_1) \hat{A}_2(t_2) | \psi' \rangle, \tag{6.30}$$

$$\propto \int d\omega_1 \int d\omega_2 \langle \psi' | \hat{a}_1^\dagger(\omega_1) \hat{a}_2^\dagger(\omega_2) \hat{a}_1(\omega_1) \hat{a}_2(\omega_2) | \psi' \rangle. \tag{6.31}$$

Hence the coincidence rate obeys a kind of Parseval's relation, and the frequency domain results can be directly applied to the time domain, if we replace frequency-domain operators with time-domain operators, frequency anticorrelation with time anticorrelation, frequency correlation with time correlation, and spectral phase modulation (dispersion) with temporal phase modulation.

One can introduce temporal phase modulation to the photons by Doppler shift as mentioned above, or by cross-phase modulation via a classical pulse in a Kerr medium if a more complex phase profile is desired. Given the Parseval's relation for coincidence, we then expect the HOM interferometry results with frequency-anticorrelated photons subject to dispersion to be functionally the same as the results with time-anticorrelated photons subject to temporal phase modulation. The coincidence rate is

$$P_c \propto \int dt |f(vt)|^2 \Big\{ 1 - \cos[\phi_s(t) - \phi_s(-t) - \phi_i(t) + \phi_i(-t)] \Big\}, \tag{6.32}$$

where $\phi_{s,i}$ are the temporal phases introduced to the signal and idler photons. The even component of temporal phase is cancelled, as expected. For a linear temporal phase, the result in Eq. (6.29) is recovered. On the other hand, time-correlated photons are capable of complete nonlocal temporal phase cancellation. An analogy with classical nonlinearity compensation by different phase conjugation schemes can clearly be made; whereas midway SPC can only compensate for the elastic component of the Kerr effect, midway temporal phase conjugation can compensate for both the instantaneous and delayed Kerr effects [20].

The Parseval's relation for coincidence of course holds for any kind of interferometer, so any result with other interoferometers obtained with frequency-anticorrelated photons subject to dispersion can be applied directly to time-anticorrelated photons subject to temporal phase modulation. For instance, the extensive study of Mach-Zehnder interferometry with frequency anticorrelated photons in Ref. [11] can be utilized just

as well in the time domain.

6.5 Conclusion

In conclusion, spontaneous SPC schemes by TWM and FWM are studied and compared under a general framework. It is proven that spontaneous SPC is capable of generating entangled photon pairs with time anticorrelation and frequency correlation. The use of quasi-phase matching and four-wave mixing is also proposed to improve the efficiency. Just as in the classical analysis, pump phase modulation is shown to effectively compensate for detuning due to cross-phase modulation.

Bibliography

[1] M. Tsang and D. Psaltis, Opt. Commun. **242**, 659 (2004).

[2] M. Tsang and D. Psaltis, Opt. Express **12**, 2207 (2004).

[3] V. Giovannetti, S. Lloyd, and L. Maccone, Nature (London) **412**, 417 (2001).

[4] Z. D. Walton, A. F. Abouraddy, A. V. Sergienko, B. E. A. Saleh, and M. C. Teich, Phys. Rev. A **67**, 062309 (2003).

[5] V. Giovannetti, L. Maccone, J. H. Shapiro, and F. N. C. Wong, Phys. Rev. Lett. **88**, 183602 (2002).

[6] Z. D. Walton, M. C. Booth, A. V. Sergienko, B. E. A. Saleh, and M. C. Teich, Phys. Rev. A **67**, 053810 (2003).

[7] M. Fiorentino, P. L. Voss, J. E. Sharping, and P. Kumar, IEEE Photon. Technol. Lett. **14**, 983 (2002).

[8] X. Li, J. Chen, P. Voss, J. Sharping, and P. Kumar, Opt. Express **12**, 3737 (2004).

[9] M. J. Fitch and J. D. Franson, Phys. Rev. A **65**, 053809 (2002).

[10] C. K. Hong, Z. Y. Ou, and L. Mandel, Phys. Rev. Lett. **59**, 2044 (1987).

[11] R. A. Campos, B. E. A. Saleh, and M. C. Teich, Phys. Rev. A **42**, 4127 (1990).

[12] R. Erdmann, D. Branning, W. Grice, and I. A. Walmsley, Phys. Rev. A **62**, 053810 (2000).

[13] V. Giovannetti, L. Maccone, J. H. Shapiro, and F. N. C. Wong, Phys. Rev. A **66**, 043813 (2002).

[14] N. Imoto, H. A. Haus, and Y. Yamamoto, Phys. Rev. A **32**, 2287 (1985).

[15] A. De Rossi and V. Berger, Phys. Rev. Lett. **88**, 043901 (2002).

[16] D. Vakhshoori, R. J. Fischer, M. Hong, D. L. Sivco, G. J. Zydzik, G. N. S. Chu, and A. Y. Cho, Appl. Phys. Lett. **59**, 896 (1991).

[17] F. De Martini, Phys. Rev. Lett. **81**, 2842 (1998).

[18] A. M. Steinberg, P. G. Kwiat, and R. Y. Chiao, Phys. Rev. A **45**, 6659 (1992).

[19] A. M. Steinberg, P. G. Kwiat, and R. Y. Chiao, Phys. Rev. Lett. **68**, 2421 (1992).

[20] M. Tsang and D. Psaltis, Opt. Lett. **28**, 1558 (2003).

Chapter 7

Spectral phase conjugation via extended phase matching

7.1 Introduction

In contrast with the more conventional optical phase conjugation schemes that perform phase conjugation with spectral inversion [1], spectral phase conjugation (SPC) is the phase conjugation of an optical signal in the frequency domain without spectral inversion. Equivalently, in the time domain, SPC is the phase conjugation and time reversal of the signal complex pulse envelope [2]. SPC is useful for all-order dispersion and nonlinearity compensation [3, 4], as well as optical signal processing [5]. Although SPC has been experimentally demonstrated using photon echo [6, 7], spectral hole burning [8, 9], temporal holography [3], spectral holography [10], and spectral three-wave mixing (TWM) [11], all the demonstrated schemes suffer from the use of cryogenic setups, nonrealtime operation, or extremely high pump energy. Pulsed TWM [12] and four-wave-mixing (FWM) [2, 13] processes in the transverse-pumping geometry have been theoretically proposed to efficiently perform SPC, but have not yet been experimentally realized. All the holographic and wave-mixing schemes also have strict requirements on the transverse beam profile of the signal, limiting their appeal for simultaneous diffraction and dispersion compensation applications.

There is a correspondence between classical SPC and quantum coincident frequency entanglement, as shown in Ref. [14] for the transversely pumped TWM [15, 12] and FWM [2, 13] processes. It is then interesting to see if other coincident frequency entanglement schemes are also capable of performing SPC, when an input signal is present. This chapter studies one of such schemes, which makes use of extended phase matching (EPM)[16] and has been experimentally demonstrated [17] in a periodically-poled potassium titanyl phosphate (PPKTP) crystal [18]. It is shown in Section 7.3, for the first time to the author's knowledge, that this EPM scheme is indeed capable of performing SPC and optical parametric amplification (OPA), more efficiently than previous proposals.

The analysis also yields a surprising result, namely that the parametric gain can be theoretically infinite even for a pump pulse with finite energy, analogous to backward wave oscillation, where counterpropagating

waves are parametrically coupled and can give rise to mirrorless optical parametric oscillation (OPO)[19, 20, 21, 22, 23, 24, 25]. The reason for the similarity is that, in the scheme presented here, even though the signal and the idler copropagate with the pump pulse in the laboratory frame, they *counterpropagate in the frame of the moving pump pulse*, because one is faster than the pump and one is slower. Hence the moving pump pulse provides both an effective cavity and parametric gain, leading to oscillation. In reality, however, the interaction among the pulses should be ultimately limited by the finite device length. It is shown in Section 7.4, with a Laplace analysis, that the parametric gain should abruptly increase above the threshold, where infinite gain is predicted by the Fourier analysis, but a finite medium length will always limit the gain to a finite value. Still, as previous proposals of TWM mirrorless OPO have never been experimentally achieved due to the requirement of a continuous-wave (CW) pump and the difficulty in phase matching counterpropagating waves, the presented analysis suggests the exciting possibility that mirrorless OPO can be realized with an ultrashort pump pulse and a practical poling period for phase matching of copropagating modes, if a long enough medium can be fabricated and parasitic effects can be controlled. By analyzing the scheme in the Heisenberg picture in Section 7.5, a high spontaneous parametric down conversion rate is also predicted, in excellent agreement with the experimental result reported in Ref. [17]. The result should be useful for many quantum information processing applications, such as quantum-enhanced synchronization [26] and multiphoton entanglement for quantum cryptography [27]. Finally, numerical results are presented in Section 7.6, which confirm the theoretical predictions.

7.2 Setup

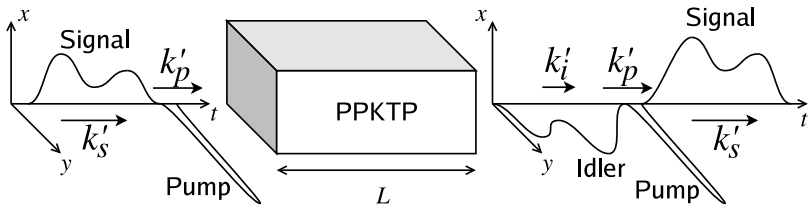

Figure 7.1: Schematic of spectral phase conjugation (SPC) via type-II extended phase matching (EPM). The signal and idler pulses, in orthogonal polarizations, have carrier frequencies of ω_s and ω_i, while the pump pulse has a carrier frequency of $\omega_p = \omega_s + \omega_i$. The EPM condition requires that the signal and the idler counterpropagate with respect to the pump, which should be much shorter than the input signal.

Consider the copropagating TWM process (Fig. 7.1), assuming that the basic type-II phase matching condition ($k_s + k_i = k_p + 2\pi/\Lambda$), with a quasi-phase-matching period Λ, is satisfied. The coupled-mode

equations are

$$\frac{\partial A_p}{\partial z} + k_p' \frac{\partial A_p}{\partial t} = j\chi_p A_s A_i, \tag{7.1}$$

$$\frac{\partial A_s}{\partial z} + k_s' \frac{\partial A_s}{\partial t} = j\chi_s A_p A_i^*, \tag{7.2}$$

$$\frac{\partial A_i^*}{\partial z} + k_i' \frac{\partial A_i^*}{\partial t} = -j\chi_i A_p^* A_s, \tag{7.3}$$

where A_p is the pump pulse envelope of carrier frequency ω_p, $A_{s,i}$ are the signal and idler envelopes of frequencies ω_s and ω_i, respectively, $k'_{p,s,i}$ are the group delays of the three modes, $\chi_{p,s,i} \equiv \omega_{p,s,i}\chi^{(2)}/(2cn_{p,s,i})$ are the nonlinear coupling coefficients, $\omega_{p,s,i}$ are the center frequencies of the modes such that $\omega_s + \omega_i = \omega_p$, and $n_{p,s,i}$ are the refractive indices. Group-velocity dispersion within each mode and diffraction are neglected. Define $\tau \equiv t - k_p' z$ as the retarded time coordinate that follows the propagating pump pulse. The change of coordinates yields

$$\frac{\partial A_p}{\partial z} = j\chi_p A_s A_i, \tag{7.4}$$

$$\frac{\partial A_s}{\partial z} + (k_s' - k_p') \frac{\partial A_s}{\partial \tau} = j\chi_s A_p A_i^*, \tag{7.5}$$

$$\frac{\partial A_i^*}{\partial z} + (k_i' - k_p') \frac{\partial A_i^*}{\partial \tau} = -j\chi_i A_p^* A_s. \tag{7.6}$$

Throughout the theoretical analysis, the pump is assumed to be undepleted and unchirped, so that $A_p = A_{p0}(t - k_p' z) = A_{p0}(\tau)$, hereafter regarded as real without loss of generality.

7.3 Fourier analysis

Equations (7.5) and (7.6) are space-invariant, if the nonlinear medium length L is much longer than the signal or idler spatial pulse width in the frame of z and τ, or

$$L >> \frac{T_{s,i}}{|k'_{s,i} - k'_p|}, \tag{7.7}$$

where $T_{s,i}$ is the signal or idler pulse width. One can then perform Fourier transform on the equations with respect to z, as defined by the following,

$$\tilde{A_s}(\kappa, \tau) \equiv \int_{-\infty}^{\infty} A_s(z, \tau) \exp(-j\kappa z) \mathrm{d}z, \tag{7.8}$$

$$\tilde{A_i^*}(\kappa, \tau) \equiv \int_{-\infty}^{\infty} A_i^*(z, \tau) \exp(-j\kappa z) \mathrm{d}z. \tag{7.9}$$

Notice that $\tilde{A}_i^*$ is defined as the Fourier transform after the conjugation of A_i. The coupled-mode equations become

$$j\kappa\tilde{A}_s + (k_s' - k_p')\frac{\partial\tilde{A}_s}{\partial\tau} = j\chi_s A_{p0}(\tau)\tilde{A}_i^*, \tag{7.10}$$

$$j\kappa\tilde{A}_i^* + (k_i' - k_p')\frac{\partial\tilde{A}_i^*}{\partial\tau} = -j\chi_i A_{p0}(\tau)\tilde{A}_s. \tag{7.11}$$

Let

$$\gamma_s \equiv k_s' - k_p',\ \gamma_i \equiv k_i' - k_p',\ r \equiv \Big|\frac{\gamma_s\chi_i}{\gamma_i\chi_s}\Big|. \tag{7.12}$$

Consider the case in which γ_s and γ_i are nonzero and have opposite signs, implying that the signal and the idler propagate in opposite directions with respect to the pump. This can be achieved for a range of wavelengths in KTP. Without loss of generality, assume that $\gamma_s > 0$ and $\gamma_i < 0$, so that $k_s' > k_p' > k_i'$. Making the following substitutions,

$$A = \sqrt{r}\tilde{A}_s\exp(j\frac{\kappa}{\gamma_s}\tau),\ B = \tilde{A}_i^*\exp(j\frac{\kappa}{\gamma_i}\tau), \tag{7.13}$$

one obtains

$$\frac{\partial A}{\partial\tau} = j\sqrt{\Big|\frac{\chi_s\chi_i}{\gamma_s\gamma_i}\Big|}A_{p0}(\tau)B\exp\Big[j\kappa(\frac{1}{\gamma_s} - \frac{1}{\gamma_i})\tau\Big], \tag{7.14}$$

$$\frac{\partial B}{\partial\tau} = j\sqrt{\Big|\frac{\chi_s\chi_i}{\gamma_s\gamma_i}\Big|}A_{p0}(\tau)A\exp\Big[-j\kappa(\frac{1}{\gamma_s} - \frac{1}{\gamma_i})\tau\Big]. \tag{7.15}$$

Due to linear space invariance, the wave-mixing process cannot generate new spatial frequencies (κ) for A and B. The magnitude of κ then depends only on the initial bandwidths of A and B, and is on the order of $2\pi\gamma_{s,i}/T_{s,i}$. As a result, if the pump pulse width T_p is much shorter than the minimum period of the detuning factor $\exp[\pm j\kappa(1/\gamma_s - 1/\gamma_i)\tau]$, or

$$T_p << \Big|\frac{2\pi}{\kappa(1/\gamma_s - 1/\gamma_i)}\Big| \sim \Big|\frac{T_{s,i}}{\gamma_{s,i}(1/\gamma_s - 1/\gamma_i)}\Big|, \tag{7.16}$$

the pump can effectively sample the detuning factor, say, at $\tau = 0$. Defining a normalized coupling function,

$$g(\tau) \equiv \sqrt{\Big|\frac{\chi_s\chi_i}{\gamma_s\gamma_i}\Big|}A_{p0}(\tau), \tag{7.17}$$

two simple coupled-mode equations are obtained,

$$\frac{\partial A}{\partial \tau} = jg(\tau)B, \tag{7.18}$$

$$\frac{\partial B}{\partial \tau} = jg(\tau)A. \tag{7.19}$$

Because the signal and the idler counterpropagate with respect to the pump, the signal should begin to mix with the pump at the leading edge of the pump pulse, say at $\tau = -T_p/2$, while the idler should begin to mix at the trailing edge of the pump, say at $\tau = T_p/2$. The solutions of Eqs. (7.18) and (7.19) can then be written as

$$A(\kappa,\tau) = \sec(G)\left\{A(\kappa,-\frac{T_p}{2})\cos\Big[\int_{T_p/2}^{\tau} g(\tau')\mathrm{d}\tau'\Big] + jB(\kappa,\frac{T_p}{2})\sin\Big[\int_{-T_p/2}^{\tau} g(\tau')\mathrm{d}\tau'\Big]\right\}, \tag{7.20}$$

$$B(\kappa,\tau) = \sec(G)\left\{jA(\kappa,-\frac{T_p}{2})\sin\Big[\int_{T_p/2}^{\tau} g(\tau')\mathrm{d}\tau'\Big] + B(\kappa,\frac{T_p}{2})\cos\Big[\int_{-T_p/2}^{\tau} g(\tau')\mathrm{d}\tau'\Big]\right\}, \tag{7.21}$$

where

$$G \equiv \int_{-T_p/2}^{T_p/2} g(\tau)d\tau \approx \int_{-\infty}^{\infty} g(\tau)\mathrm{d}\tau. \tag{7.22}$$

The input signal pulse is required to be placed in advance of the pump (by $t_s >> T_s$), and the input idler pulse to be placed behind the pump (delayed by $t_i >> T_i$), so that the signal and the idler only overlap the pump pulse inside the nonlinear medium. Consequently, the output solutions are

$$A_s(L,t) = A_{s0}(t-k_s'L+t_s)\sec(G) + j\frac{1}{\sqrt{r}}A_{i0}^*\big(-\frac{1}{r}(t-k_s'L-t_i)\big)\tan(G), \tag{7.23}$$

$$A_i(L,t) = A_{i0}(t-k_i'L-t_i)\sec(G) + j\sqrt{r}A_{s0}^*\big(-r(t-k_i'L+t_s)\big)\tan(G). \tag{7.24}$$

To see how the device is able to perform SPC, assume that the center frequencies of the two modes are the same, $\omega_s = \omega_i$, $\chi_s = \chi_i$, and the type-II EPM condition,

$$k_s' + k_i' = 2k_p',\ k_s' \neq k_i', \tag{7.25}$$

which depends on the material dispersion properties and typically occurs at a single set of center frequencies, is satisfied [16]. Then $r = 1$, and the output idler becomes the phase-conjugated and time-reversed replica of the input signal, if the input idler is zero. SPC is hence performed. The SPC efficiency η, or the idler gain, defined as the output idler fluence divided by the input signal fluence, is

$$\eta \equiv \frac{\int_{-\infty}^{\infty}|A_i(L,t)|^2\mathrm{d}t}{\int_{-\infty}^{\infty}|A_s(0,t)|^2\mathrm{d}t} = \tan^2(G). \tag{7.26}$$

This SPC efficiency can be fundamentally higher than that of the transversely pumped TWM device [12] due to two reasons. One is the copropagation of the three pulses, which makes G higher than a similar parameter in the latter case by a factor of $(1-k_p'/k_s')^{-1}$, on the order of 40 for KTP. The second reason is that for $\eta > 1$, due to the tangent function dependence, the SPC efficiency of the EPM scheme increases with respect to G much faster than that of the latter, which only depends on a similar parameter exponentially. That said, the transversely pumped FWM device [13] can still be more efficient in the small gain regime $\eta < 1$ if a highly nonlinear material, such as polydiacetylene, is used. Furthermore, the EPM device requires a longer nonlinear medium length by a factor of $(1-k_p'/k_s')^{-1}$, and depends crucially on the material dispersion, thus severely limiting the flexibility in the choice of operating wavelengths.

Equations (7.23) and (7.24) are obtained from the analysis of the coupled-mode equations (7.5) and (7.6), after Fourier transform with respect to z is performed. The solutions are therefore formally valid only when the nonlinear medium length L goes to infinity. In practice, in the moderate gain regime $\eta \sim O(1)$, the approximation given by Eq. (7.7) should be adequate, where the length L can be, say, ten times larger than the signal spatial pulse width in the frame of z and τ. Numerical analysis in Section 7.6 will validate the accuracy of the Fourier solutions.

7.4 Laplace analysis

Intriguingly, the Fourier solutions, Eqs. (7.23) and (7.24), have the same form as those of backward wave oscillation [19, 20, 21, 22, 23, 24, 25], suggesting that the device studied here, with an ultrashort pump pulse and a practical quasi-phase-matching period ($\Lambda = 46$ μm as reported in Ref. [18]), can also perform mirrorless OPO, as long as $k_{s,i}' > k_p' > k_{i,s}'$. However, the prediction of infinite gain is based on the assumption of infinite medium length and therefore may not be valid. In this case, Laplace transform should be used.

For the CW-pumped mirrorless OPO schemes, a Laplace analysis [28] with respect to time shows that beyond threshold, poles appear on the right-hand plane in the Laplace domain, meaning that the temporal impulse response increases exponentially with time, leading to self-oscillation when enough time is elapsed. The same procedures of utilizing the two-sided Laplace transform [29] as in Ref. [28] are followed here in order to be consistent with the relevant literature, but since the proposed scheme is the opposite limit of the CW devices, the Laplace transform should be performed with respect to z instead,

$$\bar{A_s}(p,\tau) \equiv \int_{-\infty}^{\infty} A_s(z,\tau)\exp(-pz)dz, \tag{7.27}$$

$$\bar{A_i^*}(p,\tau) \equiv \int_{-\infty}^{\infty} A_i^*(z,\tau)\exp(-pz)dz. \tag{7.28}$$

For simplicity but without affecting the qualitative behavior of the solutions, it is assumed that the pump pulse is square, there is no input idler, $\gamma = \gamma_s = -\gamma_i$, and $\chi = \chi_s = \chi_i$. The output solutions in the Laplace domain

are then given by

$$\bar{A_s}(p,\frac{T_p}{2}) = \frac{\sqrt{1-P^2}\csc(G\sqrt{1-P^2})}{P+\sqrt{1-P^2}\cot(G\sqrt{1-P^2})}\bar{A_s}(p,-\frac{T_p}{2}), \tag{7.29}$$

$$\bar{A_i^*}(p,-\frac{T_p}{2}) = \frac{-j}{P+\sqrt{1-P^2}\cot(G\sqrt{1-P^2})}\bar{A_s}(p,-\frac{T_p}{2}), \tag{7.30}$$

$$P \equiv \frac{p}{\chi A_{p0}},\ G \equiv \chi A_{p0}(\frac{T_p}{\gamma}). \tag{7.31}$$

If we let $p = j\kappa$, the transfer functions in Eqs. (7.29) and (7.30) are well-known to be low-pass filters [30], the bandwidth of which decreases as G increases. If the spatial bandwidth of the input signal, on the order of γ/T_s, is much smaller than the bandwidth of the low-pass filters, the transfer functions can be regarded as flat-top functions, and by plugging $P = 0$ in Eqs. (7.29) and (7.30), the Fourier solutions in Eqs. (7.23) and (7.24) are recovered. For $G << 1$, the transfer functions are sinc functions with a bandwidth $\sim \gamma/T_p$, so the Fourier solutions are valid if $T_p << T_s$, which is essentially the same assumption used in the Fourier analysis, Eq. (7.16). As G increases and the filter bandwidth decreases, however, the Fourier solutions become less and less accurate for a finite-bandwidth input signal.

The poles of the transfer functions, p_∞, can be obtained by setting the denominator of Eqs. (7.29) and (7.30) to zero,

$$p_\infty + \sqrt{(\chi A_{p0})^2 - p_\infty^2}\cot\left[G\sqrt{1-p_\infty^2/(\chi A_{p0})^2}\right] = 0. \tag{7.32}$$

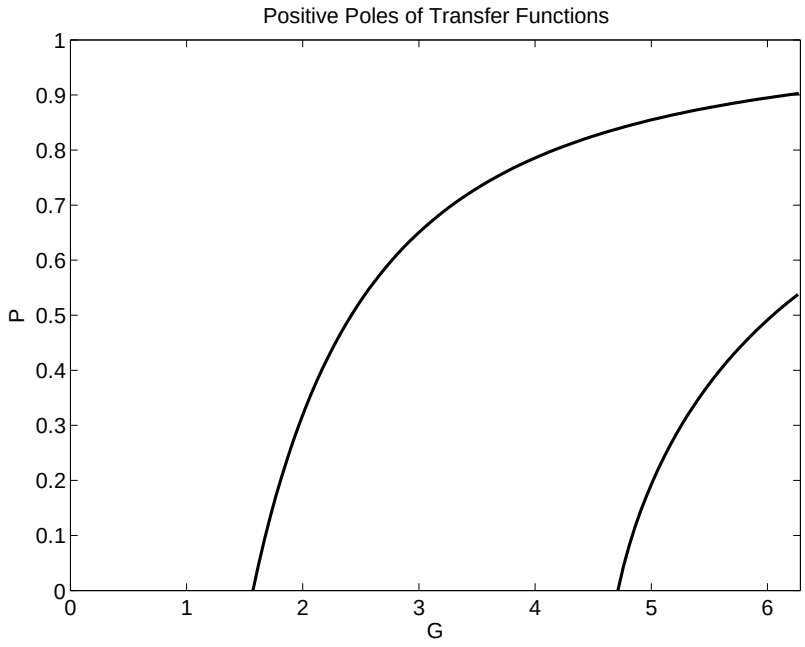

Figure 7.2: Normalized poles $p_\infty/(\chi A_{p0})$ plotted against G, obtained by numerically solving Eq. (32), indicating the onset of spatial instability beyond the threshold $G > \pi/2$. More poles appear as G is increased.

Figure 7.2 plots the normalized poles $p_\infty/(\chi A_{p0})$ against G. Positive poles begin to appear when $G > \pi/2$, hence the *spatial* impulse response increases exponentially with respect to z beyond threshold.

It is interesting to compare the scheme studied here with the case in which the pump, signal, and idler have degenerate group delays ($k_p' = k_s' = k_i'$)[31]. The coupled-mode equations of the latter case are

$$\frac{\partial A_{s,i}(z,\tau)}{\partial z} = j\chi A_{p0}(\tau) A_{i,s}^*(z,\tau), \tag{7.33}$$

where the τ derivatives vanish. The solutions are easily seen to be

$$A_{s,i}(z,\tau) = A_{s,i}(0,\tau)\cosh[\chi A_{p0}(\tau) z] + jA_{i,s}^*(0,\tau)\sinh[\chi A_{p0}(\tau) z]. \tag{7.34}$$

This corresponds to the $G \to \infty$ limit of the former scheme, where $p_\infty/(\chi A_{p0}) \to 1$ and all the poles approach the growth rate of the degenerate case, χA_{p0}.

7.5 Spontaneous parametric down conversion

Given the input-output signal-idler relationship in Eqs. (7.23) and (7.24), it is straightforward to obtain a quantum picture of the parametric process in the moderate gain regime by replacing the signal and idler envelopes with Heisenberg operators, so that

$$\hat{A}_s = \hat{A}_{s0}\sec(G) + j\hat{A}_{i0}^\dagger \tan(G), \tag{7.35}$$

$$\hat{A}_i = j\hat{A}_{s0}^\dagger \tan(G) + \hat{A}_{i0}\sec(G). \tag{7.36}$$

If the inputs are Fock states,

$$n_{s,i} \equiv \langle \hat{A}_{s,i}^\dagger \hat{A}_{s,i} \rangle = \langle \hat{A}_{s,i} \hat{A}_{s,i}^\dagger \rangle - 1, \tag{7.37}$$

$$\langle \hat{A}_{s0}^\dagger \hat{A}_{i0} \rangle = \langle \hat{A}_{i0}^\dagger \hat{A}_{s0} \rangle = \langle \hat{A}_{s0} \hat{A}_{i0}^\dagger \rangle = \langle \hat{A}_{i0} \hat{A}_{s0}^\dagger \rangle = 0. \tag{7.38}$$

The average output photon number of each mode is

$$n_s = n_{s0}\sec^2(G) + (n_{i0}+1)\tan^2(G), \tag{7.39}$$

$$n_i = n_{i0}\sec^2(G) + (n_{s0}+1)\tan^2(G). \tag{7.40}$$

The average number of spontaneously generated photon pairs per pump pulse is therefore the same as the idler gain, or $\eta = \tan^2(G)$. Moreover, the unitary transform given by Eqs. (7.35) and (7.36) has the same

form as the CW FWM process. One then expects the photon wavefunction to be similarly given by [32]

$$|\psi\rangle = \cos(G) \sum_{n=0}^{\infty} \sin^n(G)|n\rangle_s|n\rangle_i, \tag{7.41}$$

where $|n\rangle_{s,i}$ is the Fock state in the signal or idler mode. The scheme thus has a significant advantage in efficiency and robustness for multiphoton entanglement, compared with other schemes that often require feedback [33]. The efficient multiphoton coincident frequency entanglement should be useful for quantum-enhanced synchronization [26] and quantum cryptography applications [27].

The preceding quantum analysis assumes that there is only one spatial mode in each signal or idler mode, and is accurate only when the Fourier solutions are accurate. This restricts the applicability of the quantum analysis to the moderate gain regime $\eta \sim O(1)$, depending on how closely the assumption in Eq. (7.7) is observed. It is beyond the scope of this thesis to investigate what happens in the quantum picture when more than one spatial mode is involved, but qualitatively, one expects that each spatial mode should have a varying parametric gain depending on the spatial frequency, as suggested by the Laplace solutions in Eqs. (7.29) and (7.30), so the photon wavefunction would be given by a superposition of simultaneous eigenstates of spatial frequency and photon number.

Using the parameters described in Refs. [17] and [18], where $\lambda_0 = 1584$ nm, $\chi^{(2)} = 7.3$ pm/V, $n_0 = 2$, $\gamma = 1.5 \times 10^{-10}$ s/m, $T_p = 100$ fs, average pump power $= 350$ mW, diameter $= 200$ μm, and pump repetition rate $f_{rep} = 80$ MHz, the number of spontaneously generated photon pairs per second is theoretically given by $f_{rep}\tan^2(G) \approx f_{rep}G^2 = 3.6 \times 10^6$/s, in excellent agreement with the experimental result reported in Ref. [17], which is $\sim 4 \times 10^6$/s. G is then given by ~ 0.2, so the operations of SPC, OPA, and multiphoton entanglement ($G > \pi/4$) should be realizable by increasing the pump field amplitude.

7.6 Numerical analysis

Equations (7.5) and (7.6) are solved numerically via a Fourier split-step approach to confirm the above theoretical predictions. Fig. 7.3 plots the intensities and phases of the input signal, output signal, and output idler from the numerical analysis when $G = \pi/4$. The plots clearly show that the output idler is the time-reversed and phase-conjugated replica of the signal.

Figure 7.4 plots the numerical signal gain and idler gain compared with Fourier theory for $0 < G \leq \pi/3$. The numerical results are all within 3% of the theoretical values.

Figure 7.5 plots the idler gain on the logarithmic scale for a wider range of G's and two different lengths, obtained from the numerical analysis of the complete three-wave-mixing equations (7.4), (7.5), and (7.6), with a single photon as the input signal, approximately emulating parametric fluorescence. For the $L = 10$ cm case the curve can be clearly separated into three regimes; for $G < \pi/2$ and moderate gain ($\eta \sim 0$ dB), the idler gain approximately follows the Fourier solution (dashed curve). For $G > \pi/2$, the system becomes

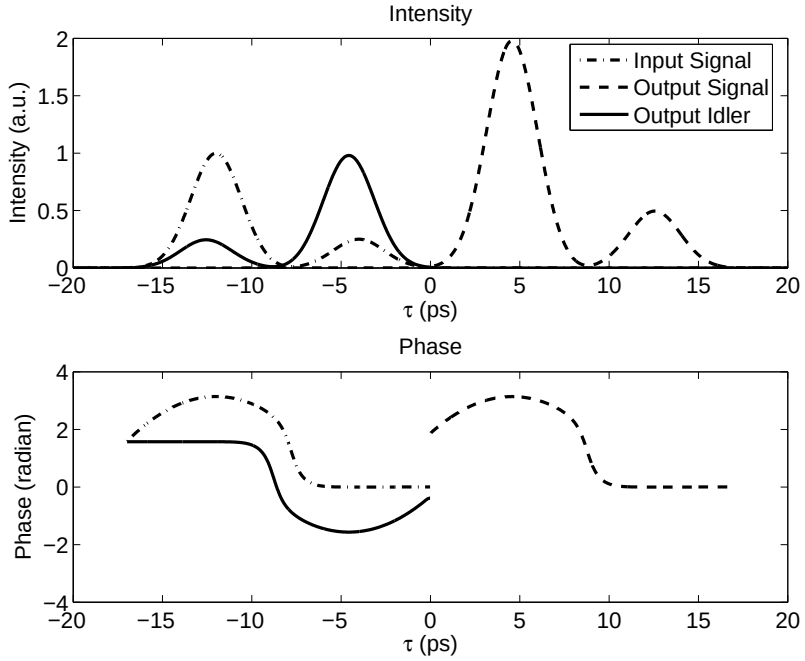

Figure 7.3: Plots of intensity and phase of input signal, output signal, and output idler, from numerical analysis of Eqs. (5) and (6). Parameters used are $k'_p = 1/(1.5\times 10^8 \mathrm{ms}^{-1})$, $k'_s = 1.025k'_p$, $k_i = 0.975k'_p$, $T_p = 100$ fs, $T_s = 2$ ps, $L = 10$ cm, $t_s = 4T_s$, beam diameter = 200 μm, $A_{s0} = 0.5\exp[-(t-2T_s)^2/(2T_s^2)] - \exp[-(1+0.5j)(t+2T_s)^2/(2T_s^2)]$, $A_{p0} = \exp[-t^2/(2T_p^2)]$, and $G = \pi/4$. The plots clearly show that the idler is the time-reversed and phase-conjugated replica, i.e., SPC, of the signal.

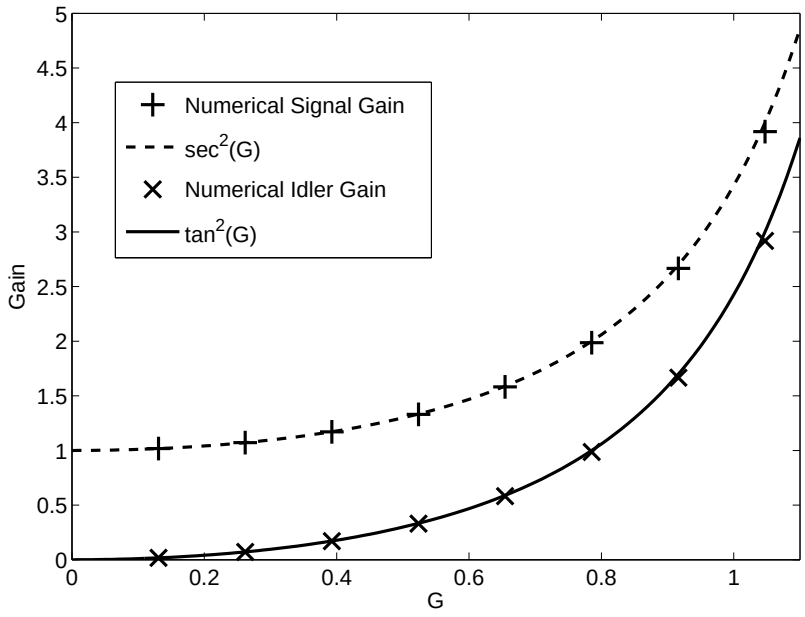

Figure 7.4: Signal gain $\eta + 1$ and idler gain η versus G from numerical analysis compared with theory. See caption of Fig. 3 for parameters used.

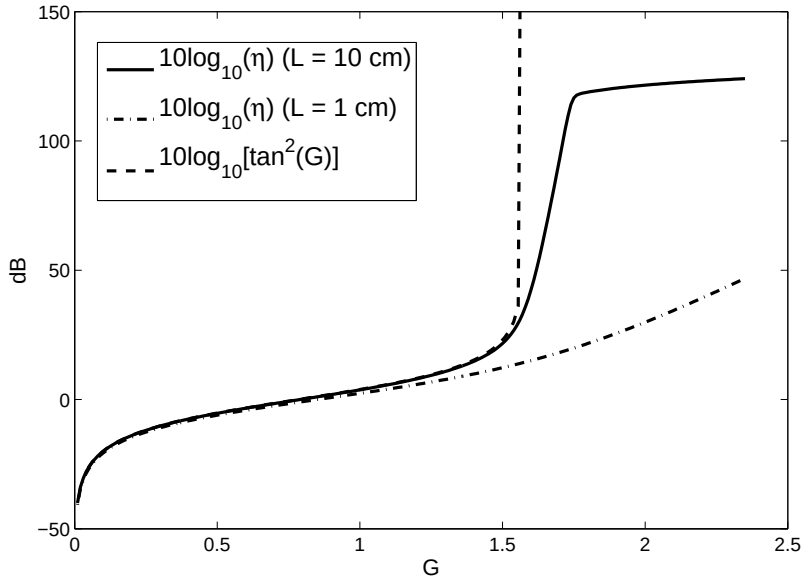

Figure 7.5: Plot of numerical idler gain η in dB against G for $L = 10$ cm (solid) and $L = 1$ cm (dash-dot), compared with the Fourier theory (dash), $\tan^2(G)$ in dB. Three distinct regimes can be observed for the $L = 10$ cm case; the moderate gain regime where the Fourier theory is accurate, the unstable regime where the gain increases exponentially, and the oscillation regime where significant pump depletion occurs. For $L = 1$ cm, the medium is not long enough for oscillation to occur in the parameter range of interest.

unstable and an exponential growth (linear ramp on the logarithmic curve) is observed, until the pump is significantly depleted, parametric oscillation occurs, and the exponential growth abruptly stops.

For $L = 1$ cm, the numerical solution departs from theory for a smaller G, and the slope of the logarithmic curve in the unstable regime, proportional to L, is too small to initiate oscillation in the parameter range of interest.

A medium length of 10 cm may be pushing the limit of current technology. Even if one is able to fabricate such a long periodically-poled nonlinear crystal, the effective medium length is always limited by parasitic effects, such as diffraction, group-velocity dispersion, and competing third-order nonlinearities, so it might be difficult to fabricate an ideal EPM device for the aforementioned purposes. For instance, in the experiment by Kuzucu *et al.* [17], the diameter of the beam is $W \sim 200$ μm, so the characteristic diffraction length is $\sim W^2/\lambda_0 = 4$ cm, while the characteristic group-velocity dispersion length is 20 cm according to Ref. [16], which are all on the order of the medium length required for mirrorless OPO. That said, techniques like diffusion bonding [34] can be used to increase the length of a nonlinear crystal, diffraction can be eliminated by waveguiding, while there exist a variety of methods to compensate for group-velocity dispersion and third-order nonlinearities [35]. Hence with careful engineering, fabricating an EPM device for the proposed applications is still a distinct possibility.

7.7 Conclusion

In summary, it is proven that the copropagating three-wave-mixing process, with appropriate extended phase matching and pumped with a short second-harmonic pulse, is capable of performing spectral phase conjugation, parametric amplification, and efficient multiphoton entanglement. The main technical challenges of experimental implementation seem to be the long medium length required and the control of parasitic effects such as diffraction, group-velocity dispersion, and competing third-order nonlinearities. However, a shorter proof-of-concept device has already been experimentally realized for the purposes of broadband second-harmonic generation [18] and coincident frequency entanglement [17], so it is not unrealistic to expect that a longer device can be fabricated for the proposed applications, which should be useful for optical communications, signal processing, and quantum information processing.

Theoretically, much remains to be explored. The study of parasitic effects, not considered in this chapter, is vital for experimental realization. The analysis of the ultrashort-pump limit can be potentially generalized to other TWM and FWM geometries, while the quantum analysis of this limit is by no means complete. In conclusion, the analysis presented here should stimulate further experimental and theoretical investigations of a new class of parametric devices.

Bibliography

[1] A. Yariv, D. Fekete, and D. M. Pepper, Opt. Lett. **4**, 52 (1979).

[2] D. A. B. Miller, Opt. Lett. **5**, 300 (1980).

[3] C. Joubert, M. L. Roblin, and R. Grousson, Appl. Opt. **28**, 4604 (1989).

[4] M. Tsang and D. Psaltis, Opt. Lett. **28**, 1558 (2003).

[5] D. M. Marom, D. Panasenko, P.-C. Sun, Y. T. Mazurenko, and Y. Fainman, IEEE J. Sel. Top. Quantum Electron. **7**, 683 (2001).

[6] N. W. Carlson, L. J. Rothberg, A. G. Yodh, W. R. Babbitt, and T. W. Mossberg, Opt. Lett. **8**, 483 (1983).

[7] V. L. da Silva, Y. Silberberg, J. P. Heritage, E. W. Chase, M. A. Saifi, and M. J. Andrejco, Opt. Lett. **16**, 1340 (1991).

[8] A. Rebane, J. Aaviksoo, and J. Kuhl, Appl. Phys. Lett. **54**, 93 (1989).

[9] S. Fraigne, J. P. Galaup, J. L. Le Gouet, B. Bousquet, L. Canioni, M. Joffre, and J. P. Likforman, J. Opt. Soc. Am. B **20**, 1555 (2003).

[10] A. M. Weiner, D. E. Leaird, D. H. Reitze, and Eung Gi Paek, IEEE J. Quantum Electron. **28**, 2251 (1992).

[11] D. M. Marom, D. Panasenko, R. Rokitski, P.-C. Sun, and Y. Fainman, Opt. Lett. **25**, 132 (2000).

[12] M. Tsang and D. Psaltis, Opt. Commun. **242**, 659 (2004).

[13] M. Tsang and D. Psaltis, Opt. Express **12**, 2207 (2004).

[14] M. Tsang and D. Psaltis, Phys. Rev. A **71**, 043806 (2005).

[15] Z. D. Walton, M. C. Booth, A. V. Sergienko, B. E. A. Saleh, and M. C. Teich, Phys. Rev. A **67**, 053810 (2003).

[16] V. Giovannetti, L. Maccone, J. H. Shapiro, and F. N. C. Wong, Phys. Rev. Lett. **88**, 183602 (2002).

[17] O. Kuzucu, M. Fiorentino, M. A. Albota, F. N. C. Wong, and F. X. Kaertner, Phys. Rev. Lett. **94**, 083601 (2005).

[18] F. Konig and F. N. C. Wong, Appl. Phys. Lett. **84**, 1644 (2004).

[19] R. Kompfner and N. T. Williams, Proc. IRE **41**, 1602 (1953).

[20] H. Heffner, Proc. IRE **42**, 930 (1954).

[21] N. M. Kroll, J. Appl. Phys. **36**, 34 (1965).

[22] D. Bobroff, J. Appl. Phys. **36**, 1760 (1965).

[23] S. E. Harris, Appl. Phys. Lett. **9**, 114 (1966).

[24] Y. J. Ding, S. J. Lee, and J. B. Khurgin, Phys. Rev. Lett. **75**, 429 (1995).

[25] A. Yariv, *Quantum Electronics* (John Wiley, New York, 1989).

[26] V. Giovannetti, S. Lloyd, and L. Maccone, Nature (London) **412**, 417 (2001).

[27] G. A. Durkin, C. Simon, and D. Bouwmeester, Phys. Rev. Lett. **88**, 187902 (2002).

[28] R. A. Fisher, B. R. Suydam, and B. J. Feldman, Phys. Rev. A **23**, 3071 (1981).

[29] B. van der Pol and H. Bremmer, *Operational Calculus Based on the Two-Sided Laplace Integral* (Cambridge University Press, Cambridge, UK, 1964).

[30] D. M. Pepper and R. L. Abrams, Opt. Lett. **3**, 212 (1978).

[31] N. E. Yu, J. H. Ro, M. Cha, S. Kurimura, and T. Taira, Opt. Lett. **27**, 1046 (2002).

[32] H.-Y. Fan and N.-Q. Jiang, Phys. Scripta **71**, 277 (2005).

[33] A. Lamas-Linares, J. C. Howell, and D. Bouwmeester, Nature (London) **412**, 887 (2001).

[34] G. Michaeli and A. Arie, Appl. Phys. B **77**, 497 (2003).

[35] G. P. Agrawal, *Nonlinear Fiber Optics* (Academic Press, San Diego, 2001).

Chapter 8

Propagation of temporal entanglement

8.1 Introduction

In quantum optics, the Heisenberg picture, where optical fields are treated as conjugate positions and momenta of quantized harmonic oscillators, is often preferred, as it is easy to substitute the optical fields in classical electromagnetic problems with noncommutative operators and obtain the Heisenberg equations of motion. Once the operator equations are solved, one can then obtain various quantum properties of the optical fields via noncommutative algebra. However, the Heisenberg picture is not without shortcomings. It can be hard to solve analytically or numerically the complex or nonlinear operator equations without approximations. It is also difficult to grasp any intuition about how the quantum correlations among the photons evolve until the Heisenberg equations are solved. These difficulties have led to a growing appreciation of the Schrödinger picture, where the photons are treated as an ensemble of bosons, and the evolution of the many-photon probability amplitude is studied. This arguably more intuitive approach has led to great success in the quantum theory of solitons [1], where instead of solving the formidable nonlinear operator equations, one can obtain analytic solutions from the *linear* boson equations in the Schrödinger picture. The many-boson interpretation has been applied to the study of entangled photons as well, where the two-photon probability amplitude is shown to obey the Wolf equations by Saleh, Teich, and Sergienko (STS) [2]. Instead of treating the entanglement properties of the photons and the optical propagation as two separate problems, with the STS equations, one can now use a single quantity, namely the two-photon amplitude, to keep track of the spatiotemporal entanglement evolution in free space. This is analogous to the Wolf equations, which reformulate the laws of optics in terms of coherence propagation [3].

In this chapter, we utilize the STS treatment of two photons to study various temporal effects, in the hope that the Schrödinger picture will offer a more accessible interpretation of temporal entanglement propagation for analytic or numerical studies of two-photon systems. Loss; group-velocity dispersion; temporal phase modulation, via an electro-optic modulator for example; linear mode coupling, via a beam splitter or a fiber coupler for example; and four-wave mixing, in a coherently prepared atomic gas [4] for example, are all included in our proposed formalism, thus extending the STS model for use in many more topics in quan-

tum optics, such as nonlocal dispersion cancellation [5, 6], fourth-order interferometry [7], and two-photon nonlinear optics [4, 8]. The analysis of a two-photon vector soliton, consisting of two photons in orthogonal polarizations under the cross-phase modulation effect, is presented in the final section, in order to demonstrate the ease of use and intuitiveness of the Schrödinger picture.

Inspired by the formalism set forth, we propose the concept of quantum temporal imaging, which uses dispersive elements and temporal phase modulators to manipulate the temporal entanglement properties of two photons. Most significantly, we show that it is possible to convert positive time correlation to negative time correlation, or vice versa, using a temporal imaging system. This conversion technique should be immensely useful for applications that require negative time correlation, such as quantum-enhanced clock synchronization [9]. Although there have been theoretical [10, 11, 12, 13] and experimental [14] proposals of generating negative time correlation directly, they have various shortcomings compared with the conventional tried-and-true schemes that generate positive time correlation. Our proposed technique should therefore allow more flexibility in choosing two-photon sources for quantum optics applications.

The chapter is structured as follows: Sec. 8.2 derives the equations that describe the evolution of the two-photon amplitude in two separate modes, Sec. 8.3 introduces the principles of quantum temporal imaging, Sec. 8.4 includes linear mode coupling in the formalism, Sec. 8.5 generalizes the formalism to two photons in more than two modes, Sec. 8.6 includes the effect of four-wave mixing, and Sec. 8.7 presents the exact solution of a two-photon vector soliton.

8.2 Two photons in two separate modes

Let us first consider two photons in two optical modes, such as two polarizations, two propagation directions, or two waveguide modes. The corresponding two-photon wavefunction is

$$|\Psi\rangle = C_{12}|1,1\rangle + C_{11}|2,0\rangle + C_{22}|0,2\rangle, \tag{8.1}$$

where the constants C_{jk}'s are the overall amplitudes of the quantum states, $|1,1\rangle$ is the quantum state in which one photon is in each mode, $|2,0\rangle$ is the state in which both photons are in mode 1, and $|0,2\rangle$ is the state which both photons are in mode 2. The positive-frequency forward-propagating component of the electric field in each mode is given by [15, 16]

$$\hat{E}_j^{(+)}(z,t) = i\int_0^\infty d\omega \left(\frac{\hbar\omega\eta_j(\omega)}{4\pi\varepsilon_0 c[n_j(\omega)]^2 S}\right)^{\frac{1}{2}} \hat{a}_j(z,\omega)\exp(-i\omega t), \tag{8.2}$$

where n_j is the complex, frequency-dependent refractive index in mode j, η_j is the real part of n_j, S is an area of quantization in the $x-y$ plane, and $\hat{a}_j$ is the photon annihilation operator, related to the corresponding

creation operator via the equal-space commutator [15, 16],

$$[\hat{a}_j(z,\omega),\hat{a}_j^{\dagger}(z,\omega')] = \delta(\omega-\omega'), \quad j=1,2. \tag{8.3}$$

In the Heisenberg picture, the creation and annihilation operators evolve according to the following equations [15, 16],

$$\frac{\partial \hat{a}_1(z,\omega)}{\partial z} = i\frac{\omega n_1(\omega)}{c}\hat{a}_1(z,\omega) + i\Big(\frac{2\omega\mu_1(\omega)}{c}\Big)^{\frac{1}{2}}\hat{f}_1(z,\omega), \tag{8.4}$$

$$\frac{\partial \hat{a}_2(z',\omega')}{\partial z'} = i\frac{\omega' n_2(\omega')}{c}\hat{a}_2(z',\omega') + i\Big(\frac{2\omega'\mu_2(\omega')}{c}\Big)^{\frac{1}{2}}\hat{f}_2(z',\omega'), \tag{8.5}$$

where μ_j is the imaginary part of n_j, and $\hat{f}_j$ is the Langevin noise operator, satisfying the commutation relation

$$[\hat{f}_j(z,\omega),\hat{f}_j^{\dagger}(z',\omega')] = \delta(z-z')\delta(\omega-\omega'). \tag{8.6}$$

To proceed, we replace $\omega n_j(\omega)/c$ by the following phenomenological approximation [17],

$$\frac{\omega n_j(\omega)}{c} \approx i\frac{\alpha_j}{2} + \sum_{n=0}^{2}\frac{\beta_{nj}}{n!}(\omega-\omega_0)^n + \frac{\omega_0}{c}\Delta n_j, \tag{8.7}$$

where $\alpha_j = 2Im[k_j(\omega_0)]$ is the loss coefficient, $\beta_{nj} = \partial^n Re[k_j(\omega)]/\partial\omega^n|_{\omega=\omega_0}$ is the nth-order dispersion coefficient, and Δn_j encompasses any other refractive index perturbation. Defining the slowly varying envelope operators as

$$\hat{A}_j(z,t) = \exp(-i\beta_{0j}z + i\omega_0 t)\int_0^{\infty}\frac{d\omega}{\sqrt{2\pi}}\,\hat{a}_j(z,\omega)\exp(-i\omega t), \tag{8.8}$$

where ω_0 is the carrier frequency of the two modes, one can obtain two evolution equations for the envelope operators,

$$\frac{\partial}{\partial z}\hat{A}_1(z,t) = iK_1\Big(t, i\frac{\partial}{\partial t}\Big)\hat{A}_1(z,t) + \hat{F}_1, \tag{8.9}$$

$$\frac{\partial}{\partial z'}\hat{A}_2(z',t') = iK_2\Big(t', i\frac{\partial}{\partial t'}\Big)\hat{A}_2(z',t') + \hat{F}_2, \tag{8.10}$$

$$K_j\Big(t, i\frac{\partial}{\partial t}\Big) = \Big[\frac{i\alpha_j}{2} + i\beta_{1j}\frac{\partial}{\partial t} - \frac{\beta_{2j}}{2}\frac{\partial^2}{\partial t^2} + \frac{\omega_0}{c}\Delta n_j(t)\Big], \tag{8.11}$$

where $\hat{F}_j$ is defined as

$$\hat{F}_j(z,t) = \exp(-i\beta_{0j}z + i\omega_0 t)\int_0^{\infty}\frac{d\omega}{\sqrt{2\pi}}\,i\Big(\frac{2\omega\mu_j(\omega)}{c}\Big)^{\frac{1}{2}}\hat{f}_j(z,\omega)\exp(-i\omega t), \tag{8.12}$$

and K_j is the complex wavenumber for the slowly varying envelope. Δn_j can explicitly depend on time, if the perturbation is much slower than the optical-frequency oscillation so that an adiabatic approximation can be made, such as in an electro-optic modulator.

We now define the two-photon probability amplitudes as

$$\psi_{12}(z,t,z',t') = \langle 0|\hat{A}_1(z,t)\hat{A}_2(z',t')|\Psi\rangle, \tag{8.13}$$

$$\psi_{11}(z,t,z',t') = \frac{1}{\sqrt{2}}\langle 0|\hat{A}_1(z,t)\hat{A}_1(z',t')|\Psi\rangle, \tag{8.14}$$

$$\psi_{22}(z,t,z',t') = \frac{1}{\sqrt{2}}\langle 0|\hat{A}_2(z,t)\hat{A}_2(z',t')|\Psi\rangle. \tag{8.15}$$

The physical significance of each amplitude ψ_{jk} is that its magnitude squared gives the probability density, P_{jk}, of coincidentally measuring one photon in mode j at (z,t) and another photon in mode k at (z',t'),

$$P_{jk}(z,t,z',t') = |\psi_{jk}(z,t,z',t')|^2. \tag{8.16}$$

Temporal entanglement is defined as the irreducibility of $|\psi_{12}|^2$ into a product of one-photon amplitudes in the form of $a(t)b(t')$. This means that the probability of detecting a photon in mode 1 at time t is correlated to the probability of detecting a photon in mode 2 at t'. The most popular ways of generating entangled photons are spontaneous parametric down conversion [18] and four-wave mixing [19], where the wave mixing geometry and the spatiotemporal profile of the pump beam determine the initial ψ_{12}.

To obtain the evolution equations for the two-photon amplitude $\psi_{12}(z,t,z',t')$ in the Schrödinger picture, we employ the same trick as in Ref. [2]. First we multiply Eq. (8.9) with $\hat{A}_2(z',t')$ and Eq. (8.10) with $\hat{A}_1(z,t)$ to produce two equations,

$$\frac{\partial}{\partial z}\hat{A}_1(z,t)\hat{A}_2(z',t') = iK_1\left(t, i\frac{\partial}{\partial t}\right)\hat{A}_1(z,t)\hat{A}_2(z',t') + \hat{F}_1\hat{A}_2, \tag{8.17}$$

$$\frac{\partial}{\partial z'}\hat{A}_1(z,t)\hat{A}_2(z',t') = iK_2\left(t', i\frac{\partial}{\partial t'}\right)\hat{A}_1(z,t)\hat{A}_2(z',t') + \hat{F}_2\hat{A}_1. \tag{8.18}$$

Using the definition of ψ_{12} in Eq. (8.13) and assuming that the thermal reservoirs are in the vacuum state so that the Langevin operators evaluate to zero when applied to the wavefunction [20], a pair of equations in terms of ψ_{12} are derived,

$$\frac{\partial}{\partial z}\psi_{12}(z,t,z',t') = iK_1\left(t, i\frac{\partial}{\partial t}\right)\psi_{12}(z,t,z',t'), \tag{8.19}$$

$$\frac{\partial}{\partial z'}\psi_{12}(z,t,z',t') = iK_2\left(t', i\frac{\partial}{\partial t'}\right)\psi_{12}(z,t,z',t'). \tag{8.20}$$

Equations (8.19) and (8.20) are the temporal version of the STS equations [2], including the effects of loss,

dispersion and phase modulation. They can also be written in the frequency domain as

$$\phi_{12}(z,\Omega,z',\Omega') = \int_{-\infty}^{\infty} dt \int_{-\infty}^{\infty} dt' \; \psi_{12}(z,t,z',t') \times \exp(i\Omega t + i\Omega' t'), \tag{8.21}$$

$$\frac{\partial}{\partial z}\phi_{12}(z,\Omega,z',\Omega') = iK_1\Big(\frac{1}{i}\frac{\partial}{\partial \Omega},\Omega\Big)\phi_{12}(z,\Omega,z',\Omega'), \tag{8.22}$$

$$\frac{\partial}{\partial z'}\phi_{12}(z,\Omega,z',\Omega') = iK_2\Big(\frac{1}{i}\frac{\partial}{\partial \Omega'},\Omega'\Big)\phi_{12}(z,\Omega,z',\Omega'). \tag{8.23}$$

For entangled photons, because ψ_{12} or ϕ_{12} cannot be separated into a product of one-photon amplitudes, distortions experienced in one arm can coherently add to the distortions experienced in the other arm, leading to various nonlocal quantum effects.

For example, considering group-velocity dispersion only, the output ϕ_{12} is given by

$$\phi_{12}(z,\Omega,z',\Omega') = \exp\Big(i\beta_{11}\Omega z + i\beta_{12}\Omega' z' + \frac{i\beta_{21}}{2}\Omega^2 z + \frac{i\beta_{22}}{2}\Omega'^2 z'\Big)\phi_{12}(0,\Omega,0,\Omega'). \tag{8.24}$$

If the photons are initially entangled with negative frequency correlation, $\phi_{12}(0,\Omega,0,\Omega')$ can be approximated by $\phi(\Omega)\delta(\Omega+\Omega')$. Ignoring the unimportant linear spectral phase, the output is

$$\phi_{12}(z,\Omega,z',\Omega') = \exp\Big[\frac{i\Omega^2}{2}(\beta_{21}z + \beta_{22}z')\Big]\phi(\Omega)\delta(\Omega+\Omega'). \tag{8.25}$$

Hence if $\beta_{21}z = -\beta_{22}z'$, the dispersion effects in both arms can nonlocally cancel each other, as originally discovered by Franson [5].

8.3 Quantum temporal imaging

In the Schrödinger picture, the two-photon amplitude evolves under temporal effects. Since the entanglement properties of the photons are contained in the two-photon amplitude, the Schrödinger picture allows one to use the temporal effects to engineer the entanglement.

First, consider the evolution of the two-photon amplitude when one of the modes, say mode 1, is subject to group-velocity dispersion,

$$\frac{\partial \psi_{12}}{\partial z} = -\beta_{11}\frac{\partial \psi_{12}}{\partial t} - \frac{i\beta_{21}}{2}\frac{\partial^2 \psi_{12}}{\partial t^2}, \tag{8.26}$$

$$\psi_{12}(L,t,z',t') = \int_{-\infty}^{\infty} d\tau \; b_1(t-\tau)\psi_{12}(0,\tau,z',t'), \tag{8.27}$$

$$b_1(t-\tau) = \Big(\frac{i}{2\pi\beta_{21}L}\Big)^{\frac{1}{2}} \exp\Big[\frac{-i(t-\beta_{11}L-\tau)^2}{2\beta_{21}L}\Big]. \tag{8.28}$$

Group-velocity dispersion is well known to be analogous to Fresnel diffraction.

Next, consider a quadratic temporal modulation of refractive index imposed on mode 1 by a short or traveling-wave electro-optic modulator,

$$\frac{\partial \psi_{12}}{\partial z} = \frac{ik_0 \Delta n_2 (t-t_0)^2}{2} \psi_{12}, \tag{8.29}$$

$$\psi_{12}(l,t,z',t') = q(t)\psi_{12}(0,t,z',t'), \tag{8.30}$$

$$q(t) = \exp\Big[\frac{ik_0 \Delta n_2 l}{2}(t-t_0)^2\Big]. \tag{8.31}$$

Quadratic temporal phase modulation is analogous to a lens. Δn_2 is assumed to be a constant, and t_0 is the time delay of the modulation. Kerr effect by a copropagating classical pulse would also suffice.

Two dispersive elements with a quadratic phase modulator inbetween form a temporal imaging system, which has been well studied in the classical domain [21]. Suppose that the photon in mode 1 propagates through the first dispersive element, with an effective dispersion coefficient β_{21} and effective length L, then passes through a time lens with refractive index modulation $\Delta n_2 (t-t_0)^2/2$, and finally propagates through the second dispersive element, with an effective dispersion coefficient β'_{21} and effective length L'. The output two-photon amplitude can be expressed in terms of the input as

$$\psi_{12}(z,t,z',t') = \int_{-\infty}^{\infty} d\tau \int_{-\infty}^{\infty} d\tau'\; b'_1(t-\tau')q(\tau')b_1(\tau'-\tau)\psi_{12}(0,\tau,z',t'), \tag{8.32}$$

$$b'_1(t-\tau') = \Big(\frac{i}{2\pi\beta'_{21}L'}\Big)^{\frac{1}{2}} \exp\Big[\frac{-i(t-\beta'_{11}L'-\tau')^2}{2\beta'_{21}L'}\Big]. \tag{8.33}$$

When the "lens law" for the time domain is satisfied,

$$\frac{1}{\beta_{21}L} + \frac{1}{\beta'_{21}L'} = k_0 \Delta n_2 l, \tag{8.34}$$

the impulse response of the system becomes

$$h(t,\tau) = \int_{-\infty}^{\infty} d\tau'\; b'_1(t-\tau')q(\tau')b_1(\tau'-\tau) \tag{8.35}$$

$$\begin{aligned} &= \frac{i}{2\pi\sqrt{\beta_{21}L\beta'_{21}L'}} \exp\Big[\frac{-i(t-\beta'_{11}L')^2}{2\beta'_{21}L'}\Big]\times \\ &\quad \exp\Big[\frac{-i(\tau+\beta_{11}L)^2}{2\beta_{21}L}\Big] \int_{-\infty}^{\infty} d\tau'\; P(\frac{\tau'}{T_a})\times \\ &\quad \exp\Big[i\Big(\frac{t-\beta'_{11}L'}{\beta'_{21}L'} + \frac{\tau+\beta_{11}L}{\beta_{21}L} - k_0\Delta n_2 l t_0\Big)\tau'\Big], \end{aligned} \tag{8.36}$$

where $P(\tau'/T_a)$ is the normalized temporal aperture function of the time lens that can be used to describe any deviation of the actual temporal phase modulation from the ideal quadratic profile, such as truncation or

higher-order phase modulation, and T_a is the aperture width. If

$$T_a >> \frac{\beta_2 L}{T_0}, \tag{8.37}$$

where T_0 is the smallest feature size of ψ_{12} along the t axis, the integral in Eq. (8.36) can be approximated by a delta function. We then arrive at the input-output relation for the two-photon amplitude,

$$\psi_{12}(z,t,z',t') = \frac{1}{\sqrt{M}}\psi_{12}(0,\frac{t-t_d}{M},z',t'), \tag{8.38}$$

$$t_d = \beta'_{11}L' + M\beta_{11}L + (1-M)t_0, \tag{8.39}$$

$$M = -\frac{\beta'_{21}L'}{\beta_{21}L}, \tag{8.40}$$

where an unimportant quadratic phase factor is omitted, t_d is the time delay of the system, and M is the magnification, which can be positive or negative depending on the signs of β_2 and β'_2.

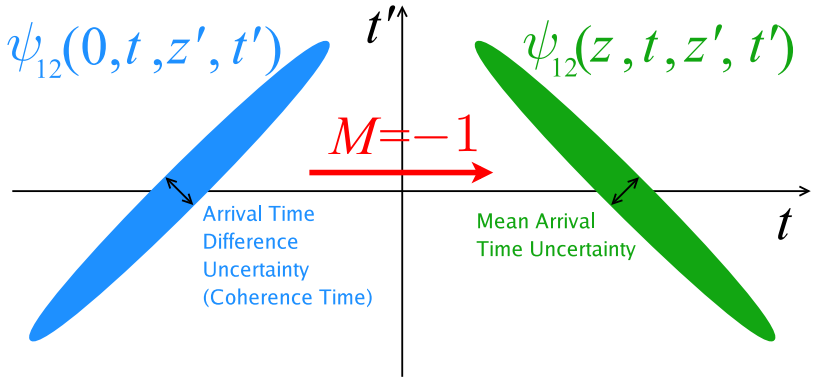

Figure 8.1: Two-dimensional sketches of the two-photon probability amplitude before and after one of the photons is time-reversed. Uncertainty in arrival time difference is transformed to uncertainty in mean arrival time.

The most interesting case is when $M = -1$, and one of the photons is time-reversed. If the two photons are initially entangled with positive time correlation, ψ_{12} can be written as

$$\psi_{12}(0,t,z',t') = a(t)b(t-t'), \tag{8.41}$$

where b is assumed to be much sharper than a. After photon 1 has passed through the temporal imaging system with $M = -1$,

$$\psi_{12}(z,t,z',t') = a(t_d - t)b(t_d - t - t'). \tag{8.42}$$

The photons hence become anticorrelated in time. See Fig. 8.1 for an illustration of this process. Since most conventional two-photon sources generate positive time correlation, but negative time correlation is

desirable for many applications, one can use the temporal imaging system to convert the former to the latter. In particular, using the aforementioned technique for the specific application of clock synchronization, the subclassical uncertainty of arrival time difference, $(t-t')/2$, can be converted to a subclassical uncertainty of mean arrival time, $(t+t')/2$, leading to a quantum enhancement of clock synchronization accuracy by a factor of $\sqrt{2}$ over the classical limit. In practice, the clock can be synchronized with the electro-optic modulator, so that the mean arrival time is controlled by t_0 and thus the clock. The proposed setup is drawn in Fig. 8.2.

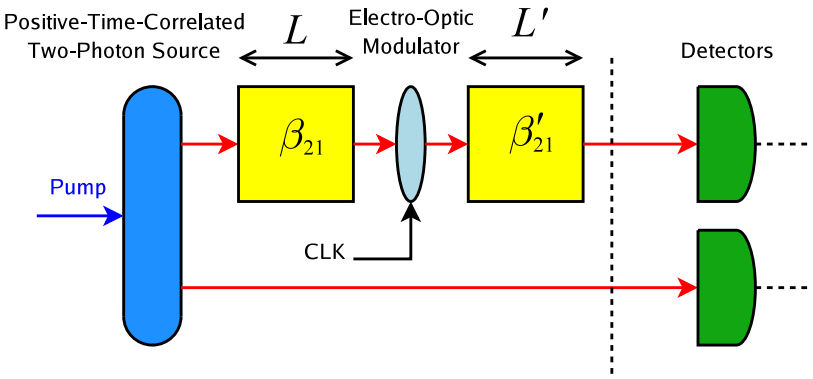

Figure 8.2: A quantum temporal imaging system for quantum-enhanced clock synchronization.

The fidelity of time reversal is limited by parasitic effects, such as higher-order dispersion and phase modulation, and the temporal aperture T_a, which adds a factor $\sim \beta'_{21}L'/T_a$ to the width of ψ along the t axis and increases the overall uncertainty of the mean arrival time. The ultimate limit, apart from instrumental ones, is set by the failure of the slowly varying envelope approximation, which only concerns ultrashort pulses with few optical cycles.

Besides the above application, one can also convert negative time correlation, which can be generated by ultrashort pulses for improved efficiency [11, 13, 22], to positive time correlation. As evident from Eq. (8.38), any desired correlation can actually be imposed on already entangled photons, by multiplying the original correlation with a factor of $1/M$.

As group-velocity dispersion and temporal phase modulation play analogous roles in the time domain to diffraction and lenses, one can use Fourier optics [23], temporal imaging [21], and quantum imaging [24] techniques to design more complex quantum temporal imaging systems.

8.4 Two photons in two linearly coupled modes

Suppose that the two modes are now coupled to each other, via, for example, a beam splitter or a fiber coupler. Equations (8.9) and (8.10) become coupled-mode equations,

$$\Big(\frac{\partial}{\partial z} - iK_1\Big)\hat{A}_1 = i\kappa(z)\hat{A}_2 + \hat{F}_1, \tag{8.43}$$

$$\Big(\frac{\partial}{\partial z'} - iK_2'\Big)\hat{A}_2' = i\kappa^*(z')\hat{A}_1' + \hat{F}_2', \tag{8.44}$$

where κ is the coupling coefficient, and for simplicity the coupling is assumed to be codirectional. The primes denote the evaluations of the functions at (z',t'). Any phase mismatch can be incorporated into κ as a z-dependent phase.

Procedures similar to those in Sec. 8.2 produce four coupled equations for ψ_{11}, ψ_{22}, and ψ_{12},

$$\Big(\frac{\partial}{\partial z} - iK_1\Big)\sqrt{2}\psi_{11}(z,t,z',t') = i\kappa\psi_{12}(z',t',z,t), \tag{8.45}$$

$$\Big(\frac{\partial}{\partial z'} - iK_2'\Big)\sqrt{2}\psi_{22}(z,t,z',t') = i\kappa^{*\prime}\psi_{12}(z',t',z,t), \tag{8.46}$$

$$\Big(\frac{\partial}{\partial z} - iK_1\Big)\psi_{12}(z,t,z',t') = i\kappa\sqrt{2}\psi_{22}(z,t,z',t'), \tag{8.47}$$

$$\Big(\frac{\partial}{\partial z'} - iK_2'\Big)\psi_{12}(z,t,z',t') = i\kappa^{*\prime}\sqrt{2}\psi_{11}(z,t,z',t'). \tag{8.48}$$

Any pair of Eqs. (8.46) and (8.47) or Eqs. (8.45) and (8.48) can be combined to yield a single equation for ψ_{12},

$$\Big(\frac{\partial}{\partial z} - iK_1\Big)\Big(\frac{\partial}{\partial z'} - iK_2'\Big)\psi_{12}(z,t,z',t') = -\kappa(z)\kappa^*(z')\psi_{12}(z',t',z,t). \tag{8.49}$$

Equation (8.49) allows one to calculate the coupled-mode propagation of two photons in terms of ψ_{12} only, given the initial conditions of ψ_{12}, ψ_{11}, and ψ_{22}. ψ_{11} and ψ_{22} can then be obtained from Eqs. (8.47) and (8.48) after ψ_{12} is calculated.

To obtain some insight into Eq. (8.49), consider only constant mode coupling, so that Eq. (8.49) becomes

$$\frac{\partial}{\partial z}\frac{\partial}{\partial z'}\psi_{12}(z,t,z',t') = -\kappa^2\psi_{12}(z',t',z,t). \tag{8.50}$$

The solution is

$$\begin{aligned}\psi_{12}(z,t,z',t') = {} & \cos(\kappa z)\cos(\kappa z')\psi_{12}(0,t,0,t') - \sin(\kappa z)\sin(\kappa z')\psi_{12}(0,t',0,t) + \\ & i\sin(\kappa z)\cos(\kappa z')\sqrt{2}\psi_{22}(0,t,0,t') + i\cos(\kappa z)\sin(\kappa z')\sqrt{2}\psi_{11}(0,t,0,t').\end{aligned} \tag{8.51}$$

At the coupler output, $z = z' = L$,

$$\psi_{12}(L,t,L,t') = T\psi_{12}(0,t,0,t') - R\psi_{12}(0,t',0,t) + i\sqrt{2TR}\psi_{22}(0,t,0,t') + i\sqrt{2TR}\psi_{11}(0,t,0,t'). \quad (8.52)$$

where $T = \cos^2(\kappa L)$ and $R = 1 - T = \sin^2(\kappa L)$. If we have one photon in each mode initially, only the initial condition of ψ_{12} is nonzero, and

$$\psi_{12}(L,t,L,t') = T\psi_{12}(0,t,0,t') - R\psi_{12}(0,t',0,t). \quad (8.53)$$

From Eq. (8.53), one can see that the output amplitude is the destructive interference between the original amplitude and its replica but with the two photons exchanging their positions in time. In particular, for a 50%-50% coupler, $T = R = 1/2$, complete destructive interference is produced if the two input photons are temporally indistinguishable. See Fig. 8.3 for a graphical illustration of the destruction interference. The introduction of variable distinguishability to photons, in order to produce varying degrees of destructive interference of ψ_{12} via a beam splitter and to measure the two-photon coherence time, is the basic principle of the Hong-Ou-Mandel interferometer [7].

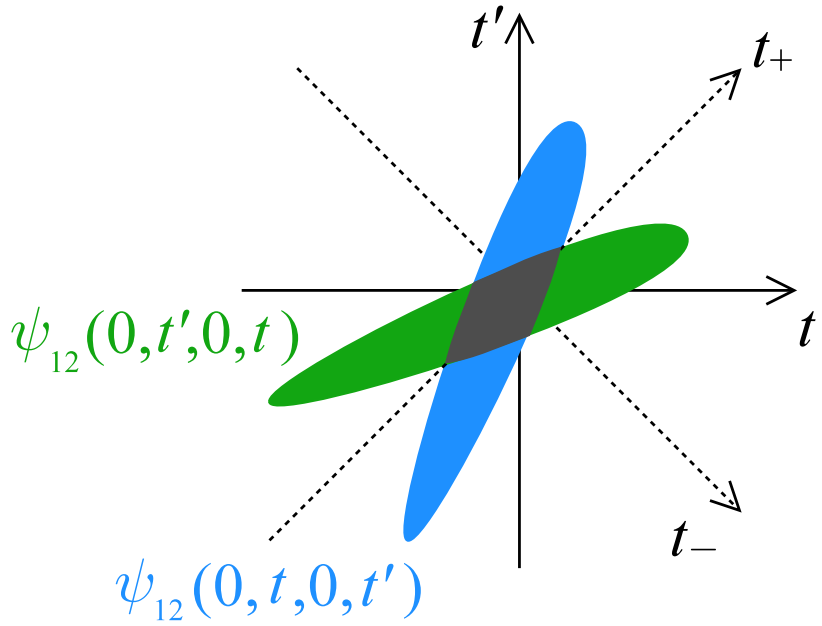

Figure 8.3: The quantum destructive interference via a coupler is determined by the overlap (dark grey area) of the two-photon amplitude $\psi_{12}(0,t,0,t')$ with its mirror image with respect to the $t+t'$ axis, $\psi_{12}(0,t',0,t)$.

8.5 Two photons in many modes

If the two photons are optically coupled to more than two modes, such as four modes for two polarizations in each of the two propagation directions, or N modes in an array of N fibers coupled to each other, one in general needs $N(N+1)/2$ two-photon amplitudes to describe the system. The propagation of the amplitudes in many modes is described by the following,

$$\left(\frac{\partial}{\partial z} - iK_j\right)\sqrt{1+\delta_{jk}}\psi_{jk}(z,t,z',t') = i\sum_{l\neq j}\kappa_{jl}\sqrt{1+\delta_{lk}}\psi_{lk}(z,t,z',t'), \tag{8.54}$$

where

$$\psi_{jk}(z,t,z',t') = \psi_{kj}(z',t',z,t), \quad \kappa_{jk} = \kappa_{kj}^*. \tag{8.55}$$

Further simplications can also be made if any of the coupling terms is zero.

For example, let there be four modes; mode 1 corresponds to arm 1 with x polarization, mode 2 corresponds to arm 2 with x polarization, mode 3 corresponds to arm 1 with y polarization, and mode 4 corresponds to arm 2 with y polarization. If only the same polarizations are coupled, the two-photon equations are

$$\begin{pmatrix} \frac{\partial}{\partial z} & -i\kappa_x & 0 & 0 \\ -i\kappa_x & \frac{\partial}{\partial z} & 0 & 0 \\ 0 & 0 & \frac{\partial}{\partial z} & -i\kappa_y \\ 0 & 0 & -i\kappa_y & \frac{\partial}{\partial z} \end{pmatrix} \begin{pmatrix} \sqrt{2}\psi_{11} & \psi_{12} & \psi_{13} & \psi_{14} \\ \psi_{21} & \sqrt{2}\psi_{22} & \psi_{23} & \psi_{24} \\ \psi_{31} & \psi_{32} & \sqrt{2}\psi_{33} & \psi_{34} \\ \psi_{41} & \psi_{42} & \psi_{43} & \sqrt{2}\psi_{44} \end{pmatrix} = 0. \tag{8.56}$$

The following solution for the orthogonally polarized amplitudes can be obtained:

$$\begin{pmatrix} \psi_{13}(L,t,L,t') \\ \psi_{24}(L,t,L,t') \\ \psi_{14}(L,t,L,t') \\ \psi_{23}(L,t,L,t') \end{pmatrix} = \begin{pmatrix} \sqrt{T_xT_y} & -\sqrt{R_xR_y} & i\sqrt{T_xR_y} & i\sqrt{T_yR_x} \\ -\sqrt{R_xR_y} & \sqrt{T_xT_y} & i\sqrt{T_yR_x} & i\sqrt{T_xR_y} \\ i\sqrt{T_xR_y} & i\sqrt{T_yR_x} & \sqrt{T_xT_y} & -\sqrt{R_xR_y} \\ i\sqrt{T_yR_x} & i\sqrt{T_xR_y} & -\sqrt{R_xR_y} & \sqrt{T_xT_y} \end{pmatrix} \begin{pmatrix} \psi_{13}(0,t,0,t') \\ \psi_{24}(0,t,0,t') \\ \psi_{14}(0,t,0,t') \\ \psi_{23}(0,t,0,t') \end{pmatrix}, \tag{8.57}$$

where $T_{x,y} = \cos^2(\kappa_{x,y}L)$ and $R_{x,y} = 1 - T_{x,y}$. In particular, if only the initial condition of ψ_{14} is nonzero,

$$\psi_{13}(L,t,L,t') = i\sqrt{T_xR_y}\psi_{14}(0,t,0,t'), \tag{8.58}$$

$$\psi_{24}(L,t,L,t') = i\sqrt{T_yR_x}\psi_{14}(0,t,0,t'), \tag{8.59}$$

$$\psi_{14}(L,t,L,t') = \sqrt{T_xT_y}\psi_{14}(0,t,0,t'), \tag{8.60}$$

$$\psi_{23}(L,t,L,t') = -\sqrt{R_xR_y}\psi_{14}(0,t,0,t'). \tag{8.61}$$

The singlet state for orthogonally polarized photons is produced if $T_x = T_y = 1/2$ [25].

8.6 Four-wave mixing

As envisioned by Lukin *et al.*, the third-order nonlinear effects among two photons can become significant in a coherently prepared atomic gas [4]. The coupled-mode equations (8.43) and (8.44) then become nonlinear,

$$\Big(\frac{\partial}{\partial z} - iK_1\Big)\hat{A}_1 = i\kappa\hat{A}_2 + i\gamma\hat{A}_1^\dagger\hat{A}_1\hat{A}_1 + i\eta\hat{A}_2^\dagger\hat{A}_2\hat{A}_1 + i\chi\hat{A}_2\hat{A}_2\hat{A}_1^\dagger + \hat{F}_1, \tag{8.62}$$

$$\Big(\frac{\partial}{\partial z'} - iK_2'\Big)\hat{A}_2' = i\kappa^{*\prime}\hat{A}_1' + i\gamma\hat{A}'^\dagger_2\hat{A}_2'\hat{A}_2' + i\eta\hat{A}'^\dagger_1\hat{A}_1'\hat{A}_2' + i\chi^{*\prime}\hat{A}_1'\hat{A}_1'\hat{A}'^\dagger_2 + \hat{F}_2', \tag{8.63}$$

where γ is the self-phase modulation coefficient, η is the cross-phase modulation coefficient, and χ is the four-wave mixing coefficient. If we define equal-space two-photon amplitudes as the following,

$$\psi_{jk}(z,t,t') = \psi_{jk}(z,t,z,t'), \tag{8.64}$$

three *linear* coupled-mode equations for the two-photon amplitudes can be derived,

$$\Big(\frac{\partial}{\partial z} - iK_1 - iK_1'\Big)\sqrt{2}\psi_{11} = i\kappa\psi_{21} + i\gamma\delta(t-t')\sqrt{2}\psi_{11} + i\chi\delta(t-t')\sqrt{2}\psi_{22}, \tag{8.65}$$

$$\Big(\frac{\partial}{\partial z} - iK_2 - iK_2'\Big)\sqrt{2}\psi_{22} = i\kappa^*\psi_{21} + i\gamma\delta(t-t')\sqrt{2}\psi_{22} + i\chi^*\delta(t-t')\sqrt{2}\psi_{11}, \tag{8.66}$$

$$\Big(\frac{\partial}{\partial z} - iK_1 - iK_2'\Big)\psi_{12} = i\kappa^*\sqrt{2}\psi_{11} + i\kappa\sqrt{2}\psi_{22} + i\eta\,\delta(t-t')\psi_{12}. \tag{8.67}$$

The advantage of the Schrödinger picture is most evident here; whereas in the Heisenberg picture one needs to solve nonlinear coupled-mode operator equations such as Eqs. (8.62) and (8.63), in the Schrödinger picture, one only needs to solve linear equations such as Eqs. (8.65) to (8.67), which are similar to the configuration-space model applied to the quantum theory of solitons [1, 26].

The delta function $\delta(t-t')$ couples the two subspaces of $\psi_{12}(z,t,t')$, so entanglement can emerge from unentangled photons [4]. To see this effect, assume that we only have four-wave mixing, so that Eq. (8.67) becomes

$$\frac{\partial}{\partial z}\psi_{12}(z,t,t') = i\eta\,\delta(t-t')\psi_{12}(z,t,t'), \tag{8.68}$$

which yields

$$\psi_{12}(L,t,t') = \exp[i\eta L\delta(t-t')]\psi_{12}(0,t,t'). \tag{8.69}$$

If the nonlinearity has a finite bandwidth $\Delta\omega$, the delta function in time should be replaced by a finite-

bandwidth function, for example a sinc function,

$$\psi_{12}(L,t,t') = \exp\Big\{\frac{i\eta L}{\pi(t-t')}\sin\Big[\frac{\Delta\omega}{2}(t-t')\Big]\Big\}\psi_{12}(0,t,t'). \tag{8.70}$$

Eq. (8.70) is the exact solution of the two-photon amplitude under the cross-phase modulation effect, while Eq. (7) in Ref. [4], presumably derived in the Heisenberg picture, is only correct in the first-order. As $\psi_{12}(L,t,t')$ cannot be written as a product of one-photon amplitudes even if the two photons are initially unentangled, entanglement is generated. The physical interpretation is that the two input photons act as pump photons to the spontaneous four-wave mixing process and are annihilated to generate two new entangled photons.

Unlike temporal imaging techniques, which can only manipulate the two-photon amplitude along the horizontal axis t or the vertical axis t', cross-phase modulation allows some manipulation of the two-photon amplitude along the diagonal time-difference axis, $t-t'$. Unfortunately, cross-phase modulation by itself cannot generate any temporal correlation, as it only imposes a phase on the two-photon temporal amplitude. In order to have more control along the $t-t'$ axis, one can combine the effects of cross-phase modulation and dispersion, as shown in the following section.

8.7 Two-photon vector solitons

In this section we study a toy example, namely, a soliton formed by two photons in orthogonal polarizations exerting cross-phase modulation on each other [17]. Although similar studies of two photons in the same mode under the self-phase modulation effect have been performed in Refs. [8], cross-phase modulation offers the distinct possibility of entangling two photons in different modes.

Consider the case in which two polarizations have the same group-velocity dispersion, so that $\beta_{21}=\beta_{22}=\beta_2$, and there is one photon in each polarization. The evolution equation for $\psi_{12}(z,t,t')$ is

$$\Big(\frac{\partial}{\partial z}+\beta_{11}\frac{\partial}{\partial t}+\beta_{12}\frac{\partial}{\partial t'}\Big)\psi_{12} = \Big[-\frac{i\beta_2}{2}\Big(\frac{\partial^2}{\partial t^2}+\frac{\partial^2}{\partial t'^2}\Big)+i\eta\,\delta(t-t')\Big]\psi_{12}. \tag{8.71}$$

Defining time coordinates in a moving frame,

$$\tau = t-\bar{\beta}_1 z, \qquad \tau' = t'-\bar{\beta}_1 z, \tag{8.72}$$

$$\bar{\beta}_1 = \frac{\beta_{11}+\beta_{12}}{2}, \qquad \Delta = \frac{\beta_{11}-\beta_{12}}{2}, \tag{8.73}$$

we obtain the following equation for $\psi_{12}(z,\tau,\tau')$,

$$\Big(\frac{\partial}{\partial z}+\Delta\frac{\partial}{\partial \tau}-\Delta\frac{\partial}{\partial \tau'}\Big)\psi_{12} = \Big[-\frac{i\beta_2}{2}\Big(\frac{\partial^2}{\partial \tau^2}+\frac{\partial^2}{\partial \tau'^2}\Big)+i\eta\,\delta(\tau-\tau')\Big]\psi_{12}. \tag{8.74}$$

Equation (8.74) is a simple linear Schrödinger equation, describing a two-dimensional "wavefunction" $\psi_{12}(z,\tau,\tau')$ in a moving frame subject to a delta potential. To solve for ψ_{12} explicitly, we define new time coordinates,

$$\tau_+ = \frac{\tau+\tau'}{2}, \quad \tau_- = \frac{\tau-\tau'}{2}, \tag{8.75}$$

Eq. (8.74) then becomes

$$\Big(\frac{\partial}{\partial z}+\Delta\frac{\partial}{\partial\tau_-}\Big)\psi_{12} = \Big[-\frac{i\beta_2}{4}\Big(\frac{\partial^2}{\partial\tau_+^2}+\frac{\partial^2}{\partial\tau_-^2}\Big)+\frac{i\eta}{2}\delta(\tau_-)\Big]\psi_{12}. \tag{8.76}$$

As evident from Eq. (8.76), the cross-phase modulation effect only offers confinement of ψ_{12} along the time difference (τ_-) axis, but not the mean arrival time (τ_+) axis.

The only bound-state solution of ψ_{12} is

$$\begin{aligned}\psi_{12}(z,\tau_+,\tau_-) = \exp\Big[-i\Big(\frac{\beta_2}{4}S^2+\frac{\Delta^2}{\beta_2}\Big)z\Big]\exp\Big(-S|\tau_-|+i\frac{2\Delta}{\beta_2}\tau_-\Big)\times \\ \int_{-\infty}^{\infty}\frac{d\Omega}{2\pi}\,\phi(\Omega)\exp\Big(-i\Omega\tau_+ + \frac{i\beta_2}{4}\Omega^2 z\Big).\end{aligned} \tag{8.77}$$

The delta potential enforces S to take on the following value,

$$S = -\frac{\eta}{\beta_2}, \tag{8.78}$$

where η and β_2 must have opposite signs. The final solution of ψ_{12} in the frame of τ and τ' is therefore

$$\begin{aligned}\psi_{12}(z,\tau,\tau') = \exp\Big[-i\Big(\frac{\eta^2/4+\Delta^2}{\beta_2}\Big)z\Big]\exp\Big[-\Big|\frac{\eta}{2\beta_2}\Big||\tau-\tau'|+i\frac{\Delta}{\beta_2}(\tau-\tau')\Big]\times \\ \int_{-\infty}^{\infty}\frac{d\Omega}{2\pi}\,\phi(\Omega)\exp\Big[-i\Omega(\frac{\tau+\tau'}{2})+\frac{i\beta_2}{4}\Omega^2 z\Big].\end{aligned} \tag{8.79}$$

The two-photon coherence time of a vector soliton is fixed, but the average arrival time is still subject to dispersive spreading and becomes increasingly uncertain as the two photons propagate. See Fig. 8.4 for an illustration. Hence, a two-photon vector soliton generates temporal entanglement with positive time correlation as it propagates. Similar to the idea of soliton momentum squeezing [27], one can also adiabatically change η or β_2 along the propagation axis to control independently the two-photon coherence time.

Notice that the center frequencies of the two photons are shifted slightly, by an amount of $\pm\Delta/\beta_2$, to compensate for their group-velocity mismatch, so that they can copropagate at the average group velocity. This is commonly known as soliton trapping [17].

If the nonlinearity has a finite bandwidth, then the potential becomes a finite-bandwidth function like the one in Eq. (8.70), and multiple bound-state solutions can be obtained via conventional techniques of solving the linear Schrödinger equation.

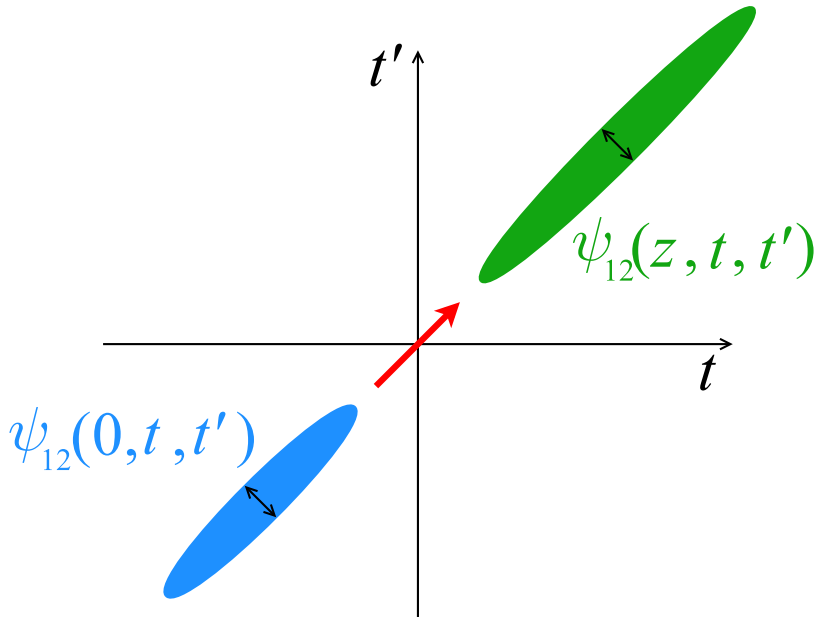

Figure 8.4: Quantum dispersive spreading of mean arrival time of a two-photon vector soliton. The cross-phase modulation effect only preserves the two-photon coherence time, giving rise to temporal entanglement with positive time correlation. One can also manipulate the coherence time independently by adiabatically changing the nonlinear coefficient along the propagation axis.

8.8 Conclusion

We have derived the general equations that govern the temporal evolution of two-photon probability amplitudes in different coupled optical modes. The formalism inspires the concept of quantum temporal imaging, which can manipulate the temporal entanglement of photons via conventional imaging techniques. The theory also offers an intuitive interpretation of two-photon entanglement evolution, as demonstrated by the exact solution of a two-photon vector soliton. To conclude, we expect the proposed formalism to be useful for many quantum signal processing and communication applications.

Bibliography

[1] Y. Lai and H. A. Haus, Phys. Rev. A **40**, 844 (1989); **40**, 854 (1989).

[2] B. E. A. Saleh, M. C. Teich, and A. V. Sergienko, Phys. Rev. Lett. **94**, 223601 (2005).

[3] E. Wolf, Nuovo Cimento **12**, 884 (1954).

[4] M. D. Lukin and A. Imamoglu, Phys. Rev. Lett. **84**, 1419 (2000).

[5] J. D. Franson, Phys. Rev. A **45**, 3126 (1992).

[6] A. M. Steinberg, P. G. Kwiat, and R. Y. Chiao, Phys. Rev. A **45**, 6659 (1992).

[7] C. K. Hong, Z. Y. Ou, and L. Mandel, Phys. Rev. Lett. **59**, 2044 (1987).

[8] R. Y. Chiao, I. H. Deutsch, and J. C. Garrison, Phys. Rev. Lett. **67**, 1399 (1991); I. H. Deutsch, R. Y. Chiao, and J. C. Garrison, Phys. Rev. Lett. **69** 3627 (1992).

[9] V. Giovannetti, S. Lloyd, and L. Maccone, Nature (London) **412**, 417 (2001).

[10] V. Giovannetti, L. Maccone, J. H. Shapiro, and F. N. C. Wong, Phys. Rev. Lett. **88**, 183602 (2002).

[11] Z. D. Walton, M. C. Booth, A. V. Sergienko, B. E. A. Saleh, and M. C. Teich, Phys. Rev. A **67**, 053810 (2003).

[12] J. P. Torres, F. Macia, S. Carrasco, and L. Torner, Opt. Lett. **30**, 314 (2005).

[13] M. Tsang and D. Psaltis, Phys. Rev. A **71**, 043806 (2005).

[14] O. Kuzucu, M. Fiorentino, M. A. Albota, F. N. C. Wong, and F. X. Kärtner, Phys. Rev. Lett. **94**, 083601 (2005).

[15] B. Huttner and S. M. Barnett, Phys. Rev. A **46**, 4306 (1992).

[16] R. Matloob, R. Loudon, S. M. Barnett, and J. Jeffers, Phys. Rev. A **52**, 4823 (1995).

[17] G. P. Agrawal, *Nonlinear Fiber Optics* (Academic Press, San Diego, 2001).

[18] M. H. Rubin, D. N. Klyshko, Y. H. Shih, and A. V. Sergienko, Phys. Rev. A **50**, 5122 (1994).

[19] M. Fiorentino, P. L. Voss, J. E. Sharping, and P. Kumar, IEEE Photon. Technol. Lett. **14**, 983 (2002).

[20] J. Jeffers and S. M. Barnett, Phys. Rev. A **47**, 3291 (1993).

[21] B. H. Kolner and M. Nazarathy, Opt. Lett. **14**, 630 (1989); B. H. Kolner, IEEE J. Quantum Electron. **30**, 1951 (1994).

[22] V. Giovannetti, L. Maccone, J. H. Shapiro, and F. N. C. Wong, Phys. Rev. A **66**, 043813 (2002).

[23] J. W. Goodman, *Introduction to Fourier Optics* (McGraw-Hill, Boston, 1996).

[24] A. F. Abouraddy, B. E. A. Saleh, A. V. Sergienko, and M. C. Teich, J. Opt. Soc. Am. B **19**, 1174 (2002).

[25] Z. Y. Ou, C. K. Hong, and L. Mandel, Opt. Commun. **63**, 118 (1987).

[26] P. L. Hagelstein, Phys. Rev. A **54**, 2426 (1996).

[27] J. M. Fini and P. L. Hagelstein, Phys. Rev. A **66**, 033818 (2002).

Chapter 9

Quantum temporal correlations and entanglement via adiabatic control of vector solitons

9.1 Introduction

If an optical pulse consists of N independent photons, then the uncertainty in the pulse center position is the pulse width divided by $\sqrt{N}$, the so-called standard quantum limit [1]. The ultimate limit permissible by quantum mechanics, however, is determined by the Heisenberg uncertainty principle and is smaller than the standard quantum limit by another factor of $\sqrt{N}$, resulting in a quantum-enhanced accuracy useful for positioning and clock synchronization applications [2]. To do better than the standard quantum limit, a multiphoton state with positive frequency correlations and, equivalently, negative time correlations is needed [2]. Consequently, significant theoretical [3, 4] and experimental [5] efforts have been made to create such a nonclassical multiphoton state. All previous efforts were based on the phenomenon of spontaneous photon pair generation in parametric processes, limiting N to 2 only. The resultant enhancement can only be regarded as a proof of concept and is too small to be useful, considering that a large number of uncorrelated photons can easily be obtained, with a standard quantum limit orders of magnitude lower than the ultimate limit achievable by two photons. It is hence much more desirable in practice to be able to enhance the position accuracy of a large number of photons. In this chapter, for the first time to the author's knowledge, a scheme that produces a multiphoton state with positive frequency correlations among an arbitrary number of photons is proposed, thus enabling quantum position accuracy enhancement for macroscopic pulses as well. The scheme set forth therefore represents a major step forward towards the use of quantum enhancement in future positioning and clock synchronization applications.

The proposed scheme exploits the quantum properties of a vector soliton, in which photons in different optical modes are bound together by the combined effects of group-velocity dispersion, self-phase modulation, and cross-phase modulation [6]. A quantum analysis shows that the mean position of the photons in

a vector soliton is insensitive to the optical nonlinearities and only subject to quantum dispersive spreading, while the separations among the photons are controlled by the balance between dispersion and nonlinearities. These properties are in fact very similar to those of scalar solitons [7, 8], so the idea of adiabatically compressing scalar solitons for momentum squeezing [9] can be similarly applied to vector solitons. The quantum dispersive spreading of the pulse center can simply be compensated by classical dispersion management, while the uncertainties in the relative frequencies among the photons can be reduced by adiabatically increasing the dispersion or decreasing the nonlinearities, resulting in a multiphoton state with a transform-limited mean-position uncertainty and positive frequency correlations. Given the past success of experiments on scalar quantum solitons [10] and vector solitons [11], the scheme set forth should be realizable with current technology. The formalism should apply to spatial vector solitons as well, so that the position accuracy of an optical beam can be enhanced [12]. Moreover, the proposed scheme is capable of creating Einstein-Podolsky-Rosen (EPR) entanglement [13] among the positions of the pulses in a vector soliton, suggesting that the vector soliton effect, together with quantum temporal imaging techniques [4], may be used for general continuous-variable quantum information processing [14].

For simplicity, only vector solitons with two optical modes, such as optical fiber solitons with two polarizations, are analytically investigated in this chapter. The results for two-mode vector solitons are representative and can be naturally extended to multimode vector solitons, such as those studied in Refs. [15].

9.2 Theory

9.2.1 Formalism

Two-mode vector solitons are classically described by the following coupled nonlinear Schrödinger equations [6],

$$i\frac{\partial U}{\partial t} = -b\frac{\partial^2 U}{\partial z^2} + 2c(|U|^2 + B|V|^2)U, \tag{9.1}$$

$$i\frac{\partial V}{\partial t} = -b\frac{\partial^2 V}{\partial z^2} + 2c(|V|^2 + B|U|^2)V, \tag{9.2}$$

where U and V are complex envelopes of the two polarizations, assumed to have identical group velocities and group-velocity dispersion, t is the propagation time, z is the longitudinal position coordinate in the moving frame of the pulses, b is the group-velocity dispersion coefficient, c is the self-phase modulation coefficient, and Bc is the cross-phase modulation coefficient. For example, $B = 2/3$ for linear polarizations in a linearly birefringent fiber [16], $B = 2$ for circular polarizations in an isotropic fiber [17], and $B = 1$ describes Manakov solitons [18], realizable in an elliptically birefringent fiber [16]. For solitons to exist, it is required that $bc < 0$.

Equations (9.1) and (9.2) can be quantized using the Hamiltonian below,

$$\hat{H} = \hbar \int dz \left[b\Big(\frac{\partial \hat{U}^\dagger}{\partial z}\frac{\partial \hat{U}}{\partial z} + \frac{\partial \hat{V}^\dagger}{\partial z}\frac{\partial \hat{V}}{\partial z} \Big) + c\Big(\hat{U}^\dagger\hat{U}^\dagger\hat{U}\hat{U} + \hat{V}^\dagger\hat{V}^\dagger\hat{V}\hat{V} + 2B\hat{U}^\dagger\hat{V}^\dagger\hat{U}\hat{V} \Big) \right], \tag{9.3}$$

where $\hat{U}$ and $\hat{V}$ are photon annihilation operators of the two polarizations and the daggers denote the corresponding creation operators. The Heisenberg equations of motion derived from Eq. (9.3) are analyzed using perturbative techniques by Rand *et al.* [19], who study the specific case of Manakov solitons, and by Lantz *et al.* [20] and Lee *et al.* [21], who numerically investigate the photon number entanglement in higher-order vector solitons. As opposed to these previous studies, in this chapter the exact quantum vector soliton solution is derived in the Schrödinger picture, in the spirit of the scalar soliton analyses in Refs. [7, 8].

Since the Hamiltonian conserves photon number in each mode and the mean momentum, one can construct simultaneous Fock and momentum eigenstates with the Bethe ansatz [7, 22],

$$|n,m,p\rangle = \frac{1}{\sqrt{n!m!}} \int d^n x\, d^m y\; f_{nmp}(x_1,...,x_n,y_1,...,y_m)\hat{U}^\dagger(x_1)...\hat{U}^\dagger(x_n)\hat{V}^\dagger(y_1)...\hat{V}^\dagger(y_m)|0\rangle, \tag{9.4}$$

where n and m are the photon numbers in the two polarizations and p is the mean momentum. Using the Schrödinger equation $E|\Psi\rangle = \hat{H}|\Psi\rangle$, one obtains

$$\begin{aligned} & E_{nmp} f_{nmp}(x_1,...,x_n,y_1,...,y_m) \\ &= \hbar\Big\{ -b\sum_j \frac{\partial^2}{\partial x_j^2} - b\sum_k \frac{\partial^2}{\partial y_k^2} + 2c\Big[\sum_{i<j}\delta(x_j - x_i) + \sum_{l<k}\delta(y_k - y_l) + B\sum_{j,k}\delta(x_j - y_k) \Big] \Big\} \times \\ & f_{nmp}(x_1,...,x_n,y_1,...,y_m). \end{aligned} \tag{9.5}$$

The soliton solution of Eq. (9.5) is

$$f_{nmp} = C_{nm} \exp\left[ip\Big(\sum_j x_j + \sum_k y_k \Big) + \frac{c}{2b}\Big(\sum_{i<j}|x_j - x_i| + \sum_{l<k}|y_k - y_l| + B\sum_{j,k}|x_j - y_k| \Big) \right], \tag{9.6}$$

where C_{nm} is a normalization constant. The energy can be calculated by substituting Eq. (9.6) into Eq. (9.5) and is given by

$$E_{nmp} = \hbar b N p^2 - \frac{\hbar c^2}{12b}\Big[n(n^2-1) + m(m^2-1) + 3B^2 nm(n+m) \Big], \tag{9.7}$$

where $N = n + m$. A physical state should contain a distribution of momentum states, say a Gaussian, such

that the time-dependent multiphoton probability amplitude is now given by

$$f_{nm} = \int dp \, \frac{1}{(2\pi\Delta p^2)^{\frac{1}{4}}} \exp\Big(-\frac{p^2}{4\Delta p^2} - ibNp^2t\Big) f_{nmp} \tag{9.8}$$

$$= C_{nm}(8\pi)^{\frac{1}{4}} \Big(\frac{\Delta p}{1+4ibN\Delta p^2 t}\Big)^{\frac{1}{2}} \exp\Big[-\frac{\Delta p^2}{1+4ibN\Delta p^2 t}\Big(\sum_j x_j + \sum_k y_k\Big)^2\Big] \times \tag{9.9}$$

$$\exp\Big[\frac{c}{2b}\Big(\sum_{i<j}|x_j - x_i| + \sum_{l<k}|y_k - y_l| + B\sum_{j,k}|x_j - y_k|\Big)\Big], \tag{9.10}$$

where Δp is determined by initial conditions and a constant energy term that does not affect the position and momentum properties of a Fock state is omitted. Although a more realistic soliton state should have a superposition of Fock states resembling a coherent state [7], the Fock components of a coherent state for $N >> 1$ have photon numbers very close to the mean value, so a Fock state should be able to adequately represent the position and momentum properties of a coherent-state soliton.

9.2.2 Adiabatic soliton expansion

The multiphoton amplitude f_{nm} consists of two components: a dispersive pulse-center component given by Eq. (9.9) that governs the quantum dispersion of the mean photon position $1/N(\sum_j x_j + \sum_k y_k)$, and a bound-state component given by Eq. (9.10) that fixes the distances among the photons via the attractive Kerr potentials. Scalar solitons possess the same properties [7, 8], and it can be argued that all vector solitons with any number of modes under the effects of group-velocity dispersion, self-phase modulation, and cross-phase modulation must also be comprised of such two components. It follows that the momentum-space probability amplitude, defined as the N-dimensional Fourier transform of f_{nm}, also consists of a mean momentum component and a bound-state component that governs the relative momenta among the photons. If one increases b or reduces c adiabatically, the multiphoton amplitude would remain in the same form, but with increased uncertainties in the relative distances as well as reduced uncertainties in the relative momenta. More crucially, the mean momentum uncertainty remains unaffected, leading to a multiphoton state with positive momentum correlations. The adiabatic approximation remains valid if the change happens over a propagation time scale $T >> \hbar/|E(t=T) - E(t=0)|$, which is on the order of the initial soliton period divided by N. As optical fiber solitons can typically propagate for a few soliton periods before loss becomes a factor, the desired adiabatic expansion should be realizable with current technology. In the following it is assumed for simplicity that only c is adiabatically varied. Mathematically, in the limit of vanishing c, the bound-state component becomes relatively flat, and f_{nm} becomes solely governed by the pulse-center component,

$$f_{nm} \propto \exp\Big[-\frac{\Delta p^2}{1+4ibN\Delta p^2 t}\Big(\sum_j x_j + \sum_k y_k\Big)^2\Big]. \tag{9.11}$$

In the momentum space, as the bandwidth of the relative momenta is reduced and becomes much smaller than the bandwidth of the mean momentum, the wavefunction in terms of momentum eigenstates becomes

$$|\Psi\rangle \propto \int dp\ \exp\Big(-\frac{p^2}{4\Delta p^2} - ibNp^2t\Big)|n_p, m_p\rangle, \tag{9.12}$$

where $|n_p, m_p\rangle$ denotes a momentum eigenstate with momentum p and n and m photons in the respective polarizations. Except for the dispersive phase term, Eq. (9.12) is precisely the desired coincident frequency state that can achieve the ultimate limit of mean position accuracy [2], as frequency is trivially related to momentum via the dispersion relation. The same operation of position squeezing on a scalar soliton is previously considered by Fini and Hagelstein, who nonetheless dismiss this possibility due to the detrimental effect of quantum dispersion [9].

9.2.3 Quantum dispersion compensation

Fortunately, quantum dispersion, like classical dispersion, can be compensated with classical dispersion management. If the vector soliton propagates in another waveguide with an opposite group-velocity dispersion, then the dispersive phase term in Eq. (9.8) can be cancelled, thus restoring the minimum uncertainty in the mean photon position. The complete setup of generating multiphoton states with positive frequency correlations is sketched in Fig. 9.1. To apply the presented scheme to a spatial vector soliton, negative refraction, which can be achieved in a negative-refractive-index material [23], or a photonic crystal [24], is required to compensate for the quantum diffraction instead.

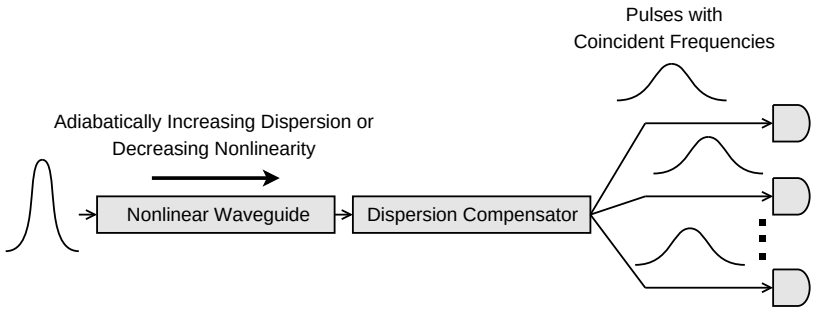

Figure 9.1: Proposed setup of generating multiphoton states with quantum-enhanced mean position accuracy via adiabatic control of vector solitons. A pulse is coupled into a vector soliton in a multimode nonlinear waveguide, in which dispersion adiabatically increases or the Kerr nonlinearity adiabatically decreases. A second waveguide with an opposite dispersion is used for compensating the quantum dispersive spreading of the mean position.

9.3 Temporal correlations among photons

In order to understand how the quantum vector soliton solution corresponds to a classical soliton in typical experiments and how much adiabatic pulse expansion is needed to reach the ultimate quantum limit, consider the specific case of a Manakov soliton, where $B = 1$. Other vector solitons should have very similar properties given the similarity of the solutions. If the photon position variables are re-indexed in the following new notations,

$$\{z_1, ..., z_N\} = \{x_1, ..., x_n, y_1, ..., y_m\}, \tag{9.13}$$

the multiphoton amplitude in Eqs. (9.9) and (9.10) becomes

$$f_{nm} = C_{nm}(8\pi)^{1/4}\Big(\frac{\Delta p}{1+4ibN\Delta p^2 t}\Big)^{\frac{1}{2}} \exp\left[-\frac{\Delta p^2}{1+4ibN\Delta p^2 t}\Big(\sum_j z_j\Big)^2 + \frac{c}{2b}\sum_{i<j}|z_j - z_i|\right]. \tag{9.14}$$

Intriguingly, this solution is exactly the same as the scalar soliton solution [7], or in other words, a Manakov soliton is quantum-mechanically equivalent to a scalar soliton. This equivalence explains the discovery by Rand *et al.* that the squeezing effect of a Manakov soliton has the same optimum as a scalar soliton [19]. Moreover, C_{nm} can now be borrowed from the scalar soliton analysis and is given by $C_{nm} = [(N-1)!|c/b|^{N-1}/(2\pi)]^{1/2}$ [7]. The knowledge of C_{nm} allows one to calculate the correlations among the photon positions using standard statistical mechanics techniques. An expression for $\big\langle \sum_{i<j}|z_j - z_i|\big\rangle$ can be derived, and by symmetry,

$$\big\langle |z_j - z_i| \big\rangle = \frac{1}{N(N-1)}\left\langle \sum_{i<j}|z_j - z_i| \right\rangle = \Big|\frac{2b}{Nc}\Big| \sim W_0. \tag{9.15}$$

As expected, the average absolute distance between any two photons is on the order of the classical soliton pulse width, $W_0 \sim |2b/(Nc)|$ [7]. Next, assume that the variance of the relative distance is related to the square of the average absolute distance by a parameter q,

$$\big\langle |z_j - z_i|^2 \big\rangle = q\big\langle |z_j - z_i| \big\rangle^2 = \frac{4qb^2}{N^2c^2}. \tag{9.16}$$

While an explicit expression for q is hard to derive, q must only depend on N by dimensional analysis, must be larger than 1 because $\big\langle |z_j - z_i|^2 \big\rangle \geq \big\langle |z_j - z_i| \big\rangle^2$, and is likely to be on the order of unity, as will be shown later. Eq. (9.16) then gives

$$\big\langle |z_j - z_i|^2 \big\rangle = \big\langle z_j^2 \big\rangle - 2\big\langle z_i z_j \big\rangle + \big\langle z_i^2 \big\rangle = 2\big\langle z_j^2 \big\rangle - 2\big\langle z_i z_j \big\rangle, \tag{9.17}$$

$$\big\langle z_j^2 \big\rangle - \big\langle z_i z_j \big\rangle = \frac{2qb^2}{N^2c^2}. \tag{9.18}$$

Furthermore, the variance of $\sum_j z_j$ is simply given by

$$\left\langle \left(\sum_j z_j \right)^2 \right\rangle = N \left\langle z_j^2 \right\rangle + N(N-1) \left\langle z_i z_j \right\rangle = \Delta z^2, \tag{9.19}$$

$$\Delta z^2 = \frac{1}{4\Delta p^2} + 4\Big(bN\Delta pt \Big)^2. \tag{9.20}$$

From Eqs. (9.18) and (9.19) the covariances can be obtained explicitly,

$$\left\langle z_j^2 \right\rangle = \frac{\Delta z^2}{N^2} + \frac{2q(N-1)b^2}{N^3c^2}, \quad \left\langle z_i z_j \right\rangle = \frac{\Delta z^2}{N^2} - \frac{2qb^2}{N^3c^2}. \tag{9.21}$$

A quantum soliton solution best resembles a classical initial condition with independent photons when the initial covariance is zero,

$$\left\langle z_i z_j \right\rangle_{t=0} = \frac{1}{4N^2\Delta p^2} - \frac{2qb^2}{N^3c^2}\Big|_{t=0} = 0, \tag{9.22}$$

$$\Delta p = \Big| \frac{\sqrt{N}c}{\sqrt{8q}b} \Big|_{t=0} \sim \frac{1}{2\sqrt{N}W_0}. \tag{9.23}$$

Incidentally, the mean momentum uncertainty Δp is at the shot-noise level when the photons are initially uncorrelated. This justifies the assumption that q is on the order of unity. An initial condition with independent photons would then mostly couple to a soliton state with Δp given by Eq. (9.23), while coupling to continuum states should be negligible. Adiabatically increasing $|b/c|$ then makes $\left\langle z_i z_j \right\rangle$ negative and therefore introduces the necessary negative correlations among the photon positions. If the ratio between the final and initial values of $|b/c|$ is γ, for $N >> 1$ and $\gamma << \sqrt{N}$, the pulse bandwidth is reduced by a factor of γ according to the classical theory. The accuracy enhancement over the standard quantum limit for the same reduced bandwidth is hence also given by γ in the regime of moderate expansion. The multiphoton state becomes that given by Eqs. (9.11) and (9.12) and the ultimate limit is reached only when $\gamma >> \sqrt{N}$.

9.4 Temporal entanglement between optical pulses

As the photons across different optical modes become correlated via the cross-phase modulation effect, entanglement is expected among the pulse positions in a vector soliton. To estimate the magnitude of the entanglement in terms of macroscopic position variables, consider again the case of Manakov solitons. Let the pulse center coordinates of the respective polarizations be X and Y, defined as $X = 1/n\sum_{j=1}^{n} z_j$ and $Y = 1/m\sum_{k=m+1}^{N} z_k$. If there is an equal number of photons in each polarization such that $n = m = N/2$, The following statistics for X and Y can be calculated using Eqs. (9.21),

$$\left\langle (\frac{X+Y}{2})^2 \right\rangle = \frac{\Delta z^2}{N^2}, \quad \left\langle (\frac{X-Y}{2})^2 \right\rangle = \frac{2qb^2}{N^3c^2}. \tag{9.24}$$

Similar to a two-photon vector soliton [4], the mean position of the two pulses is affected by quantum dispersion, while the relative distance is bounded by the Kerr effect. For two initially uncorrelated pulses, Eqs. (9.24) give the same value, but as the vector soliton propagates, Δz grows due to quantum dispersion, leading to a positive temporal correlation between the two pulses. This correlation, however, does not result in the EPR paradox, as the joint spectrum in terms of the conjugate momenta with respect to X and Y does not change. If, on the other hand, b and c are adiabatically manipulated, then the nonlocal uncertainty product $\left\langle (X-Y)^2 \right\rangle \left\langle (P_X - P_Y)^2 \right\rangle$, where P_X and P_Y are the conjugate momenta, can remain constant under the adiabatic approximation while $\left\langle (X-Y)^2 \right\rangle$ and $\left\langle (P_X - P_Y)^2 \right\rangle$ are varied, resulting in EPR entanglement. Combined with quantum temporal imaging techniques, which are able to temporally reverse, compress, and expand photons in each mode [4], adiabatic vector soliton control potentially provides a powerful way of fiber-based continuous-variable quantum information processing [14].

Bibliography

[1] V. Giovannetti, S. Lloyd, and L. Maccone, Science **306**, 1330 (2004).

[2] V. Giovannetti, S. Lloyd, and L. Maccone, Nature (London) **412**, 417 (2001).

[3] V. Giovannetti, L. Maccone, J. H. Shapiro, and F. N. C. Wong, Phys. Rev. Lett. **88**, 183602 (2002); Z. D. Walton, M. C. Booth, A. V. Sergienko, B. E. A. Saleh, and M. C. Teich, Phys. Rev. A **67**, 053810 (2003); J. P. Torres, F. Macia, S. Carrasco, and L. Torner, Opt. Lett. **30**, 314 (2005); M. Tsang and D. Psaltis, Phys. Rev. A **71**, 043806 (2005).

[4] M. Tsang and D. Psaltis, Phys. Rev. A **73**, 013822 (2006).

[5] O. Kuzucu, M. Fiorentino, M. A. Albota, F. N. C. Wong, and F. X. Kärtner, Phys. Rev. Lett. **94**, 083601 (2005).

[6] G. P. Agrawal, *Nonlinear Fiber Optics* (Academic Press, San Diego, 2001).

[7] Y. Lai and H. A. Haus, Phys. Rev. A **40**, 844 (1989); *ibid.* **40**, 854 (1989).

[8] F. X. Kärtner and H. A. Haus, Phys. Rev. A **48**, 2361 (1993); P. L. Hagelstein, *ibid.* **54**, 2426 (1996).

[9] J. M. Fini and P. L. Hagelstein, Phys. Rev. A **66**, 033818 (2002).

[10] See, for example, A. Sizmann, Appl. Phys. B **65**, 745 (1997), and references therein; C. Silberhorn *et al.*, Phys. Rev. Lett. **86**, 4267 (2001).

[11] See, for example, M. N. Islam, Opt. Lett. **14**, 1257 (1989); J. U. Kang, G. I. Stegeman, J. S. Aitchison, and N. Akhmediev, Phys. Rev. Lett. **76**, 3699 (1996); Y. Barad and Y. Silberberg, *ibid.* **78**, 3290 (1997); S. T. Cundiff *et al.*, *ibid.* **82**, 3988 (1999).

[12] S. M. Barnett, C. Fabre, and A. Mâitre, Eur. Phys. J. D **22**, 513 (2003).

[13] A. Einstein, B. Podolsky, and N. Rosen, Phys. Rev. **47**, 777 (1935).

[14] S. L. Braunstein and P. van Loock, Rev. Mod. Phys. **77**, 513 (2005).

[15] B. Crosignani and P. Di Porto, Opt. Lett. **6**, 329 (1981); F. T. Hioe, Phys. Rev. Lett. **82**, 1152 (1999).

[16] C. R. Menyuk, IEEE J. Quantum Electron. **25**, 2674 (1989).

[17] A. L. Berkhoer and V. E. Zakharov, Sov. Phys. JETP **31**, 486 (1970).

[18] S. V. Manakov, Sov. Phys. JETP **38**, 248 (1974).

[19] D. Rand, K. Steiglitz, and P. R. Prucnal, Phys. Rev. A **71**, 053805 (2005).

[20] E. Lantz, T. Sylvestre, H. Maillotte, N. Treps, and C. Fabre, J. Opt. B **6**, 295 (2004).

[21] R.-K. Lee, Y. Lai, and B. A. Malomed, Phys. Rev. A **71**, 013816 (2005).

[22] H. B. Thacker, Rev. Mod. Phys. **53**, 253 (1981).

[23] V. G. Veselago, Sov. Phys. Usp. **10**, 509 (1968); J. B. Pendry, Phys. Rev. Lett. **85**, 3966 (2000).

[24] C. Luo, S. G. Johnson, J. D. Joannopoulos, and J. B. Pendry, Phys. Rev. B **65**, 201104(R) (2002).

Chapter 10

Beating the spatial standard quantum limits via adiabatic soliton expansion and negative refraction

10.1 Introduction

In many optical imaging applications, such as atomic force microscopy [1] and nanoparticle detection [2], precise measurements of the displacement of an optical beam are required. It is hence important to know what the fundamental limit on the accuracy of such measurements is placed by the laws of physics, and how one can approach this limit in an experiment. It is now known that if an optical beam consists of N independent photons with wavelength λ, then the minimum uncertainty in its spatial displacement is on the order of $\lambda/\sqrt{N}$, the so-called standard quantum limit [3]. The ultimate uncertainty permissable by quantum mechanics, however, is smaller than the standard quantum limit by another factor of $\sqrt{N}$ [3]. An experiment that beats this standard quantum limit with nonclassical multimode light has already been demonstrated [4]. On the other hand, in other optical imaging applications, such as lithography, microscopy, and data storage, detection of extremely small features of an object is desired. The feature size of an optical intensity pattern cannot be smaller than λ, due to the resolution limit [5]. Multiphoton absorption allows detection of smaller feature sizes, and the minimum feature size of multiphoton absorption using a classical coherent light source is on the order of $\lambda/\sqrt{N}$ [6], which can be regarded as the standard quantum limit on the multiphoton absorption feature size. Nonclassical light sources allow one to do better, and the ultimate limit is smaller than the standard one by another factor of $\sqrt{N}$ [6, 7]. A proof-of-concept experiment of this resolution enhancement has also been demonstrated [8]. In the time domain, very similar quantum limits on the position accuracy of an optical pulse can be derived [9]. Given the striking similarities among the spatiotemporal quantum limits, one expects them to be closely related to each other, yet the formalisms used to described each of them are vastly different [3, 6, 7, 9], so a more general formalism applicable to all spatiotemporal domains would greatly facilitate our understanding towards the spatiotemporal quantum enhancement effects.

In this chapter, we apply the temporal formalism used by Giovannetti *et al.* [9] to the spatial domain, and show that the uncertainty in the beam displacement and the spot size of multiphoton absorption are in fact closely related. Using this newly derived result, we demonstrate how one can generate arbitrary multiphoton interference patterns with a continuous superposition of coincident momentum states. We further present an unfortunate result, namely that the multiphoton absorption rate is reduced if the quantum lithography resolution is enhanced, contrary to popular belief [6]. Finally, we take advantage of the general spatiotemporal framework to show that the idea of adiabatic soliton expansion, previously proposed to beat the temporal standard quantum limit [10], can also be used to beat both spatial standard quantum limits and approach the ultimate limits with an arbitrary number of photons. The use of solitons is an attractive alternative to the more conventional use of second-order nonlinearity for quantum information processing, because the soliton effect bounds the photons together and allows a much longer interaction length for significant quantum correlations to develop among the photons.

10.2 Formalism

Consider N photons with the same frequency ω and polarization that propagate in the $x-z$ plane. A general wavefunction that describes such photons is given by [11]

$$|\Psi\rangle = \frac{1}{\sqrt{N!}} \int dk_1 dk_2 ... dk_N \; \phi(k_1, k_2, ..., k_N) |k_1, k_2, ..., k_N\rangle. \tag{10.1}$$

where $|k_1, ..., k_N\rangle$ is the momentum eigenstate, $k_1, ..., k_N$ specify the transverse wave vectors of the photons along the x axis, and $\phi(k_1, ..., k_N)$ is defined as the multiphoton momentum probability amplitude. The longitudinial wave vectors are all assumed to be positive. One can also define the corresponding quantities in real space,

$$|x_1, ..., x_N\rangle = \int \frac{dk_1}{\sqrt{2\pi}} ... \frac{dk_N}{\sqrt{2\pi}} \exp(-ik_1 x_1 - ... - ik_N x_N) |k_1, ..., k_N\rangle, \tag{10.2}$$

$$\psi(x_1, ..., x_N) = \int \frac{dk_1}{\sqrt{2\pi}} ... \frac{dk_N}{\sqrt{2\pi}} \phi(k_1, ..., k_N) \exp(ik_1 x_1 + ... + ik_N x_N), \tag{10.3}$$

$$|\Psi\rangle = \frac{1}{\sqrt{N!}} \int dx_1 ... dx_N \psi(x_1, ..., x_N) |x_1, ..., x_N\rangle, \tag{10.4}$$

where $\psi(x_1, ..., x_N)$ is the multiphoton spatial probability amplitude. ϕ and ψ are subject to normalization conditions $\int dk_1 ... dk_N |\phi|^2 = \int dx_1 ... dx_N |\psi|^2 = 1$, and ϕ and ψ must be symmetric under any exchange of labels due to the bosonic nature of photons. The magnitude squared of ψ gives the joint probability

distribution of the positions of the photons,

$$\langle : I(x_1)...I(x_N) : \rangle \propto \frac{1}{N!}\langle \Psi | \hat{A}^\dagger(x_1)...\hat{A}^\dagger(x_N)\hat{A}(x_1)...\hat{A}(x_N)|\Psi\rangle \tag{10.5}$$

$$= |\psi(x_1,...,x_N)|^2, \tag{10.6}$$

where $\hat{A}(x_i)$ and $\hat{A}^\dagger(x_i)$ are the spatial annihilation and creation operators, respectively. The statistical interpretation of ψ is valid because we only consider photons that propagate in the positive z direction. The above definition of a multiphoton state is more general than those used by other authors, in the sense that we allow photons with arbitrary momenta, compared with the use of only one even spatial mode and one odd mode by Fabre *et al.* [3], the use of only two discrete momentum states by Boto *et al.* [6], and the use of many discrete momentum states by Björk *et al.* [7].

The displacement of an optical beam can be represented by the following operator,

$$\hat{X} = \frac{1}{N}\int dx\, x\hat{A}^\dagger(x)\hat{A}(x). \tag{10.7}$$

Applying $\hat{X}$ to $|x_1,...,x_N\rangle$ gives

$$\hat{X}|x_1,...,x_N\rangle = \left(\frac{1}{N}\sum_{i=1}^{N} x_i\right)|x_1,...,x_N\rangle, \tag{10.8}$$

so the beam displacement can be intuitively regarded as the mean position of the photons under the statistical interpretation. If we assume that $\langle \hat{X} \rangle = 0$ for simplicity, the displacement uncertainty is given by

$$\langle \hat{X}^2 \rangle^{1/2} = \left[\int dx_1...dx_N \left(\frac{1}{N}\sum_{i=1}^{N} x_i\right)^2 |\psi(x_1,...,x_N)|^2\right]^{1/2}. \tag{10.9}$$

It is often more convenient to use a different system of coordinates as follows [12],

$$X = \frac{1}{N}\sum_{i=1}^{N} x_i, \quad \xi_i = x_i - X,\ i = 1,...,N-1, \quad \xi_N = -\sum_{i=1}^{N-1}\xi_i. \tag{10.10}$$

X is therefore the "center-of-mass" coordinate that characterizes the overall displacement of the optical beam, and ξ_i's are relative coordinates. Defining a new probability amplitude in terms of these coordinates,

$$\psi'(X,\xi_1,...,\xi_{N-1}) = \psi(X+\xi_1,...,X+\xi_N), \tag{10.11}$$

we obtain the following expression for the displacement uncertainty,

$$\left\langle \hat{X}^2 \right\rangle^{1/2} = \left[\frac{1}{N} \int dX d\xi_1 ... \xi_{N-1} \, X^2 |\psi'(X, \xi_1, ..., \xi_{N-1})|^2 \right]^{1/2} \tag{10.12}$$

$$= \left\langle X^2 \right\rangle^{1/2}, \tag{10.13}$$

which is the marginal width of ψ' with respect to X.

On the other hand, the dosing operator of N-photon absorption is [6]

$$\left\langle : I^N(x) : \right\rangle \propto |\psi(x, x, ..., x)|^2 = |\psi'(x, 0, ..., 0)|^2, \tag{10.14}$$

which is, intuitively, the probability distribution of all N photons arriving at the same place x. Hence, designing a specified multiphoton interference pattern in quantum lithography is equivalent to engineering the conditional probability distribution $|\psi'(X, 0, ..., 0)|^2$. In particular, the spot size of multiphoton absorption is the conditional width of ψ' with respect to X,

$$\left[\int dx \, x^2 \left\langle : I^N(x) : \right\rangle \right]^{1/2} \propto \left[\int dX \, X^2 |\psi'(X, 0, ..., 0)|^2 \right]^{1/2} \tag{10.15}$$

$$= \left\langle X^2 \right\rangle^{1/2} |_{\xi_1 = ... = \xi_{N-1} = 0}. \tag{10.16}$$

Despite the subtle difference between the marginal width and the conditional width, if ψ' can be made separable in the following way,

$$\psi'(X, \xi_1, ..., \xi_{N-1}) = \overline{\psi}(X) \psi_{rel}(\xi_1, ..., \xi_{N-1}), \tag{10.17}$$

then both widths are identical, and one can optimize the multiphoton state simultaneously for both applications.

The standard quantum limit on the uncertainty in X is obtained when the photons are spatially independent, such that $\psi(x_1, ..., x_N) = f(x_1) ... f(x_N)$. For example, if $f(x)$ is a Gaussian given by $f(x) \propto \exp\left(-\frac{\kappa^2 x^2}{2}\right)$, then both the marginal and conditional uncertainties in X are

$$\left\langle X^2 \right\rangle_{SQL}^{1/2} = \left\langle X^2 \right\rangle_{SQL}^{1/2} \Big|_{\xi_1 = ... = \xi_{N-1} = 0} = \frac{1}{\sqrt{2N}\kappa}. \tag{10.18}$$

Similar to the optimization of temporal position accuracy [9], the ultimate quantum limits on spatial displacement accuracy and quantum lithography feature size are achieved with the following nonclassical state,

$$|\Psi\rangle = \int dk G(k) |k, k, ..., k\rangle. \tag{10.19}$$

The momentum probability amplitude is then

$$\phi(k_1,...,k_N) = G(k_1)\delta(k_1-k_2)\delta(k_1-k_3)...\delta(k_1-k_N), \tag{10.20}$$

which characterizes N photons with coincident momentum. The spatial amplitude is thus given by

$$\psi'(X,\xi_1,...,\xi_N) = \int \frac{dk}{\sqrt{2\pi}} G(k)\exp(iNkX) \equiv g(NX), \tag{10.21}$$

which is a function of X only and can be understood as a continuous superposition of N-photon states, each with an effective de Broglie wavelength equal to $2\pi/(Nk)$. The multiphoton interference pattern is therefore trivially given by $|g(NX)|^2$, the magnitude squared of the Fourier transform of $G(k)$. An arbitrary interference pattern can hence be generated, if an appropriate $G(k)$ can be engineered. This approach of designing the multiphoton interference pattern should be compared with the less direct approaches by the use of discrete momentum states [6, 7]. With the resolution limit, $G(k)$ is zero for $|k| > 2\pi/\lambda$, so given the Fourier transform relation between $G(k)$ and $g(NX)$, the minimum feature size of multiphoton interference is on the order of λ/N.

To compare the ultimate uncertainty in X with the standard quantum limit, let $G(k)$ be a Gaussian given by $G(k) \propto \exp\left(-\frac{k^2}{2\kappa^2}\right)$, then the uncertainty in X becomes

$$\left\langle X^2 \right\rangle_{UQL}^{1/2} = \frac{1}{\sqrt{2}N\kappa}, \tag{10.22}$$

which is smaller than the standard quantum limit, Eq. (10.18), by another factor of $\sqrt{N}$, as expected.

10.3 Multiphoton absorption rate of nonclassical states

Let us recall Boto *et al.*'s heuristic argument concerning the multiphoton absorption rate of entangled photons. They claim that, because entangled photons tend to arrive at the same place at the same time, the multiphoton absorption rate must be enhanced [6]. If photons tend to arrive at the same place, then the uncertainty in their relative positions must be small. However, the spatial probability amplitude that achieves the ultimate lithographic resolution, Eq. (10.21), is a function of X only, which means that the uncertainty in the relative positions is actually infinite. In general, any enhancement of resolution with respect to X must result in a corresponding reduction in the bandwidths with respect to the relative positions, in order to maintain the same maximum bandwidth. By the Heisenberg uncertainty principle, such photons must then have increased uncertainty in their relative positions. Hence, Boto *et al.*'s argument manifestly does not hold for photons with a quantum-enhanced lithographic resolution. In fact, the opposite is true: Although these photons have a reduced uncertainty in their average position, they must have an increased uncertainty in their relative positions, so they do not arrive at the same place very often, and the multiphoton absorption rate must be

reduced. To observe this fact, consider the total multiphoton absorption rate,

$$\int dx \left\langle : I^N(x) : \right\rangle \propto \int dX |\psi'(X,0,...,0)|^2. \tag{10.23}$$

Because ψ' must satisfy the normalization condition,

$$\frac{1}{N}\int dX d\xi_1 ... d\xi_N |\psi'(X,\xi_1,...,\xi_N)|^2 = 1, \tag{10.24}$$

a larger uncertainty in ξ_i's means that $|\psi'(X,0,...,0)|^2$ must be smaller, leading to a reduced multiphoton absorption rate. Conversely, photons that tend to arrive together must have a larger uncertainty in where they arrive, so an enhanced multiphoton absorption rate means that the quantum lithographic resolution must be sacrificed. That said, one can still compensate for the reduction in the multiphoton absorption rate due to an enhanced resolution in one dimension, by reducing the relative positions of the photons in the other unused space and time dimensions.

10.4 Generating nonclassical states via the soliton effect

We now turn to the problem of producing the nonclassical multiphoton states for spatial quantum enhancement. As we have established a general formalism that resembles the temporal one, schemes that produce temporal quantum enhancement can be applied to the spatial domain as well. In particular, a scheme that makes use of temporal solitons is recently proposed to enhance the temporal accuracy of an optical pulse [10]. We here proceed to show how spatial solitons can be utilized to enhance the beam displacement accuracy, as well as reduce the spot size of multiphoton absorption, beyond the standard quantum limits and approaching the ultimate quantum limits.

Consider the Hamiltonian that describes the one-dimensional diffraction effect and Kerr nonlinearity,

$$\hat{H} = \int dx \left[-b \frac{\partial \hat{A}^\dagger}{\partial x} \frac{\partial \hat{A}}{\partial x} + c \hat{A}^\dagger \hat{A}^\dagger \hat{A} \hat{A} \right], \tag{10.25}$$

where b is the Fresnel diffraction coefficient, assumed to be positive, and c is the negative Kerr coefficient, assumed to be negative, so that $b/c < 0$ and solitons can exist under the self-focusing effect. The soliton solution of the spatial amplitude for N photons under this Hamiltonian is [13]

$$\psi = C \int \frac{dk}{\sqrt{2\pi}} G(k) \exp\left[ik \sum_i x_i + \frac{c}{2b} \sum_{i<j} |x_i - x_j| - ibNk^2 t + i \frac{c^2}{12b} N(N^2-1)t \right], \tag{10.26}$$

where $C = \sqrt{(N-1)!|c/b|^{N-1}/(2\pi)}$ and $G(k)$ is determined by the initial conditions. If initially the photons

are uncorrelated, $G(k)$ can be approximated as [10]

$$G(k) \propto \exp\Big(-\frac{k^2}{2\kappa^2}\Big), \quad \kappa = \left|\sqrt{\frac{N}{4q}}\frac{c}{b}\right| \sim \frac{1}{\sqrt{N}W_0}, \tag{10.27}$$

where q is a parameter on the order of unity [10], and W_0 is the initial soliton beam width. The probability amplitude can be written in terms of the center-of-mass and relative coordinate system defined in Eqs. (10.10) as

$$\psi' = C\int \frac{dk}{\sqrt{2\pi}} G(k) \exp\left[iNkX + \frac{c}{2b}\sum_{i<j}|\xi_i - \xi_j| - ibNk^2t + i\frac{c}{12b}N(N^2-1)t\right], \tag{10.28}$$

which is separable in the way described by Eq. (10.17), meaning that the conditional width and marginal width with respect to X are identical. If we adiabatically reduce c or increase b, then we can reduce the uncertainty in the relative momenta of the photons and increase the uncertainty in the relative positions [10]. Classically, we expect the soliton beam width to expand and the spatial bandwidth to be reduced, But the most crucial difference in the quantum picture is that the center-of-mass coordinate X remains unaffected during the adiabatic soliton expansion, apart from the quantum dispersion term $-ibNk^2t$.

As pointed out in Ref. [10], the quantum dispersion term can be compensated if the soliton propagates in a second medium with an opposite diffraction coefficient b'. Full compensation is realized when $\int_0^T b(t)dt = -\int_0^{T'} b'(t)dt$, where T is the propagation time in the first medium and T' is the propagation time in the second medium. Negative refraction, realizable in a left-handed material [14] or a photonic crystal [15] for example, is hence required in the second medium. Ideally the second medium should also have a Kerr coefficient c' opposite to the final value of c in the first medium, such that $c' = -c(T)$, so that $b'/c' < 0$ and the quantum soliton maintains its shape, but in practice $c' = 0$ would also suffice, because the momentum bandwidths would remain unchanged in a linear medium while the quantum dispersion is being compensated.

In the limit of vanishing c/b in the first medium, the wavefunction would approach the ultimate multi-photon state given by Eq. (10.21). However, the bandwidth of $G(k)$ is very low, on the order of $1/(\sqrt{N}W_0)$, where W_0 is the initial soliton beam width, so the bandwidth of $G(k)$ is nowhere near the resolution limit and the uncertainty in X is the same as the input beam. In order to reduce this uncertainty, one can put the beam in a conventional imaging system [16] to recompress it, so that the output probability amplitude becomes

$$\psi_{out} = \frac{1}{\sqrt{M^N}}\psi_{in}\left(\frac{x_1}{M}, \frac{x_2}{M}, ..., \frac{x_N}{M}\right), \tag{10.29}$$

where M is the magnification factor. If M is smaller than 1, each photon is spatially compressed, thus reducing the ultimate quantum limit on the uncertainty in X. To illustrate, Fig. 10.1 shows a flowchart of the whole quantum enhancement process and a simple example of what the spatial and momentum probability amplitudes should look like in each step for two photons.

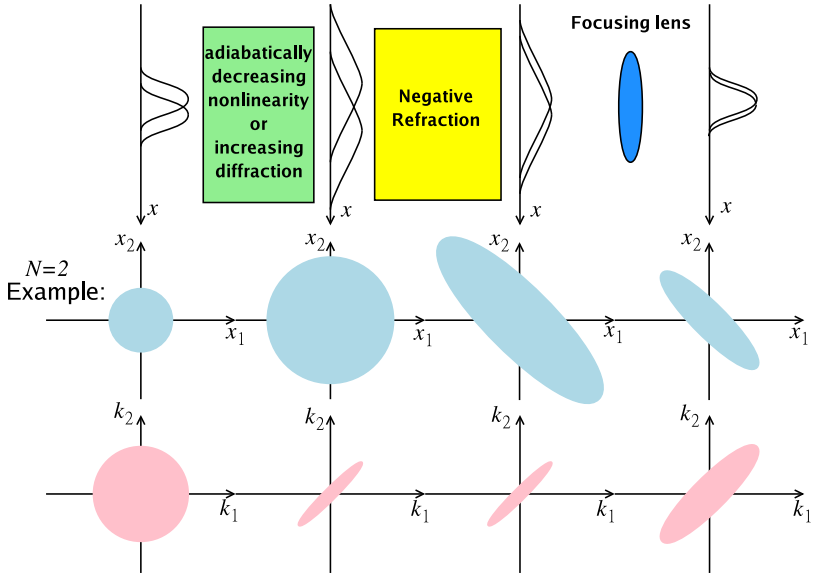

Figure 10.1: First row: schematics of the spatial quantum enhancement setup via adiabatic soliton expansion. Second row: sketches of the spatial probability amplitude, $\psi(x_1, x_2)$, for an example of two photons in each step of the process. Third row: sketches of the momentum probability amplitude, $\phi(k_1, k_2)$. Consult text for details of each step of the process.

10.5 Conclusion

In conclusion, spatial quantum enhancement effects are studied under a general framework. A method of generating arbitrary multiphoton interference pattern by the use of a continuous superposition of coincident momentum states is proposed. It is further shown that the multiphoton absorption rate is reduced if the lithographic resolution is enhanced. Finally, the use of adiabatic soliton expansion and negative refraction is proposed to beat the spatial standard quantum limits.

Bibliography

[1] C. A. J. Putman, B. G. De Grooth, N. F. Van Hulst, and J. Greve, J. Appl. Phys. **72**, 6 (1992).

[2] S. Kamimura, Appl. Opt. **26**, 3425 (1987).

[3] C. Fabre, J. B. Fouet, and A. Mâitre, Opt. Lett. **25**, 76 (2000); S. M. Barnett, C. Fabre, and A. Mâitre, Eur. Phys. J. D **22**, 513 (2003).

[4] N. Treps, U. Andersen, B. Buchler, P. K. Lam, A. Maître, H.-A. Bachor, and C. Fabre, Phys. Rev. Lett. **88**, 203601 (2002).

[5] M. Born and E. Wolf, *Principles of Optics* (Cambridge University Press, Cambridge, UK, 1999).

[6] A. N. Boto, P. Kok, D. S. Abrams, S. L. Braunstein, C. P. Williams, and J. P. Dowling, Phys. Rev. Lett. **85**, 2733 (2000); P. Kok, A. N. Boto, D. S. Abrams, C. P. Williams, S. L. Braunstein, and J. P. Dowling, Phys. Rev. A **63**, 063407 (2001).

[7] G. Björk, L. L. Sánchez-Soto, and J. Söderholm, Phys. Rev. Lett. **86**, 4516 (2001), G. Björk, L. L. Sánchez-Soto, and J. Söderholm, Phys. Rev. A **64**, 013811 (2001).

[8] M. D'Angelo, M. V. Chekhova, and Y. Shih, Phys. Rev. Lett. **87**, 013602 (2001).

[9] V. Giovannetti, S. Lloyd, and L. Maccone, Nature (London) **412**, 417 (2001).

[10] M. Tsang, e-print quant-ph/0603088 [submitted to Phys. Rev. Lett.].

[11] L. Mandel and E. Wolf, *Optical Coherence and Quantum Optics* (Cambridge University Press, Cambridge, UK, 1995).

[12] P. L. Hagelstein, Phys. Rev. A **54**, 2426 (1996).

[13] Y. Lai and H. A. Haus, Phys. Rev. A **40**, 844 (1989); *ibid.* **40**, 854 (1989).

[14] V. G. Veselago, Sov. Phys. Usp. **10**, 509 (1968); J. B. Pendry, Phys. Rev. Lett. **85**, 3966 (2000).

[15] C. Luo, S. G. Johnson, J. D. Joannopoulos, and J. B. Pendry, Phys. Rev. B **65**, 201104(R) (2002).

[16] J. W. Goodman, *Introduction to Fourier Optics* (McGraw-Hill, Boston, 1996).

Chapter 11

Reflectionless evanescent wave amplification via two dielectric planar waveguides

11.1 Introduction

Conventional optical imaging systems cannot resolve features smaller than the optical wavelength, because the high-spatial-frequency modes that describe the subwavelength features are evanescent waves, which exponentially decay away from the object and do not propagate to the far field. Observing the evanescent waves is therefore one of the most important yet formidable challenges in the field of optics, with important applications in optical lithography, data storage, and microscopy. Near-field scanning optical microscopy can detect the evanescent waves [1], but it requires scanning, which may not be desirable for many applications. A groundbreaking proposal by Pendry suggests that evanescent waves can be amplified without any reflection in a negative-refractive-index slab [2], causing significant interest as well as controversy [3] in the mechanism of evanescent wave amplification (EWA). On the practical side, the fabrication of a negative-refractive-index material for optical frequencies is a challenging task, as it requires both negative permittivity and negative permeability, the latter of which does not naturally occur in materials, and methods of implementing an effective negative refractive index [4, 5, 6] often introduce significant loss detrimental to the EWA process. As proposed by Pendry [2] and experimentally demonstrated by Fang *et al.* [7], a negative permittivity in a metal slab can also amplify evanescent waves to some extent, but the thickness of the slab is limited by the electrostatic approximation as well as loss. A simpler EWA scheme that utilizes less lossy materials would thus be desirable.

Along this direction, Luo *et al.* propose that a photonic crystal slab can be used to amplify evanescent waves [8], since evanescent waves with specific spatial frequencies can be coupled into the bound states of the photonic crystal slab, and the buildup of the bound states produces an enhanced evanescent tail on the other side of the slab. Apart from the difficulty in fabricating a three-dimensional photonic crystal for two-

dimensional imaging, the kind of EWA achieved by a photonic crystal slab is not ideal, because the buildup of the bound states also creates enhanced reflected evanescent waves, causing multiple evanescent wave reflections between the object and the photonic crystal. On the other hand, in order to obtain information about the output evanescent waves on the image plane, energy must be extracted, and the only way for the detector to "tell" the imaging system to give up energy is via a reflected evanescent wave. In other words, detection of an evanescent wave always creates a reflected evanescent wave, so there exist multiple reflections between an imaging system and the detector as well. Since the magnitudes of evanescent wave transmission and reflection coefficients can be larger than 1 or even infinite, multiple evanescent wave reflections can be very significant and should not be ignored in the design of near-field imaging systems. An ideal near-field imaging system should hence have 100% transmission as well as zero reflection, *as if the imaging system is not there and the object directly touches the image plane*. This ideal behavior also allows multiple imaging systems to be cascaded and a longer distance between the object and the detector.

In this chapter, the underlying physics of reflectionless evanescent wave amplification (REWA) by the use of a negative-refractive-index slab is explained, and, using this knowledge, it is shown that evanescent waves with specific spatial frequencies can be amplified without reflection simply by two dielectric planar waveguides. Since loss in a dielectric can be orders of magnitude lower than metals or metamaterials, our proposed scheme is the simplest way of experimentally demonstrating the intriguing phenomenon of REWA and offers simple alternatives to the use of left-handed materials, surface plasmons, or photonic crystals for near-field imaging applications.

11.2 Evanescent wave amplification

One of the most poorly understood aspects of Pendry's proposal is that at the interface of an $n = 1$ material and an $n = -1$ material, the transmission and reflection coefficients are theoretically infinite [2]. Mathematically this indicates the presence of an unstable pole on the imaginary axis in the complex transverse-spatial-frequency ($s = ik_x$) plane, and physically the transmitted and reflected evanescent optical fields must therefore increase linearly along a semi-infinite interface. This is hardly surprising if one recalls the well-known fact that infinite scattering coefficients correspond to bound-state solutions, so the incoming evanescent waves are simply resonantly coupled into the waveguide modes of the interface. The most peculiar aspect of Pendry's interface is that the scattering coefficients are always infinite, meaning that bound-state solutions exist for all k_x. This is not true for other waveguides, including photonic crystals [8], which have discrete bound states with different discrete k_x's. In particular, for ideal surface plasmons, only one bound state exists.

11.2.1 Evanescent wave amplification by one dielectric slab

First, consider a dielectric slab with thickness a and refractive index n_1 in the $x-y$ plane. Suppose that an evanescent s-polarized wave with an electric field exponentially decaying along the z axis given by $\mathbf{E}_{0+} =$

$[0,1,0]\exp(ik_z z + ik_x x - i\omega t)$ impinges on the slab, where k_x is assumed to have subwavelength resolution, so $k_x > \omega n_0/c$, k_z is determined by the dispersion relation, given by $k_z = i\sqrt{k_x^2 - k_0^2}$, $k_0 = \omega n_0/c$, and n_0 is the refractive index of the surroundings. Considering the first interface between n_0 and n_1 only, the reflected wave is $r[0,1,0]\exp(-ik_z z + ik_x x - i\omega t)$, and the transmitted wave inside the slab is $t[0,1,0]\exp(ik_z' z + ik_x x - i\omega t)$. k_x is the same on both sides of the interface, and k_z' is given by the dispersion relation $k_z' = \sqrt{k_1^2 - k_x^2}$, where $k_1 = \omega n_1/c$. k_z' is hereafter assumed to be real for waveguide modes to exist. This restricts k_x to be bounded by the wave numbers in the two media,

$$k_0 < k_x < k_1. \tag{11.1}$$

The transmission and reflection coefficients across the first interface are given by $t = 2k_z/(k_z + k_z')$ and $r = (k_z - k_z')/(k_z + k_z')$ respectively. Likewise, the scattering coefficients across the second interface are $t' = 2k_z'/(k_z' + k_z)$ and $r' = (k_z' - k_z)/(k_z' + k_z)$. To obtain the total transmission, τ, across the slab, multiple scattering events must be summed,

$$\tau = t\exp(ik_z' a)t' + t\exp(ik_z' a)[r'\exp(ik_z' a)]^2 t' + ... \tag{11.2}$$

$$= \frac{tt'\exp(ik_z' a)}{1 - r'^2\exp(2ik_z' a)}. \tag{11.3}$$

The total reflection coefficient can be obtained similarly,

$$\Gamma = r + \frac{tt'r'\exp(2ik_z' a)}{1 - r'^2\exp(2ik_z' a)}. \tag{11.4}$$

Waveguide modes correspond to those with evanescent tails exponentially decaying away from the waveguide. In other words, the total transmitted evanescent wave and the total reflected evanescent wave for the waveguide modes can exist by themselves without any incoming wave $\mathbf{E}_{0+}$, or, mathematically speaking, τ and Γ are infinity. This happens when

$$1 - r'^2\exp(2ik_z' a) = 1 - \left(\frac{k_z' - k_z}{k_z' + k_z}\right)^2 \exp(2ik_z' a) = 0, \tag{11.5}$$

which simply states that the accumulated phase in a round trip inside the waveguide must be multiples of 2π. As both k_z and k_z' depend on k_x, Eq. (11.5) is an eigenvalue equation of k_x for the TE modes of the single waveguide. A simple dielectric slab can hence achieve EWA due to the waveguide mode coupling resonances, similar to a photonic crystal [8]. If only subwavelength features are concerned and all-angle negative refraction [9] is not needed, a complicated structure such as photonic crystal is not necessary. However, just like a photonic crystal, the reflection coefficient Γ of a slab waveguide is also infinite, causing potential problems with multiple reflections.

11.2.2 Reflectionless evanescent wave amplification by two waveguides

In Pendry's proposal, both interfaces of a negative-refractive-index slab need to be considered for ideal REWA. The two interfaces can be considered as two waveguides, and the total transmission of the slab exponentially increases with respect to the thickness of the slab, or the distance between the two waveguides, when the single-interface scattering coefficients are infinite. This suggests that REWA may also exist for other kinds of double-waveguide structures, when the resonant coupling condition of the single waveguide is reached.

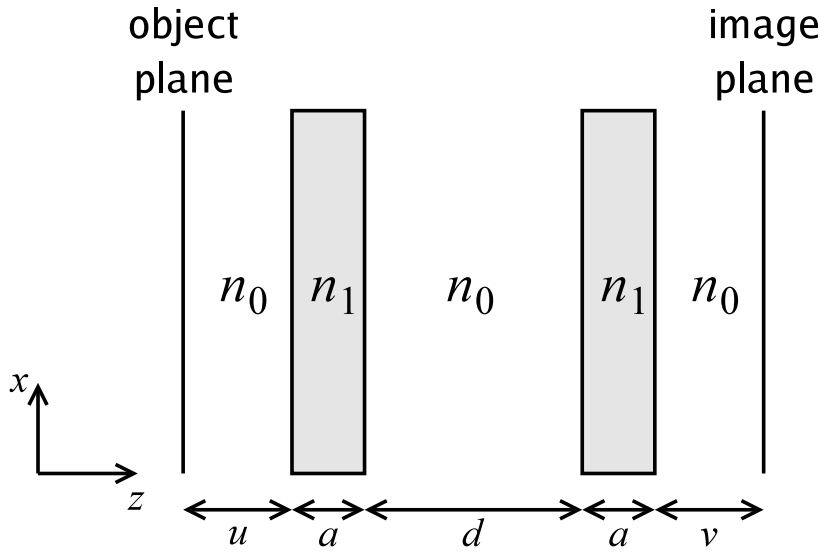

Figure 11.1: Reflectionless evanescent wave amplification (REWA) by two slab waveguides, where $n_1 > n_0$.

Now let us go back to the dielectric slab waveguide example and add another identical waveguide a distance d away from the first, as depicted in Fig. 11.1. The total transmission coefficient for this double-waveguide structure is

$$T = \frac{\tau^2 \exp(ik_z d)}{1 - \Gamma^2 \exp(2ik_z d)}. \tag{11.6}$$

When k_x coincides with one of the single-waveguide bound-state eigenvalues determined by Eq. (11.5), the total transmission becomes

$$\begin{aligned} \lim_{r'^2 \exp(2ik'_z a) \to 1} T &= \lim_{r'^2 \exp(2ik'_z a) \to 1} -\frac{\tau^2}{\Gamma^2} \exp(-ik_z d) \\ &= -\exp(-ik_z d), \end{aligned} \tag{11.7}$$

which increases exponentially with respect to d. The total reflection coefficient of the double-waveguide

structure is likewise given by

$$R = \Gamma + \frac{\tau^2 \Gamma \exp(2ik_z d)}{1 - \Gamma^2 \exp(2ik_z d)}, \tag{11.8}$$

and in the limit of k_x being a bound-state eigenvalue of a single waveguide,

$$\lim_{r'^2 \exp(2ik'_z a) \to 1} R = \lim_{r'^2 \exp(2ik'_z a) \to 1} \left(1 - \frac{\tau^2}{\Gamma^2}\right) \Gamma = 0. \tag{11.9}$$

Hence, an evanescent wave can propagate with perfect transmission and zero reflection in the setup depicted in Fig. 11.1, thereby achieving REWA, if $u + v = d$ and the resonant single-waveguide coupling condition is reached. Identical results can also be derived for p-polarized waves and TM modes. REWA should be quite general for any kind of symmetric and identical waveguides, as long as the bound-state limit of τ^2/Γ^2 is 1, so two photonic crystal slabs may be used to achieve all-angle negative refraction [9] and REWA simultaneously.

11.3 Discussion

For imaging applications, it is important to stress that the double-waveguide device only beats the resolution limit of the cladding layer with refractive index n_0, but not the resolution limit of the core layer with refractive index n_1. This is because the bound-state eigenvalues of k_x are bounded by wave numbers of the two media, as shown by Eq. (11.1). That said, for a highly multimode waveguide, the maximum k_x is close to the wave number of the core medium, so the proposed device can still take advantage of the high resolution limit offered by a high-refractive-index material without contact with the object. This can be advantageous for many applications because many solids have higher refractive indices than fluids but it is not very practical to fill the whole imaging system with solids as in oil immersion microscopy. Furthermore, for biomedical imaging applications, it is not always possible to place the high-refractive-index material directly in touch with the object plane, because the contact may damage the biological sample, or one may desire to put the object plane inside a semi-transparent object, such as a cell.

Promising high-refractive-index material candidates include diamond, which can have a refractive index as high as 2.7 [10] and transparent down to a wavelength of about 230 nm [11], and coherently prepared atoms (confined in, say, a dielectric box) with a resonantly enhanced refractive index [12], which can theoretically reach the order of one hundred [13] and a proof-of-concept experiment of which has already been demonstrated [14].

An outstanding problem of using any waveguide, except negative-refractive-index slabs, for EWA is that ideal enhancement only occurs for single-waveguide modes, which are discrete and band-limited for each ω. For instance, the discrete k_x's of the TE modes in a symmetric slab waveguide are determined by Eq. (11.5) and band-limited by Eq. (11.1). As a result, an object with frequency components that lie outside the waveguiding band or do not coincide with the bound states cannot be perfectly reproduced. For this

reason, ideal surface plasmons are ill-suited for faithful image transmission, as they have only one bound state with one eigenvalue k_x. Loss can increase the bandwidth of the transmitted spatial frequencies near each discrete waveguide mode, but also severely limits the distance between the two waveguides at which effective REWA occurs. For dielectrics, multimode waveguides can partially solve this problem by offering more Fourier modes within the band. One may also use a broadband light source to increase the amount of available spatial frequencies.

11.4 Conclusion

In conclusion, the use of two dielectric planar waveguides is proposed to amplify evanescent waves without reflection. The simple configuration elucidates the most essential physics of REWA and presents a simple way of experimentally demonstrating such an intriguing phenomenon. In practice, the proposed setup also allows one to take advantage of high resolution limit of a dielectric without contact with the object.

Bibliography

[1] E. Betzig and J. K. Trautman, Science **257**, 189 (1992).

[2] J. B. Pendry, Phys. Rev. Lett. **85**, 3966 (2000).

[3] See, for example, N. Garcia and M. Nieto-Vesperinas, Phys. Rev. Lett. **88**, 207403 (2002).

[4] S. Zhang, W. Fan, B. K. Minhas, A. Frauenglass, K. J. Malloy, and S. R. J. Brueck, Phys. Rev. Lett. **94**, 037402 (2005).

[5] S. Zhang, W. Fan, N. C. Panoiu, K. J. Malloy, R. M. Osgood, and S. R. J. Brueck, Phys. Rev. Lett. **95**, 137404 (2005).

[6] V. M. Shalaev, W. Cai, U. K. Chettiar, H.-K. Yuan, A. K. Sarychev, V. P. Drachev, and A. V. Kildishev, Opt. Lett. **30**, 3356 (2005).

[7] N. Fang, H. Lee, C. Sun, and X. Zhang, Science **308**, 534 (2005).

[8] C. Luo, S. G. Johnson, J. D. Joannopoulos, and J. B. Pendry, Phys. Rev. B **68**, 045115 (2003).

[9] C. Luo, S. G. Johnson, J. D. Joannopoulos, and J. B. Pendry, Phys. Rev. B **65**, 201104 (2002).

[10] D. F. Edwards and E. Ochoa, J. Opt. Soc. Am. **71**, 607 (1981), and references therein.

[11] C. D. Clark, P. J. Dean, and P. V. Harris, Proc. Roy. Soc. A **277**, 312 (1964).

[12] M. O. Scully, Phys. Rev. Lett. **67**, 1855 (1991).

[13] M. Fleischhauer, C. H. Keitel, M. O. Scully, C. Su, B. T. Ulrich, and S.-Y. Zhu, Phys. Rev. A **46**, 1468 (1992).

[14] A. S. Zibrov, M. D. Lukin, L. Hollberg, D. E. Nikonov, M. O. Scully, H. G. Robinson, and V. L. Velichansky, Phys. Rev. Lett. **76**, 3935 (1996).

Chapter 12

Metaphoric optical computing of fluid dynamics

12.1 Introduction

12.1.1 Philosophy of metaphoric computing

Nonlinear dynamical systems, such as weather, plasma, and the economy, are ubiquitous in nature and everyday life, yet such systems are typified by their highly complex and chaotic behaviors, making them notoriously difficult to study theoretically, experimentally, and numerically. Analytic solutions of nonlinear systems are rare, experiments are often too inflexible or impractical, and numerical simulations must take into account a large number of data points in multiple dimensions in order to accurately model a problem of interest, such that even the fastest supercomputers today would take days or weeks to simulate relatively simple nonlinear dynamics that a physical system exhibits in seconds.

On the opposite side of the same coin, we can regard the physical system as a computational device that computes its own dynamics at a speed unimaginable by supercomputers. The key to harnessing this tremendous computing power of a physical system is therefore to make it compute other interesting problems of the same order of complexity. Of course, a conventional digital computer is itself a physical system, but it makes use of complex semiconductor physics to compute elementary logic operations, and in doing so, discards a large amount of information that is considered extraneous. In this perspective, a digital computer is an extremely inefficient computing device, as it only utilizes an exceedingly small amount of the full computing capability potentially offered by its physics. The advantage in this case is the flexibility in cascading different logic operations for general-purpose computing, but as evidenced by the difficulties in the numerical simulations of nonlinear dynamical systems, this inefficient computing method is often inadequate.

In order to make full use of the computing capability offered by a physical system, we hereby propose the concept of metaphoric computing, which makes use of a more experimentally accessible nonlinear dynamical system to simulate another nonlinear dynamical system. An example of this computing method is a wind

tunnel, in which a small-scale fluid experiment is performed to simulate large-scale fluid dynamics, by virtue of the scaling laws inherent in fluid dynamics. Metaphoric computing, however, is not restricted to the use of similar physical systems to simulate each other. In this paper, we show in particular that nonlinear optics can compute fluid dynamics as well. An optical beam inherently holds three-dimensional spatiotemporal information, and nonlinear optical propagation computes the evolution of this large amount of information simultaneously at the speed of light, promising substantial parallelism and speed for computing. Although the use of nonlinear optics for digital computing has not been as successful as the use of solid-state electronics, forcing optical beams to compute binary logic wastes most of the spatiotemporal information that can be manipulated in optical beams. Instead of fitting a square peg in a round hole, using optics to simulate other nonlinear dynamical systems provides a natural way of making full use of the computing capacity offered by a nonlinear optical system.

Fluid dynamics, the foundation of a wide variety of important research fields including meteorology, aeronautics, plasma physics, superfluids, and Bose-Einstein condensates, is an ideal problem to solve by metaphoric computing. Intractable theoretical analysis and inflexible experiments compel the use of numerical simulations, the difficulty of which nonetheless gives rise to a whole new field, computational fluid dynamics, in itself. The main difficulty is due to the inherent complexity of a fluid dynamics problem, which is nonlinear and continuously generates finer structures as the fluid dynamics evolves. For problems that are of practical interest, such fine structures are often orders of magnitude smaller than the size of the objects under consideration, thus requiring a large number of data points in each of the three spatial dimensions to be manipulated at each time step, which must also be correspondingly small to avoid numerical instabilities. An alternative method of simulating complex fluid dynamics that combines the speed of a fluid experiment and the flexibility of a numerical analysis is hence of great practical importance. In this paper, we show that, via a suitable transformation, nonlinear optical propagation can be utilized to simulate Euler fluid dynamics, which is known to be computationally expensive and unstable to solve numerically . We also provide strong evidence that nonlinear optics can simulate high-Reynolds-number Navier-Stokes fluid dynamics as well, which include a large class of important and computationally difficult problems, such as turbulence. With the speed, parallelism, and configurability of optics, an “optical wind tunnel” may one day become a viable alternative to experiments and numerical analysis in the study of fluid dynamics.

12.1.2 Correspondence between nonlinear optics and fluid dynamics

The analogy between nonlinear optics and fluid dynamics has been noted by many authors [1, 2, 3, 4, 5, 6, 7, 8, 9, 10, 11, 12, 13, 14, 15, 16, 17, 18]. Wagner *et al.* first suggested that the nonlinear propagation equation of an optical beam can be recast into equations that resemble the continuity equation and the Bernoulli equation in irrotational fluid dynamics [1]. Coullet *et al.* first coined the term “optical vortices,” which shows the analogy between phase singularities in optics and fluid vortices [2]. Brambilla *et al.* noted that laser equations can be transformed to a hydrodynamic form [3]. Arecchi *et al.* first experimentally demonstrated the dynamics

of optical vortices in nonlinear optics [4]. Akhmanov *et al.* called the rich nonlinear dynamics observed in a nonlinear resonator "optical turbulence." [5] Swartzlander and Law observed optical vortex solitons created via the instability of dark soliton stripes analogous to the Kelvin-Helmholtz instability in fluid dynamics [6]. Staliunas showed that a laser can be described by the Ginzburg-Landau equation, which can be transformed into equations resembling the Navier-Stokes equations that describe viscous fluid dynamics [7]. Vaupel *et al.* observed vortex pair nucleation by the interference of two modes in a laser and claimed that it was an analogue of a vortex street behind an obstacle in a fluid flow [8]. Molina-Terriza *et al.* also observed optical vortex streets in walking second-harmonic generation [9]. Roux [10] and Rozas *et al.* [11] studied the interactions between optical vortices and found that their interactions resemble those of fluid vortices. Rozas *et al.* then experimentally demonstrated the fluidlike motion of a pair of optical vortices [12]. Michinel *et al.* [13] and Paz-Alonso *et al.* [14] found that optical propagation in a cubic-quintic nonlinear medium resembles a liquid drop, and optical vortices in such a medium also have fluidlike motions [15]. On the other hand, nonlinear optics has been compared with superfluids and Bose-Einistein condensates, as they can all be described, to varying degrees, by the nonlinear Schrödinger equation [19, 20], commonly known as the Gross-Pitaevskii equation in the field of superfluids [21]. Pomeau and Rica suggested that the phenomenon of transition to dissipation in a superflow [22] can be observed in nonlinear diffraction [16]. Bolda *et al.* numerically demonstrated the same phenomenon in a nonlinear Fabry-Pérot cavity [17]. Chiao also found that photons in such a cavity should obey the Bogoliubov dispersion relation for a superfluid [18].

The abundant amount of prior work credited above provides ample evidence that nonlinear optics resembles fluid dynamics to a certain degree. In order to use nonlinear optics as a useful and practical computational tool for fluid dynamics, however, simply drawing analogies between the two kinds of dynamics is not enough. One must be able to show an exact correspondence or, at the very least, an approaching convergence between a problem in nonlinear optics and a problem in fluid dynamics, in order to produce any useful prediction of fluid dynamics via nonlinear optics. Moreover, as computers nowadays have enough capabilities to simulate two-dimensional fluids, the mere correspondence between optics and two-dimensional fluid dynamics considered in most of the prior work would not motivate the use of metaphoric optical computing in preference to conventional digital computing. A three-dimensional fluid modeling, on the other hand, requires a processing capability orders of magnitude higher than that available in today's supercomputers, so metaphoric optical computing would need to compute such problems much more efficiently to compete with electronic computers and the Moore's law.

In the following sections, we shall attempt to establish the correspondence between nonlinear optics and three-dimensional fluid dynamics. We shall show that, taking group-velocity dispersion into account, nonlinear optical dynamics approaches three-dimensional inviscid Euler fluid dynamics in the highly nonlinear self-defocusing regime, where the optical intensity represents the fluid density, the optical phase gradient represents the fluid velocity, the nonlinear refractive index perturbation represents pressure, the propagation distance represents time, and the temporal dimension of the optical pulse represents the third dimension of

the fluid. As Euler fluid equations often exhibit high numerical instabilities, this correspondence in itself should be useful in modeling high-Reynolds-number fluid dynamics away from objects and boundaries. In the convergence of nonlinear Schrödinger equation towards the Euler equations, a "quantum pressure" term arising from the nonlinear Schrödinger equation plays the role of a small parameter. As this quantum pressure term plays analogous roles to viscosity in the Navier-Stokes equations, we argue that nonlinear optics should be able to approximate viscous Navier-Stokes fluid dynamics as well, in the regime where quantum pressure and viscosity both play the role of small parameters in the respective equations. That said, we do not pretend that we have established the equivalence between nonlinear optics and Navier-Stokes dynamics, as the similarity between quantum pressure and viscosity is still an open problem.

On the practical side, in cases where an ideal nonlinear optics setup is not available, we suggest a split-step method that pieces together different optical devices to approximate an ideal nonlinear optics experiment. This method is very similar to the method proposed to simulate quantum systems using a quantum computer [23].

It must be stressed that although we focus on simulations of classical physical systems, future quantum computers that simulate quantum systems [23] would run into the same problem of manipulating a large amount of multidimensional information. In the case of quantum systems, multidimensional quantum information, such as a multiparticle multispatiotemporal-dimensional wavefunction, needs to be processed in parallel. Quantum computers can naturally parallelize the multiparticle aspect, but there is no obvious way of parallelizing the manipulation of multispatiotemporal-dimensional information via simple binary quantum logic. Perhaps a quantum metaphoric computing would then be necessary, where a more accessible multidimensional quantum system is used to simulate another quantum system.

12.2 Correspondence between nonlinear optics and Euler fluid dynamics

12.2.1 Madelung transformation

We now proceed to show mathematically how the self-defocusing nonlinear optical propagation equation, including the effect of group-velocity dispersion, can be transformed to three-dimensional hydrodynamic equations. First, we show how the optics equations, in the absence of optical vortices, correspond to inviscid and irrotational fluid equations. This form of transformation is widely attributed to Madelung [24]. We model the paraxial nonlinear propagation of an optical beam, described by the envelope function $\psi(z,x,y,T)$, via the nonlinear Schrödinger equation [19, 20],

$$i\frac{\partial\psi}{\partial z} = -\frac{1}{2k_0}\left(\frac{\partial^2}{\partial x^2}+\frac{\partial^2}{\partial y^2}\right)\psi + \frac{\beta_2}{2}\frac{\partial^2\psi}{\partial T^2} - k_0 n_2|\psi|^2\psi, \tag{12.1}$$

where z is the propagation distance, $k_0 = 2\pi n_0/\lambda_0$ is the carrier wave number, β_2 is the group-velocity dispersion coefficient, T is the time coordinate in the moving frame of the pulse, and n_2 is the nonlinear Kerr coefficient. To use the time coordinate as the third spatial dimension of a fluid, anomalous group-velocity dispersion, or $\beta_2 < 0$, is required. Dispersion can then be regarded in equal footing as diffraction if a normalized time coordinate is defined as

$$\tau \equiv \frac{T}{\sqrt{-\beta_2 n_0 k_0}}, \tag{12.2}$$

such that

$$i\frac{\partial \psi}{\partial z} = -\frac{1}{2k_0}\left(\frac{\partial^2}{\partial x^2} + \frac{\partial^2}{\partial y^2} + \frac{\partial^2}{\partial \tau^2}\right)\psi - k_0 n_2 |\psi|^2 \psi. \tag{12.3}$$

The Madelung transformation is defined as follows,

$$\psi = |\psi| \exp(j\phi), \tag{12.4}$$

$$I = |\psi|^2, \tag{12.5}$$

$$\mathbf{k} = \nabla'\phi = \hat{x}\frac{\partial}{\partial x} + \hat{y}\frac{\partial}{\partial y} + \hat{\tau}\frac{\partial}{\partial \tau}, \tag{12.6}$$

such that the evolution equations for the intensity, I, and the phase gradient, $\mathbf{k}$, are given by

$$\frac{\partial I}{\partial z} + \frac{1}{k_0}\nabla' \cdot (I\mathbf{k}) = 0, \tag{12.7}$$

$$\frac{\partial \mathbf{k}}{\partial z} + \frac{1}{k_0}\nabla'\left(\frac{1}{2}\mathbf{k}\cdot\mathbf{k}\right) = \nabla'(k_0 n_2 I) + \frac{1}{k_0}\nabla'\left(\frac{1}{2\sqrt{I}}\nabla'^2\sqrt{I}\right). \tag{12.8}$$

One can already see that Eq. (12.7) has the exact same form as the fluid continuity equation, while Eq. (12.8) resembles the Bernoulli equation [1], if one regards the intensity as the fluid density and the phase gradient as the fluid velocity. The nonlinear refractive index term, $k_0 n_2 I$, would resemble the fluid pressure if $n_2 < 0$, so self-defocusing is required. The last term in Eq. (12.8) is a peculiar term that arises from optical diffraction and dispersion, does not exist in classical fluid dynamics, and is commonly called the "quantum pressure."

In order to compare these equations with fluid equations more easily, we use the following normalized variables,

$$\nabla = W\nabla', \quad \zeta = \frac{K}{Wk_0}z, \tag{12.9}$$

$$\rho = \frac{I}{I_0}, \quad \mathbf{u} = \frac{\mathbf{k}}{K} = \frac{1}{KW}\nabla\phi, \tag{12.10}$$

$$a = \frac{1}{k_0\sqrt{-n_2 I_0}}, \quad \mathscr{M} = Ka, \quad \mathscr{R} = KW, \tag{12.11}$$

where W is the characteristic size, K is the characteristic phase gradient, I_0 is some characteristic optical

intensity of the propagation, and a is the so-called healing length, which is the length scale at which the quantum pressure term has the same order of magnitude as the nonlinear term on the right hand side of Eq. (12.8), $\mathscr{M}$ is the Mach number, which measures the relative strength of fluid pressure compared with convection, and $\mathscr{R}$ is another number that measures the relative strength of fluid convection compared with quantum pressure. The normalized equations become

$$\frac{\partial \rho}{\partial \zeta} + \nabla \cdot (\rho \mathbf{u}) = 0, \tag{12.12}$$

$$\frac{\partial \mathbf{u}}{\partial \zeta} + \nabla \left(\frac{1}{2} \mathbf{u} \cdot \mathbf{u} \right) = -\frac{1}{\mathscr{M}^2 \rho} \nabla \left(\frac{1}{2} \rho^2 \right) - \frac{1}{\mathscr{R}^2} \nabla \left(\frac{1}{2\sqrt{\rho}} \nabla^2 \sqrt{\rho} \right). \tag{12.13}$$

Equation (12.12) is exactly the same as the fluid continuity equation, and in the limit of $\mathscr{M}/\mathscr{R} \to 0$, which is the highly self-defocusing regime, Eq. (12.13) is the same as the hydrodynamic equation of motion that describes inviscid and irrotational fluids. Equations (12.12) and (12.13) also admit sound wave solutions, which describe travelling perturbations to the density and the velocity. As long as the sound waves are weak, the dependence of pressure on the density is not crucial, and the use of self-defocusing Kerr nonlinearity is adequate. This restricts the correspondence to slightly compressible barotropic fluids.

In order to model slightly compressible fluids, the optical beam needs to have a relatively constant intensity background. This can be achieved approximately near the center of a very large beam, in a large multimode waveguide as a container in two spatial dimensions, or in a cubic-quintic nonlinear medium to provide a "surface tension" to the beam [25, 13, 14, 15].

12.2.2 Vorticity

In general, the fluid velocity vector should contain an irrotational component and a rotational component,

$$\mathbf{u} = -\nabla \varphi - \nabla \times \mathbf{A}, \tag{12.14}$$

where φ is called the velocity potential, and the curl of $\mathbf{u}$ is defined as the fluid vorticity,

$$\boldsymbol{\omega} = \nabla \times \mathbf{u} = -\nabla \times (\nabla \times \mathbf{A}). \tag{12.15}$$

The dynamics of vorticity is arguably the cornerstone of hydrodynamics [21]. The inviscid fluid dynamics that includes the rotational effect is governed by the Euler equation,

$$\frac{\partial \mathbf{u}}{\partial \zeta} + \mathbf{u} \cdot \nabla \mathbf{u} = -\frac{1}{\mathscr{M}^2 \rho} \nabla P, \tag{12.16}$$

where P is the pressure. For incompressible fluids, $\mathscr{M} << 1$, and as long as P increases with ρ, the specific dependence of P on the fluid properties is not important. Equation (12.16) contains the convective term $\mathbf{u} \cdot \nabla \mathbf{u}$,

which can be written as

$$\mathbf{u}\cdot\nabla\mathbf{u} = \nabla\left(\frac{1}{2}\mathbf{u}\cdot\mathbf{u}\right) + (\nabla\times\mathbf{u})\times\mathbf{u} \tag{12.17}$$

$$= \nabla\left(\frac{1}{2}\mathbf{u}\cdot\mathbf{u}\right) + \boldsymbol{\omega}\times\mathbf{u}. \tag{12.18}$$

One can then see that the optical Bernoulli equation, Eq. (12.13), misses the rotational component of the convective term. In other words, the Madelung transformation is only able to describe the irrotational part of the fluid motion, but not the more important rotational part.

The inability of the Madelung transformation to describe vorticity is due to the failure of the transformation near optical vortices, where Eq. (12.13) is ill-defined. To understand this problem, consider a rectilinear optical vortex in polar coordinates and neglect the third fluid dimension for now,

$$\psi = f(r)\exp(im\theta), \tag{12.19}$$

$$r = \sqrt{x^2+y^2}, \quad \theta = \tan^{-1}\left(\frac{y}{x}\right), \tag{12.20}$$

where m is an integer and is called the topological charge of an optical vortex. The phase gradient is then given by

$$\mathbf{k} = \hat{\theta}\frac{1}{r}\frac{\partial}{\partial\theta}(m\theta) = \hat{\theta}\frac{m}{r}. \tag{12.21}$$

The fluid vorticity is proportional to the curl of $\mathbf{k}$,

$$\nabla\times\mathbf{k} = \hat{z}\frac{2\pi m}{r}\delta(r), \tag{12.22}$$

which resembles the vorticity of an ideal point fluid vortex [26]. The motion of these vortices, however, cannot be described by the Madelung transformed equations due to two problems: $\mathbf{k}$ diverges when $r\to 0$, so the fluid velocity $\mathbf{u}$ at the center of a vortex is infinite, and $f(r)$ must approach r^m in the limit of $r\to 0$ to maintain the continuity of ψ, so the quantum pressure term, with $\sqrt{\rho}$ in the denominator, is also infinite near the vortex center.

To overcome these difficulties, it is necessary to consider the motion of the optical vortices separate from the irrotational optical flow.

12.2.3 Optical vortex solitons and point vortices

In a relatively constant intensity background, optical vortices exist as optical vortex solitons [27, 6, 25]. The optical envelope function ψ of a vortex soliton is given by Eq. (12.19), where $f(r)\to r^m$ for $r << a$, and $f(r)$ approaches a constant for $r >> a$, where a is the healing length and also the size of the dark spot of a

vortex soliton. In three dimensions, a vortex soliton exists as a vortex filament. We shall hereafter consider single-charged vortex solitons with $m = \pm 1$ only, as they have the lowest energy and are the most prevalent ones arising from an experimental situation. It is also more accurate to approximate continuous vorticity with only discrete vortices with the smallest topological charge.

Eq. (12.22) suggests that an optical vortex soliton resembles an ideal point vortex in incompressible fluids. Indeed, the motion of optical vortices in the highly self-defocusing limit can be rigorously proven to behave in the same way as point fluid vortices [10, 11, 28, 29, 30, 31]. If one defines the position of each vortex filament as $\mathbf{x}_j$, then the fluid velocity at each point due to the presence of the vortex filaments in the limit of high self-defocusing is given by

$$\mathbf{u}(\mathbf{x},\zeta) = -\sum_j 2\pi m_j \int \frac{(\mathbf{x}-\mathbf{x}_j)\times d\mathbf{x}_j}{4\pi|\mathbf{x}-\mathbf{x}_j|^3} - \nabla\varphi, \quad a \to 0, \tag{12.23}$$

where $\mathbf{x}$ is the normalized three-dimensional position vector, m_j is the topological charge of vortex j, and $-\nabla\varphi$ describes the irrotational flow according to Eq. (12.13). In particular, the motion of each filament is given by

$$\frac{\partial \mathbf{x}_i}{\partial \zeta} = -\sum_j 2\pi m_j \int \frac{(\mathbf{x}_i-\mathbf{x}_j)\times d\mathbf{x}_j}{4\pi|\mathbf{x}_i-\mathbf{x}_j|^3} - \nabla\varphi, \quad a \to 0, \tag{12.24}$$

in the leading order. These equations of vortex motion are valid as long as the separations of the vortices are much larger than a. For example, Fig. 12.1 plots the intensity, phase, and phase gradient of two rectilinear optical vortex solitons with the same charge, which should rotate around each other, and those of two vortices with opposite charges, which should drift in the same direction perpendicular to their separation.

With the vortex filaments, one can define the equivalent vorticity in an optical beam,

$$\boldsymbol{\omega}(\mathbf{x},\zeta) = \sum_j 2\pi m_j \int d\mathbf{x}_j \delta(\mathbf{x}-\mathbf{x}_j), \tag{12.25}$$

which can be used to approximate the continuous vorticity of a fluid, if the number of vortex filaments is large enough. In this case, to include the vorticity effect in the nonlinear optical dynamics, one can phenomenologically patch up the irrotational equation of motion, Eq. (12.13),

$$\frac{\partial \mathbf{u}}{\partial \zeta} + \nabla\left(\frac{1}{2}\mathbf{u}\cdot\mathbf{u}\right) + \boldsymbol{\omega}\times\mathbf{u} = -\frac{1}{\mathscr{M}^2}\nabla\rho. \tag{12.26}$$

This modification of the equation of motion can be attributed to the phenomenon of phase slippage [21, 32], well known in the field of superfluids. The use of discrete point vortex interactions to calculate Euler fluid dynamics is also a well-known numerical method in computational fluid dynamics [33]. Hence, to simulate Euler fluid dynamics, one can approximate both the rotational and irrotational components of the initial fluid velocity profile by the optical phase and the phase singularities in an optical beam, and the

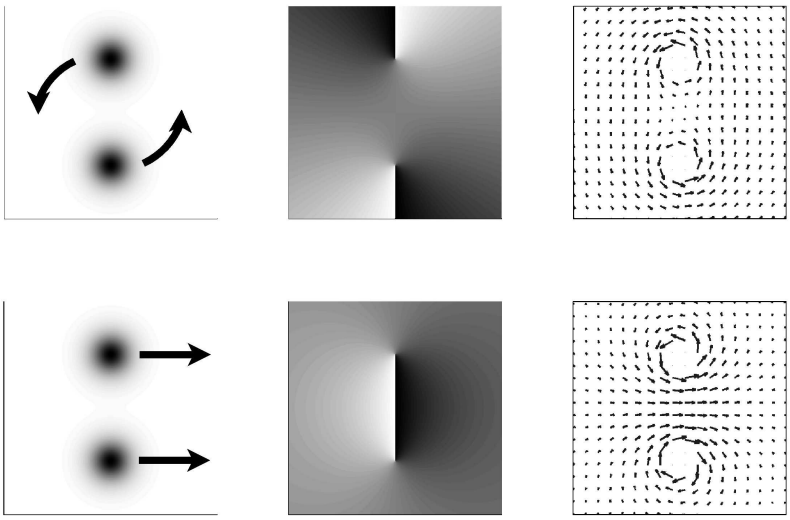

Figure 12.1: Intensity (left column), phase (middle column), and phase gradient (right column) of two optical vortex solitons with the same charge (top row), which should rotate in the same sense, and those of two vortex solitons with opposite charges, which should drift in a direction perpendicular to their separation. The phase gradient near the centers of the vortices is not plotted due to its divergence.

nonlinear self-defocusing propagation of the beam would converge to incompressible Euler fluid dynamics in the strongly self-defocusing regime. One can also borrow from the well-established numerical techniques [33] to determine how the distribution of optical vortices sufficiently approximates the continuous vorticity in fluids.

12.2.4 The fluid flux representation

So far, we have shown that optical vortex solitons behave like point vortices in fluids when they are far away from each other, and this behavior can be used to approximate Euler fluid dynamics. However, there is no guarantee that the vortices would remain well separated in the course of the vortex dynamics. If optical vortices behaved exactly like point vortices, then their velocities would diverge when they are close to each other. This velocity divergence is well known to cause significant numerical instability in the use of point vortices for computational fluid dynamics [33]. Another problem is that in three dimensions, the self-induced velocity of a curved point vortex filament diverges logarithmically $\sim \ln(1/a)$ in the limit of $a \to 0$ [33]. Since the optical intensity decreases to zero near the center of an optical vortex, the quantum pressure term, which determines the size of the vortex dark spot, can no longer be ignored, and the optical vortex interactions should differ markedly from point vortex interactions when their separation is on the order of a.

To investigate the optical vortex dynamics when they are close to each other, the fluid velocity is no longer an appropriate quantity to study, because it diverges near a vortex center. The density, on the other hand, approaches zero towards the center. This motivates us to define an alternative finite quantity by multiplying

the velocity and the density,

$$\mathbf{J} \equiv \rho \mathbf{u}. \tag{12.27}$$

which is the fluid flux, or the momentum density. Simple calculations show that the flux is indeed finite everywhere in an optical beam, including the center of an optical vortex. In terms of the flux, the tensor dynamical equations now read [34]

$$\frac{\partial \rho}{\partial \zeta} + \frac{\partial J_i}{\partial x_i} = 0, \tag{12.28}$$

$$\frac{\partial J_i}{\partial \zeta} + \frac{\partial}{\partial x_j}\left(\frac{J_i J_j}{\rho}\right) = -\frac{1}{\mathscr{M}^2}\frac{\partial}{\partial x_i}\left(\frac{1}{2}\rho^2\right) - \frac{1}{\mathscr{R}^2}\frac{\partial}{\partial x_j}\frac{1}{2}\left(\frac{\partial\sqrt{\rho}}{\partial x_i}\frac{\partial\sqrt{\rho}}{\partial x_j} - \sqrt{\rho}\frac{\partial^2\sqrt{\rho}}{\partial x_i \partial x_j}\right), \tag{12.29}$$

where J_i is the ith component of $\mathbf{J}$, $\partial/\partial x_i$ is the ith spatial derivative, and repeated indices are implicitly summed in the manner of Einstein's summation. These equations have the same form as the normalized Euler equations in the tensor form,

$$\frac{\partial \rho}{\partial \zeta} + \frac{\partial J_i}{\partial x_i} = 0, \tag{12.30}$$

$$\frac{\partial J_i}{\partial \zeta} + \frac{\partial}{\partial x_j}\left(\frac{J_i J_j}{\rho}\right) = -\frac{1}{\mathscr{M}^2}\frac{\partial P}{\partial x_i}, \tag{12.31}$$

except the quantum pressure term in Eq. (12.29). Hence, in the flux representation, we have successfully avoided the problem of divergent quantities. Furthermore, Eq. (12.29), in contrast to Eq. (12.13), includes the correct convective term.

The use of momentum density in the description of nonlinear optical dynamics is more natural and appropriate than the use of velocity in the Madelung transformation, as the dynamics ultimately evolves according to the basic law of momentum conservation. As we shall show next, when comparing the optical flux to the fluid flux, the dynamics of optical vortex solitons are much more similar to that of less singular fluid vortices than point vortices, and the correspondence between nonlinear optics and Euler fluid dynamics is still justified when a is finite.

12.2.5 Optical vortex solitons and vortex blobs

In light of the fluid flux representation, one should therefore compare the flux of an optical vortex soliton to the flux of a fluid vortex. In an incompressible fluid, the density is constant, so the flux is proportional to the velocity, and the flux at the center of a point vortex has the same singular behavior as the velocity. Near a vortex soliton, however, the flux is finite. Consider the example of a single-charged vortex soliton. The flux

near the center is given by

$$\mathbf{J} \propto \hat{\theta} r, \quad r << a, \tag{12.32}$$

which vanishes as $r \to 0$, as opposed to the divergence of $\mathbf{J} \sim 1/r$ at the center of a point vortex.

Instead of comparing a vortex soliton to a point vortex, one should hence compare the soliton to a *vortex blob* [33], which has finite vorticity over a finite area. The vorticity of a vortex blob filament is mathematically described by

$$\boldsymbol{\omega}(\mathbf{x}, \zeta) = 2\pi m_j \int d\mathbf{x}_j \gamma(|\mathbf{x} - \mathbf{x}_j|), \tag{12.33}$$

where γ is a vorticity distribution function for the filament. The velocity near the center of a rectilinear vortex blob and far away from the center is

$$\mathbf{u} \propto \hat{\theta} r, \quad r << a, \tag{12.34}$$

$$\mathbf{u} \propto \hat{\theta} \frac{1}{r}, \quad r >> a, \tag{12.35}$$

so in an incompressible fluid, the fluid flux of an optical vortex soliton with size a is the same as that of a vortex blob with size a. See Fig. 12.2 for a graphical illustration. The dynamics of a vortex blob and that

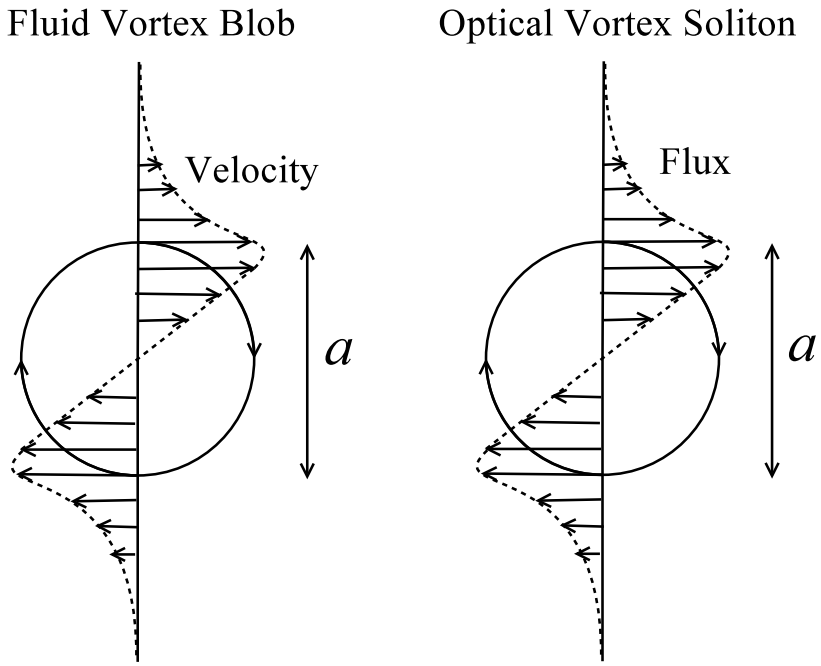

Figure 12.2: Sketches of velocity and flux of a vortex blob and an optical vortex along a line across the center, to illustrate the similarities between the two in terms of the flux.

of a vortex soliton are also extremely similar. For example, the rotation frequency Ω of two like-charged

vortex blobs approaches a constant $\propto 1/a^2$ when their separation goes to zero. Numerical simulations of the nonlinear Schrödinger equation also show that the rotation frequency of two like-charged vortex solitons approaches a constant $\propto 1/a^2$ and does not diverge like two point vortices [35]. On the other hand, the self-induced velocity of a curved vortex blob filament is given by [33]

$$\frac{\partial \mathbf{x}_i}{\partial \zeta} = \frac{m_i \mathbf{b}}{2\rho_c} \ln \frac{\rho_c}{a}, \tag{12.36}$$

where $\mathbf{b}$ is the unit binomial vector of the filament and ρ_c is the radius of curvature. The self-induced velocity of an optical vortex soliton filament is proven to be exactly the same [29]. Hence, optical vortex solitons act as vortex blobs, and a large number of solitons can simulate Euler fluid dynamics, much like the popular discrete vortex blob method in computational fluid dynamics [33].

12.2.6 Numerical evidence of correspondence between nonlinear optics and Euler fluid dynamics

The most telling evidence of the correspondence between nonlinear optics and Euler fluid dynamics is perhaps the numerical fluid dynamics simulations using the nonlinear Schrödinger equation by Nore *et al.* [36, 37]. Using the nonlinear Schrödinger equation, Nore *et al.* numerically demonstrated the Euler fluid dynamics of a jet made of an array of counterrotating vortices, which exhibit sinuous and varicose instabilities [36]. In another study, Nore *et al.* also demonstrated three-dimensional shear flows and showed that numerically solving nonlinear Schrödinger equation is a viable alternative to Euler and Navier-Stokes equations for the numerical study of shear flows [37]. As nonlinear optical propagation is governed by nonlinear Schrödinger equation, the numerical experiments by Nore *et al.* show that nonlinear optics should also be able to compute Euler fluid dynamics.

12.3 Similarities between nonlinear Schrödinger dynamics and Navier-Stokes fluid dynamics

In the previous sections, we have shown the correspondence between self-defocusing optical propagation and inviscid Euler fluid dynamics via a variety of methods, including the Madelung transformation, the incorporation of vorticity effect due to the "phase slip" phenomenon, the fluid flux representation, and the comparison between optical vortex solitons and vortex blobs. Even though viscosity plays the role of a small parameter in most interesting fluid dynamics problems, its effects are of paramount importance near a "no-slip" boundary and in the dissipation of eddies, in which cases the viscous Navier-Stokes equations should be used. In this section we shall present evidence that the nonlinear Schrödinger equation exhibits many of the same behaviors of viscous Navier-Stokes fluid dynamics, and in each case, quantum pressure plays an

analogous role to viscosity.

The normalized Navier-Stokes equations in the flux representation are given by

$$\frac{\partial \rho}{\partial \zeta} + \frac{\partial J_i}{\partial x_i} = 0, \tag{12.37}$$

$$\frac{\partial J_i}{\partial \zeta} + \frac{\partial}{\partial x_j}\left(\frac{J_i J_j}{\rho}\right) = -\frac{1}{\mathscr{M}^2}\frac{\partial P}{\partial x_i} + \frac{1}{\mathscr{R}}\frac{\partial}{\partial x_j}\left(\frac{\partial u_i}{\partial x_j} + \frac{\partial u_j}{\partial x_i}\right), \tag{12.38}$$

where the last term in Eq. (12.38) is the viscosity term and $\mathscr{R}$ is called the Reynolds number, which describes the relative strength of convection compared to viscosity,

$$\mathscr{R} = \frac{UL}{\nu}, \tag{12.39}$$

where U is the characteristic velocity of the fluid system, L is the characteristic length, and ν is the kinematic viscosity of the fluid. Comparing the viscosity term in Eq. (12.38) with the quantum pressure term in Eq. (12.29) via a dimensional analysis would suggest that an analogous optical Reynolds number would be defined as

$$\mathscr{R} = KW, \tag{12.40}$$

where, to recall, K is the characteristic optical phase gradient, and W is the characteristic size of the optical experiment setup. The optical Reynolds number thus roughly measures the number of optical vortices. In other words, if the optical Reynolds number indeed corresponds to its fluid counterpart, then the quantization of the optical vortices would play an analogous role to fluid viscosity. This view seems to be echoed by other researchers in the field of superfluids [38, 39, 40, 41], although we must stress that it is still an open problem as to what extent the quantization effect resembles the viscous effect [41].

12.3.1 Zero-flux boundary conditions, boundary layers, and boundary layer separation

In classical fluid dynamics the "no-slip" boundary condition is most commonly used, and restricts the total velocity and hence the total flux to be zero at the boundary. For fluid flow above a surface, the velocity shear introduced must be balanced by a viscous stress, resulting in a boundary layer that connects the zero velocity at the boundary to the flow velocity above the boundary in an asymptotic expansion [42]. For the nonlinear Schrödinger equation, the boundary condition of an impenetrable object can be specified by a low-refractive-index region, which restricts the optical intensity to be zero at the surface [43] due to total internal reflection. Even though the tangential velocity can have a nonzero value at the surface, both the normal and tangential components of the flux must be zero there. This can hence be viewed as a zero-flux "no-slip" boundary condition. An optical boundary layer analogous to the viscous boundary layer in classical fluid dynamics is

also formed [43]. See Fig. 12.3 for a graphical illustration of the similarities between a viscous boundary layer and an optical boundary layer.

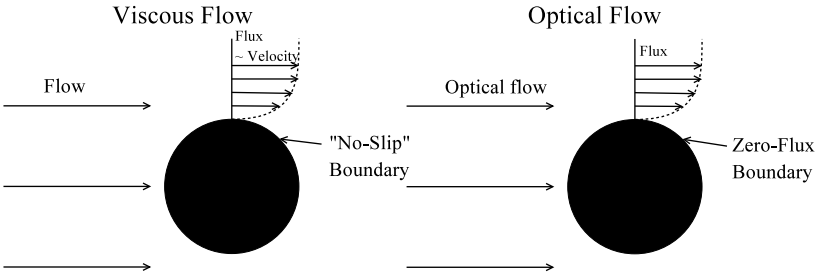

Figure 12.3: Comparison between a viscous boundary layer and an optical boundary layer.

For a viscous fluid flow past an obstacle, as the Reynolds number increases, the boundary layer begins to separate and vorticity is convected behind the obstacle. An analogy in the dynamics of the nonlinear Schrödinger equation, in the form of vortex nucleation on the boundary, is also predicted [22], and in the case of large objects, the instability of the optical boundary layer also depends on the optical Reynolds number $\mathscr{R}$ defined in Eq. (12.40) [40], much like the viscous boundary layer separation.

12.3.2 Dissipation of eddies

Another important effect of viscosity is the dissipation of small-scale structures in turbulence. An analogous effect in nonlinear Schrödinger equation is the emission of sound waves two vortices are close to each other [35] and the generation of Kelvin waves in the process of vortex line reconnections [44]. The radiation of acoustic energy in both cases must cause a damping of the high-spatial-frequency convection within the optical beam, and the effective Reynolds number is again estimated to be equal to the optical Reynolds number [38, 39, 41].

12.3.3 Kármán vortex street

The Kármán vortex street is a famous viscous fluid phenomenon, in which alternate fluid vortices are emitted from the back of an obstacle to the flow of a viscous fluid, when the Reynolds number increases beyond a certain threshold [26, 45]. Using the numerical vortex blob method, Chorin first simulated such a phenomenon for a cylinder obstacle and obtained good agreement with experimental data [46]. Since an optical beam diffracting past a low refractive index region would also emit optical vortices and the vortices interact like vortex blobs in a self-defocusing medium, we performed a numerical experiment of the nonlinear Schrödinger equation to investigate if we would observe a similar phenomenon for nonlinear optics.

The numerical setup is sketched in Fig. 12.4. A big optical beam is assumed to propagate at an angle to an ellipsoid cylinder, with a refractive index much lower than the surroundings to act as an impenetrable object, in a self-defocusing medium. The length of the long axis of the ellipsoid cross section is assumed to

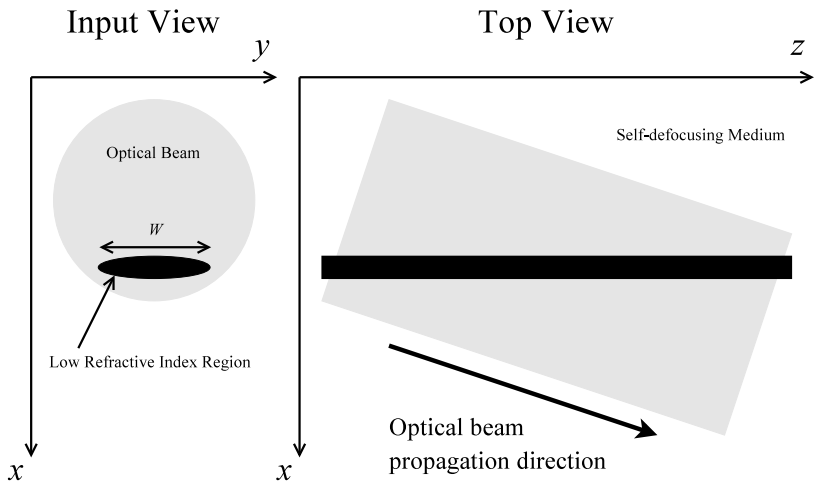

Figure 12.4: Setup of numerical experiment (not to scale).

be W, and the short axis is assumed to be one-fifth of W throughout the simulations. The two-dimensional nonlinear Schrödinger equation is solved using the Fourier split-step method [20], which implies a periodic boundary condition for the optical beam. This should not affect the qualitative behavior of the dynamics, if the optical beam is much bigger than the object. In all of the simulations, the Mach number $\mathscr{M}$ is fixed at 0.4, while the optical Reynolds number $\mathscr{R}$ is varied. Figure 12.5 plots the intensity of the optical beam at a normalized propagation distance $\zeta = 10$ for an optical Reynolds number $\mathscr{R} = KW = 12.8$. Optical vortex solitons are created on the top and bottom side of the low-refractive-index region, and they interact in such a way that resembles the phenomenon of twin vortices behind an obstacle in a low-Reynolds-number viscous fluid flow.

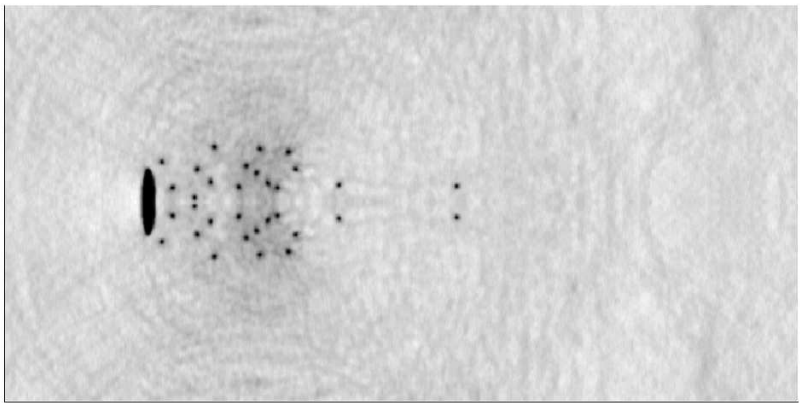

Figure 12.5: The intensity of the optical beam at a normalized propagation distance $\zeta = 10$, for $\mathscr{M} = 0.4$ and $\mathscr{R} = 12.8$. The dark ellipse is the low-refractive-index region that acts as an impenetrable object. Optical vortex solitons are seen to be created on the top and bottom side of the ellipse, While the convection of the solitons behind the object resembles the twin vortices behind an obstacle in a viscous fluid flow.

Figure 12.6 plots the flux $\mathbf{J} = (\psi^* \nabla \psi - \psi \nabla \psi^*)/2i$ and Fig. 12.7 plots the momentum vorticity $\nabla \times \mathbf{J}$.

Both plots confirm the similarity between the numerically observed dynamics and the phenomenon of twin vortices in a viscous fluid flow.

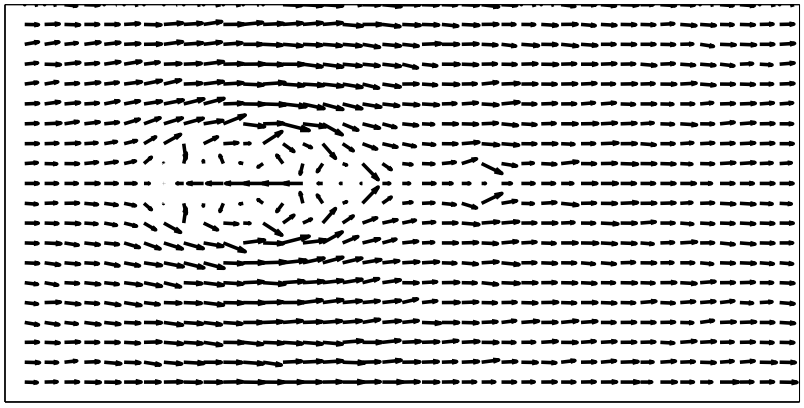

Figure 12.6: A vector plot of the flux $\mathbf{J}$ at $\zeta = 10$, for $\mathscr{M} = 0.4$ and $\mathscr{R} = 12.8$, which confirms the similarity between the numerically observed dynamics and the phenomenon of twin vortices.

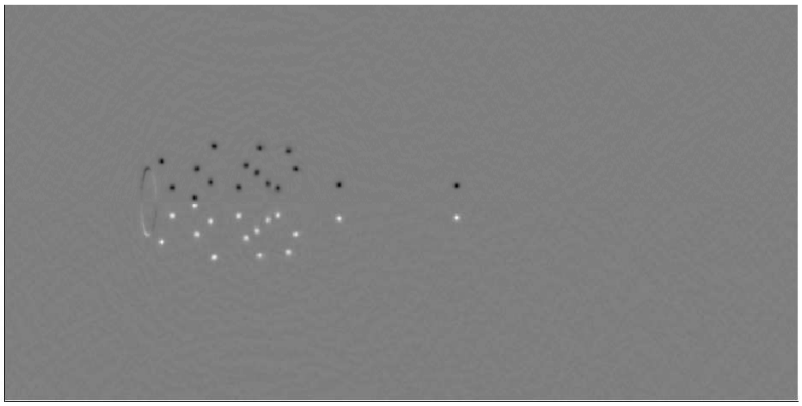

Figure 12.7: A plot of the momentum vorticity $\nabla \times \mathbf{J}$ at $\zeta = 10$, for $\mathscr{M} = 0.4$ and $\mathscr{R} = 12.8$. A white dot indicates that the vortex has a positive topological charge and a black dot indicates that the vortex has a negative charge. The plot shows the similarity between the numerically observed dynamics and the phenomenon of twin vortices.

Figures 12.8, 12.9, and 12.10 plot the intensity, flux, and momentum vorticity of the optical beam respectively, at a longer propagation distance $\zeta = 20$ for the same parameters. The qualitative dynamical behavior of vortices staying behind the object is essentially unchanged.

We now raise the Reynolds number to $\mathscr{R} = 25.6$ and perform the numerical experiment again. As seen from Figs. 12.11, 12.12, and 12.13, the optical vortex solitons become smaller and more abundant, but at $\zeta = 10$ the phenomenon of twin vortices behind an obstacle is again observed.

At $\zeta = 20$, however, significant instability in the twin vortices develops, such that the spatial symmetry between the upper plane and the lower plane is broken, and alternative bunches of optical vortices begin to be emitted from the back of the object. Figures 12.14, 12.15, and 12.16 plot the intensity, flux and vorticity

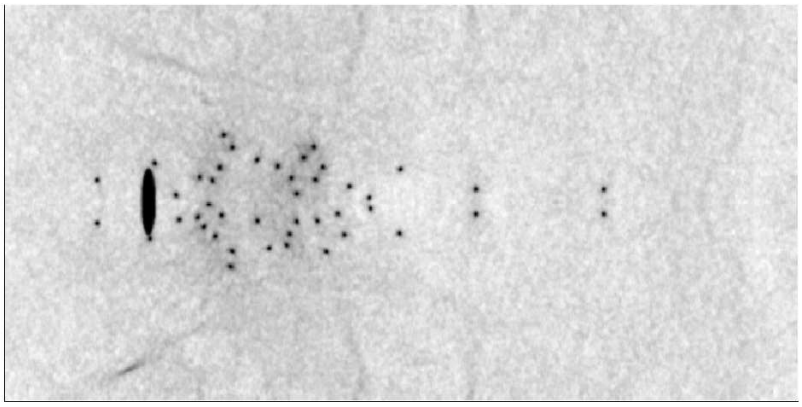

Figure 12.8: The intensity of the optical beam at a normalized propagation distance $\zeta = 20$, for $\mathscr{M} = 0.4$ and $\mathscr{R} = 12.8$. The qualitative dynamical behavior is essentially unchanged from that shown in Fig. 12.5.

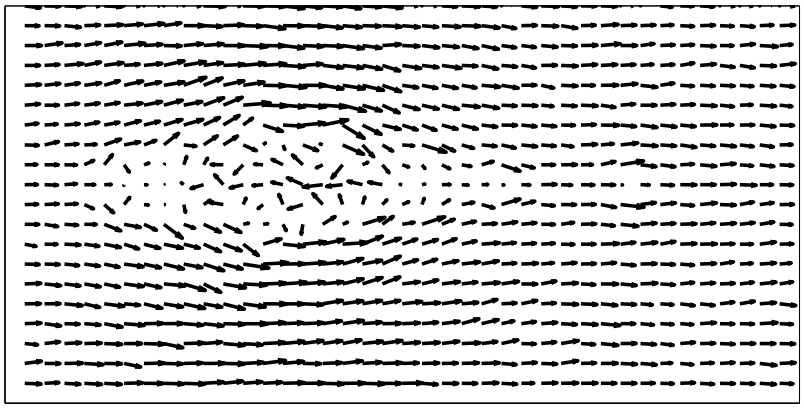

Figure 12.9: A vector plot of the flux $\mathbf{J}$ at $\zeta = 20$, for $\mathscr{M} = 0.4$ and $\mathscr{R} = 12.8$.

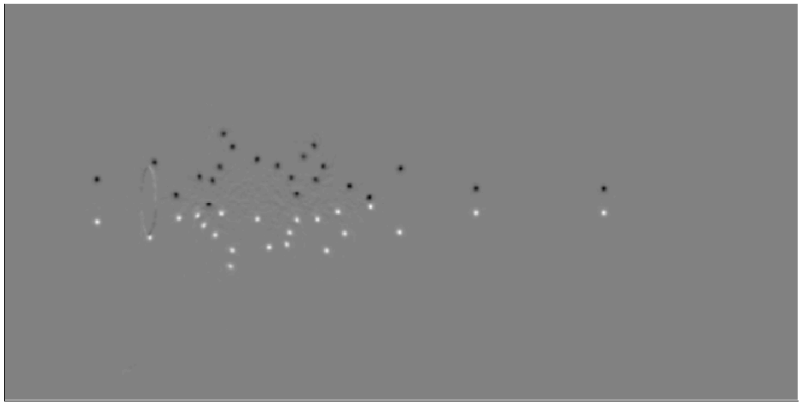

Figure 12.10: A plot of the momentum vorticity $\nabla \times \mathbf{J}$ at $\zeta = 20$, for $\mathscr{M} = 0.4$ and $\mathscr{R} = 12.8$.

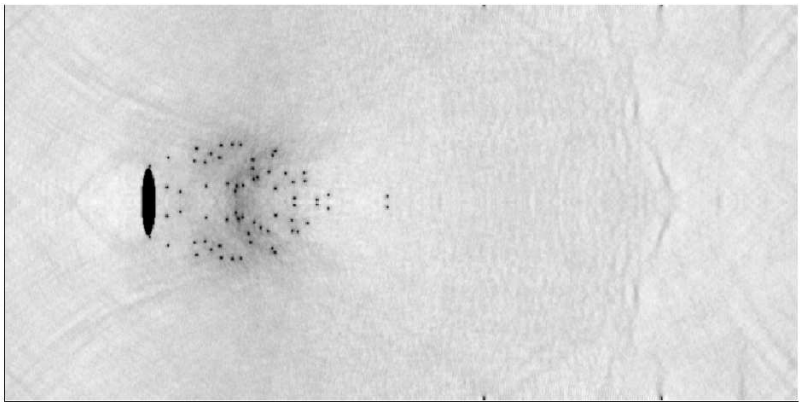

Figure 12.11: The optical intensity at $\zeta = 10$, for $\mathscr{M} = 0.4$ and $\mathscr{R} = 25.6$. The vortex solitons are observed to be smaller, and the phenomenon of twin vortices is again observed.

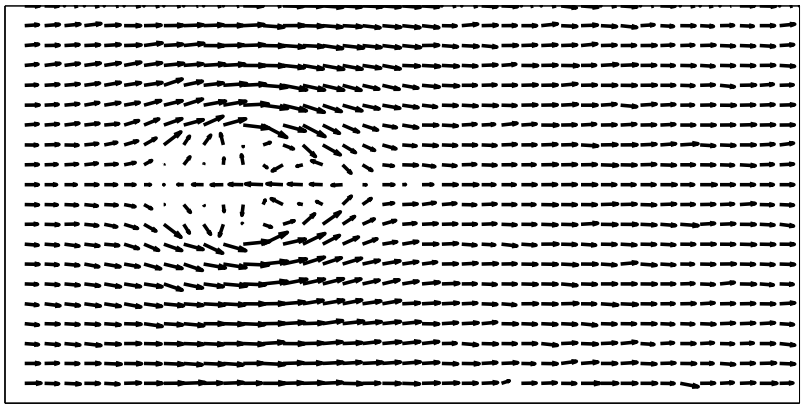

Figure 12.12: The flux $\mathbf{J}$ at $\zeta = 10$, for $\mathscr{M} = 0.4$ and $\mathscr{R} = 25.6$.

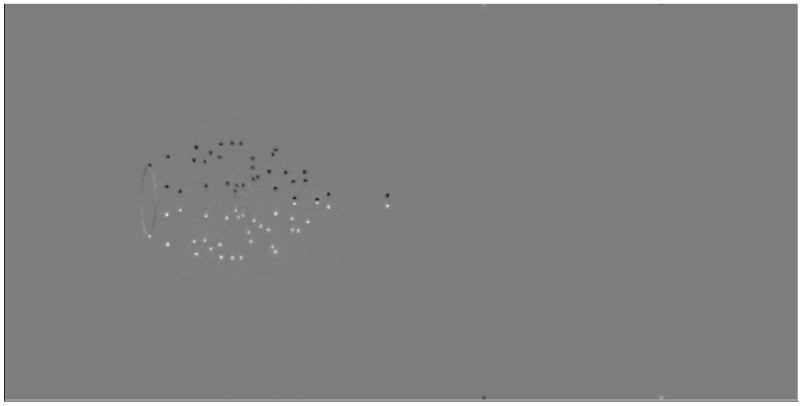

Figure 12.13: The momentum vorticity $\nabla \times \mathbf{J}$ at $\zeta = 10$, for $\mathscr{M} = 0.4$ and $\mathscr{R} = 25.6$.

at $\zeta = 20$ respectively, which demonstrate a behavior strongly resembling the famous Kármán vortex street phenomenon.

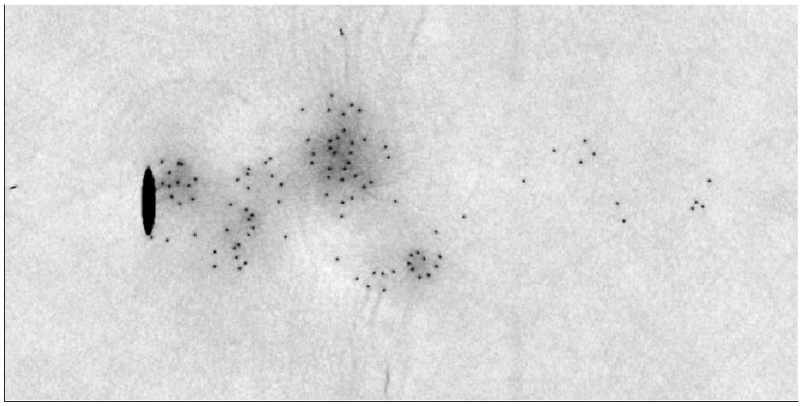

Figure 12.14: Optical intensity at $\zeta = 20$, for $\mathscr{M} = 0.4$ and $\mathscr{R} = 25.6$. The twin vortices become unstable and detach alternatively from the object.

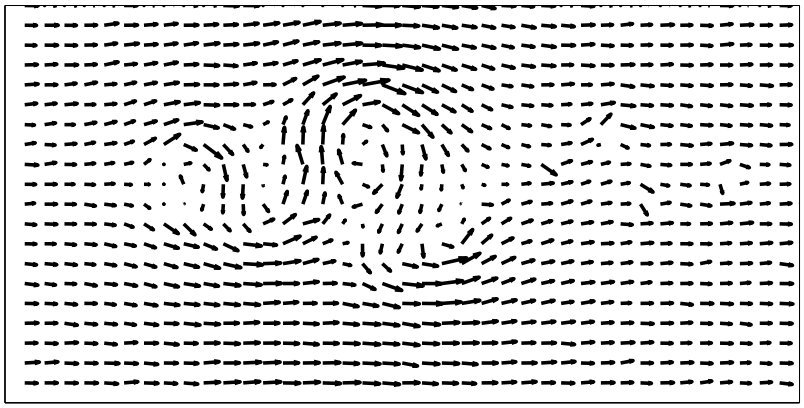

Figure 12.15: Flux at $\zeta = 20$, for $\mathscr{M} = 0.4$ and $\mathscr{R} = 25.6$, which shows a flow pattern strongly resembling the Kármán vortex street.

Due to computing power constraints, we are only able to simulate low-Reynolds-number flows, which we do not expect to quantitatively reproduce viscous fluid dynamics. We have to use an ellipsoid cylinder in the numerical experiments, instead of the more conventional circular cylinder, to artificially generate more optical vortices, and the Mach number is a little too high for compressional waves not to play a significant role in the dynamics. With all that said, using the nonlinear Schrödinger equation, we are still able to qualitatively demonstrate, for the first time to our knowledge, two well-known viscous fluid phenomena, namely, the formation of twin vortices behind an obstacle, and the symmetry-breaking instability of the twin vortices that leads to the Kármán vortex street when the Reynolds number is increased. Compared with previous claims of observing the Kármán vortex street in nonlinear optics numerically [7] or experimentally [8, 9], our numerical results demonstrate an unprecedented level of correspondence between nonlinear optical dynamics and the Kármán vortex street phenomenon, thanks to the presence of a much larger number of optical vortices in our

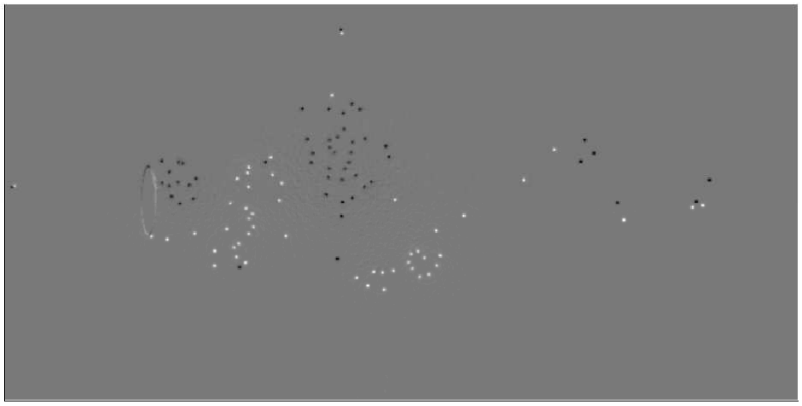

Figure 12.16: Vorticity at $\zeta = 20$, for $\mathscr{M} = 0.4$ and $\mathscr{R} = 25.6$, which confirms that the alternate bunches of vortices indeed have the right charges that resemble the Kármán vortex street phenomenon.

simulations.

12.3.4 Kolmogorov turbulence

The striking similarities between nonlinear optics and viscous fluid dynamics are not limited to low-Reynolds-number two-dimensional problems. As the Reynolds number is further increased to the order of a million, the viscous fluid flow enters a turbulent regime. Since this regime is highly chaotic, only statistical signatures can be reproduced in a turbulent fluid flow. A well-known signature of turbulence is the Kolmogorov energy spectrum [47], derived under the assumption that a "steady state" is reached when the macroscopic-scale fluid flow continuously generate finer spatial structures via convection and viscosity dissipates the smallest structures. As viscosity plays a significant role in the Kolmogorov turbulence spectrum, it is surprising to see that numerical simulations of the three-dimensional nonlinear Schrödinger equation also reproduce the Kolmogorov spectrum at high Reynolds numbers, and the vorticity dynamics of the "superflow" described by the nonlinear Schrödinger equation resembles that of the viscous flow, in which vortex reconnection events play a major role [38, 39].

The dissipation of the smallest spatial structures in a superflow is speculated to be the Kelvin waves produced by the natural motion and reconnections of vortex filaments [41, 44], and the corresponding Reynolds number is again speculated to be $\mathscr{R} = KW$ [41]. Numerical and theoretical analyses of the so-called "quantum turbulence" exhibited by the nonlinear Schrödinger equation all reveal striking similarities between quantum and classical fluids, and it is argued that the study of quantum turbulence could lead to a better understanding of turbulence in normal fluids [48].

12.4 The split-step method

While a nonlinear optical system shows promise for computing Euler and Navier-Stokes fluid dynamics, it also poses serious technical challenges. Ideally one would like to have a configurable nonlinear material with low loss, anomalous group-velocity dispersion, high defocusing nonlinearity, and three-dimensional copropagating boundaries. One may only be able to find separate materials or optical devices, each of which performs only some of the functions. Moreover, parasitic effects such as loss, two-photon absorption, and high-order dispersion can be detrimental to the accuracy. To combine different devices and periodically compensate for parasitic effects, we hereby propose the "split-step" method, the inspiration of which comes from the numerical Fourier "split-step" method [20]. Consider the general nonlinear Schrödinger equation

$$\frac{\partial \psi}{\partial \zeta} = \sum_{n=1}^{N} \hat{H}_n \psi, \tag{12.41}$$

where propagation effects and boundary conditions are expressed in terms of operators $\hat{H}_n$. The formal solution is

$$\psi(\zeta + \Delta\zeta) = \exp\Big(\int_{\zeta}^{\zeta+\Delta\zeta} \sum_{n=1}^{N} \hat{H}_n d\zeta' \Big) \psi(\zeta). \tag{12.42}$$

But if $\Delta\zeta$ is much smaller than $1/H$ where H is the magnitude of the operators, by virtue of the Baker-Hausdorff formula we have

$$\psi(\zeta + \Delta\zeta) = \prod_{n=1}^{N} \exp\left(\hat{H}_n \Delta\zeta\right) \psi(\zeta) + O(H^2 \Delta\zeta^2). \tag{12.43}$$

Each of the propagation effects can hence be applied separately to an optical pulse, with a quadratic error term. A symmetrized version of the split-step method can further reduce the error order,

$$\psi(\zeta + \Delta\zeta) = \prod_{m=N}^{1} \exp\left(\hat{H}_m \frac{\Delta\zeta}{2}\right) \prod_{n=1}^{N} \exp\left(\hat{H}_n \frac{\Delta\zeta}{2}\right) \psi(\zeta) + O(H^3 \Delta\zeta^3). \tag{12.44}$$

The split-step method is not unlike the proof of a quantum computer being able to simulate any quantum systems [23]. Whereas it is difficult to find a quantum device that performs the exact Hamiltonian of the quantum system of interest, it is possible to approximate the Hamiltonian in small time slices. Similarly, in a metaphoric optical computer, one can form a unit cell of a "meta-material" by combining a slice of defocusing material, a slice of material with anomalous group-velocity dispersion, a slice of ultrafast phase modulator to apply the three-dimensional boundary conditions, and a gain medium to compensate for loss. The optical beam can loop through the unit cell multiple times in a cavity, so that the outcome will approximate the true solution as if we had an ideal medium. See Fig. 12.17 for a graphical illustration of the method.

The split-step method has the additional advantages that each subsystem can be tunable and easily substi-

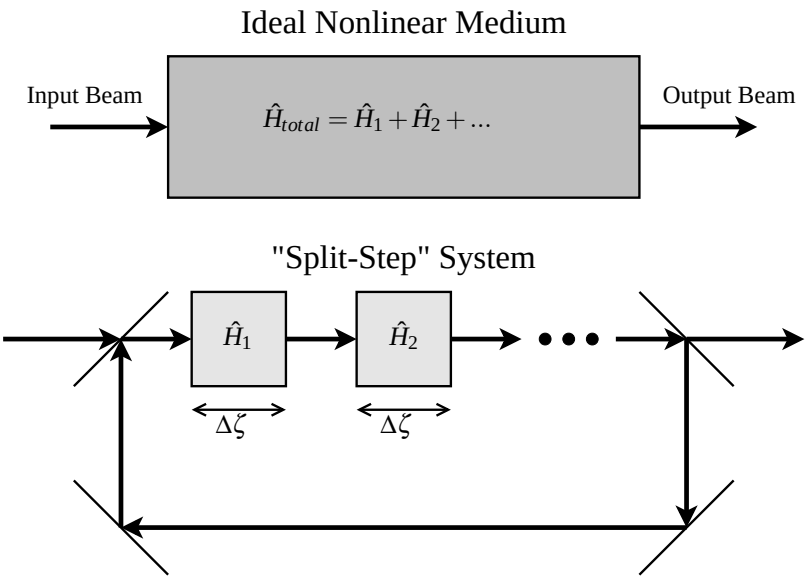

Figure 12.17: Sketch of a split-step optical system that approximates the ideal nonlinear medium.

tuted with another material or device, and the pulse evolution can be monitored more easily. The magnitude of each effect can be tuned by simply changing the propagation length in each device, In exchange for configurability we have sacrificed some accuracy due to discretization errors and instability. The computation speed may also be reduced by a large but constant fraction, as the pulse may spend most of its time on simply propagating from one device to the next and not performing the core computation by nonlinear propagation. The split-step method, however, does not detract from the inherent parallelism in the computation, as the transverse dimensions are not discretized.

12.5 Conclusion

In conclusion, we have used a variety of theoretical and numerical methods to show that self-defocusing optical propagation has a converging correspondence with Euler fluid dynamics and a striking similarity with Navier-Stokes fluid dynamics. We have numerically shown that the interactions of a large number of optical vortex solitons are able to simulate two well-known viscous fluid phenomena. We have also proposed the split-step method, a way of practically implementing the metaphoric optical computer.

There are serious technical challenges if a metaphoric computer is to become useful for computing fluid dynamics, especially three-dimensional fluid dynamics problems, as techniques for the complete specification and characterization of the spatiotemporal optical field are still in their infancy. The speed, configurability, and parallelism of a metaphoric optical simulator nonetheless promise vast advantages over conventional numerical simulations.

Since photons are quantum objects, optical propagation would also inherently compute the quantum dy-

namics of bosons, and may therefore be used as a metaphoric simulator of quantum fluids, such as superfluids, superconductors, and Bose-Einstein condensates. In this way the advantages of a metaphoric computer and those of a quantum computer are combined, and only then the classical and quantum computing capabilities offered by photons would truly be exhausted. This extension of metaphoric optical computing will be a subject of future work.

Bibliography

[1] W. G. Wagner, H. A. Haus, and J. H. Marburger, Phys. Rev. **175**, 256 (1968).

[2] P. Coullet, L. Gil, and F. Rocca, Opt. Commun. **73**, 403 (1989).

[3] M. Brambilla, L. A. Lugiato, V. Penna, F. Prati, C. Tamm, and C. O. Weiss, Phys. Rev. A **43**, 5114 (1991).

[4] F. T. Arecchi, G. Giacomelli, P. L. Ramazza, and S. Residori, Phys. Rev. Lett. **67**, 3749 (1991).

[5] S. A. Akhmanov, M. A. Vorontsov, V. Yu. Ivanov, A. V. Larichev, and N. I. Zheleznykh, J. Opt. Soc. Am. B **9**, 78 (1992).

[6] G. A. Swartzlander, Jr. and C. T. Law, Phys. Rev. Lett. **69**, 2503 (1992).

[7] K. Staliunas, Phys. Rev. A **48**, 1573 (1993).

[8] M. Vaupel, K. Staliunas, and C. O. Weiss, Phys. Rev. A **54**, 880 (1996).

[9] G. Molina-Terriza, D. V. Petrov, J. Recolons, and L. Torner, Opt. Lett. **27**, 625 (2002).

[10] F. S. Roux, J. Opt. Soc. Am. B **12**, 1215 (1995).

[11] D. Rozas, C. T. Law, and G. A. Swartzlander, Jr., J. Opt. Soc. Am. B **14**, 3054 (1997).

[12] D. Rozas, Z. S. Sacks, and G. A. Swartzlander, Jr., Phys. Rev. Lett. **79**, 3399 (1997).

[13] H. Michinel, J. Campos-Táboas, R. García-Fernández, J. R. Salgueiro, and M. L. Quiroga-Teixeiro, Phys. Rev. E **65**, 066604 (2002).

[14] M. J. Paz-Alonso, D. Olivieri, H. Michinel, and J. R. Salgueiro, Phys. Rev. E **69**, 056601 (2004).

[15] M. J. Paz-Alonso and H. Michinel, Phys. Rev. Lett. **94**, 093901 (2005).

[16] Y. Pomeau and S. Rica, C. R. Acad. Sci. Paris, **317**, 1287 (1993).

[17] E. L. Bolda, R. Y. Chiao, and W. H. Zurek, Phys. Rev. Lett. **86**, 416 (2001).

[18] R. Y. Chiao, Opt. Commun. **179** 157 (2000).

[19] R. W. Boyd, *Nonlinear Optics* (Academic Press, San Diego, 2002).

[20] G. P. Agrawal, *Nonlinear Fiber Optics* (Academic Press, San Diego, 2001).

[21] R. J. Donnelly, *Quantized Vortices in Helium II* (Cambridge University Press, New York, 1991).

[22] T. Frisch, Y. Pomeau, and S. Rica, Phys. Rev. Lett. **69**, 1644 (1992).

[23] S. Lloyd, Science **273**, 1073 (1996).

[24] E. Madelung, Z. Phys. **40**, 322 (1926).

[25] M. Quiroga-Teixeiro and H. Michinel, J. Opt. Soc. Am. B **14**, 2004 (1997).

[26] L. M. Milne-Thomson, *Theoretical Hydrodynamics* (The Macmillan Company, New York, 1968).

[27] A. W. Snyder, L. Poladian, and D. J. Mitchell, Opt. Lett. **17** 789 (1992).

[28] J. C. Neu, Physica D **43**, 407 (1990).

[29] L. M. Pismen and J. Rubinstein, Physica D **47**, 353 (1991).

[30] F.-H. Lin and J. X. Xin, Commun. Math. Phys. **200**, 249 (1999).

[31] T.-C. Lin, SIAM J. Appl. Math. **60**, 1099 (2000).

[32] E. B. Sonin, Rev. Mod. Phys. **59**, 87 (1987).

[33] A. Leonard, J. Comp. Phys. **37**, 289 (1980).

[34] J. Grant, J. Phys. A **6**, L151 (1973).

[35] I. Aranson and V. Steinberg, Phys. Rev. B **53**, 75 (1996).

[36] C. Nore, M. E. Brachet, and S. Fauve, Physica D **65**, 154 (1993).

[37] C. Nore, M. Abid, and M. E. Brachet, C. R. Acad. Sci. Paris, **319**, 733 (1994).

[38] C. Nore, M. Abid, and M. E. Brachet, Phys. Rev. Lett. **78**, 3896 (1997).

[39] C. Nore, M. Abid, and M. E. Brachet, Phys. FLuids **9**, 2644 (1997).

[40] J. S. Stiessberger and W. Zwerger, Phys. Rev. A **62**, 061601 (2000).

[41] W. F. Vinen and J. J. Niemela, J. Low Temp. Phys. **128**, 167 (2002).

[42] H. Schlichting, K. Gersten, E. Krause, and H. Oertel Jr., *Boundary-Layer Theory* (Springer, New York, 2000).

[43] N. G. Berloff and P. H. Roberts, J. Phys. A **33**, 4025 (2000).

[44] E. Kozik and B. Svistunov, Phys. Rev. Lett. **92**, 035301 (2004).

[45] C. H. K. Williamson, Annu. Rev. Fluid. Mech. **28**,477 (1996).

[46] A. J. Chorin, J. Fluid Mech. **57**, 785 (1973).

[47] U. Frisch, *Turbulence, the Legacy of A. N. Kolmogorov* (Cambridge University Press, Cambridge, 1995).

[48] S. N. Fisher and G. R. Pickett, “Quantum turbulence,” Phys. World April Issue (2006).